3-26-2014

Materials Interactions and Degradation Processes in Solid Oxide Electrolysis Cells

Michael Keane
University of Connecticut - Storrs, mck09003@engr.uconn.edu

Materials Interactions and Degradation Processes in Solid Oxide Electrolysis Cells

Michael Keane, Ph.D.

University of Connecticut, 2014

Solid oxide electrolysis cells (SOECs) are high temperature electrochemical devices with the potential for large-scale, highly efficient production of hydrogen or syngas with negligible net greenhouse gas emissions. Long-term electrical performance degradation relating to materials interactions at elevated temperatures is one of the primary technical limitations to SOEC commercialization. In this work, solid oxide cells were fabricated and tested using various materials and conditions in order to further the understanding of SOEC degradation mechanisms. This knowledge can be used to develop new materials and fabrication methods that improve performance and long-term stability of SOECs.

SOEC anode delamination from the electrolyte is a major known contributor to performance degradation. Delamination was observed in the current study between strontium-doped lanthanum manganite (LSM) air electrodes (anodes) and yttria-stabilized zirconia (YSZ) electrolytes. Small particles of lanthanum zirconate ($La_2Zr_2O_7$) form at the anode-side LSM-YSZ interface due to pressure buildup as oxide ions from the YSZ are oxidized to oxygen gas. The resulting interfacial fracturing and variance in thermal expansion weaken the LSM-YSZ interface, causing gradual delamination.

Silver-based electrodes were investigated for use in reduced operating temperatures (750 °C or below). Silver-palladium/gadolinia-doped ceria (Ag-Pd-GDC) composite electrodes were electrically stable with 0.8 V applied for 100 h at 750 °C. However, the Ag-Pd was morphologically unstable due to agglomeration and electromigration, requiring

further optimization of the composite structure, particle size, and composition. Oxide impurities in the Ag-Pd migrated to the electrode-electrolyte interfaces and caused local undulations in the YSZ electrolyte surface. These results demonstrate that material purity plays a crucial role in interfacial stability when using silver-based electrodes under applied voltage.

Performance and degradation of Ni-YSZ fuel electrodes (SOEC cathodes) were studied as functions of materials, preparation techniques, and operating conditions. Carbon deposition, nickel evaporation, and impurity poisoning were not observed to negatively affect performance. However, nickel particle size was too large for optimum performance, and agglomeration decreased nickel interconnectivity and contact with the current collector. Structural and compositional optimization is therefore required to make Ni-YSZ electrodes suitable for the electrolysis of water or carbon dioxide.

Materials Interactions and Degradation Processes in Solid Oxide Electrolysis Cells

Michael Keane

B.S., University of Maine, 2009

A Dissertation

Submitted in Partial Fulfillment of the

Requirements for the Degree of Doctor of Philosophy

at the

University of Connecticut

2014

APPROVAL PAGE

Doctor of Philosophy Dissertation

Materials Interactions and Degradation Processes in Solid Oxide Electrolysis Cells

Presented by

Michael Keane, B.S.

Major Advisor_____
Prabhakar Singh

Associate Advisor_____
Alexander Agrios

Associate Advisor_____
Ugur Pasaogullari

Associate Advisor_____
Radenka Maric

Associate Advisor_____
Steven Suib

University of Connecticut

2014

Acknowledgements

I would like to thank my major advisor Professor Prabhakar Singh for his support and direction through my years at the Center for Clean Energy Engineering, and for contributing countless ideas that helped to progress my research. I would also like to thank my advisory committee of Professors Alexander Agrios, Ugur Pasaogullari, Radenka Maric, and Steven Suib. Thanks to Professor Atul Verma for his great insight and lots of long discussions.

Thanks to my past and present research group members: Sapna Gupta, Gavin Ge, Alex Lassman, Na Li, Keling Zhang, Boxun Hu, Manoj Mahapatra, Kailash Patil, and Mahesh Venkataraman, for many hours of helpful discussion. Also much thanks to the visiting students I worked with during my time at the Center, including Chris Kupiec, Steve Onorato, and Hui Fan. Thanks to Professor Steven Suib, Cecil King'ondu, Yongtao Meng, and Altug Poyraz from the UConn Department of Chemistry for technical assistance.

I am happy to acknowledge the Center staff including Peter, Garry, and Mark for helping my experiments in the lab go smoothly, and also Sheila, BJ, Amy, and Leah for their administrative assistance. Thanks to Joe and Mark in the machine shop for designing and fabricating so many parts for my experimental setups.

Thanks to my supervisor Dr. Bruce Randolph and colleagues Dr. Wei Chu and Ron Freeman for their direction and insight during my internship at ConocoPhillips.

Financial support from Idaho National Laboratory, ConocoPhillips, and the Connecticut Space Grant Consortium is much appreciated.

Thanks to my parents and family for their ongoing love and support.

Finally, love and thanks to my wife Nan for her great support and motivation during all my years of my research.

Table of Contents

LIST OF FIGURES

LIST OF TABLES

CHAPTER 1: INTRODUCTION

1.1. Motivation

Due to the increasing need for the reduction of greenhouse gas emissions from the conversion and consumption of energy, there is great interest in areas such as carbon dioxide capture, hydrogen for energy storage and as a clean fuel, and liquid fuel production from syngas (carbon monoxide and hydrogen) [1-3]. Synthetic liquid hydrocarbon fuels can be produced from syngas via the Fischer-Tropsch process, Eq. (1.1):

$$(2n+1)H_2(g) + nCO(g) \rightarrow C_nH_{2n+2}(l) + nH_2O(g) \quad (1.1)$$

The combustion of synthetic fuels produced in this manner results in lower harmful emissions than combustion of conventional diesel and gasoline due to the high purity of synthetic fuels. These fuels also lessen dependence on foreign petroleum.

The most common methods for syngas and hydrogen production are conventional steam reforming and partial oxidation of abundant natural gas and liquid hydrocarbons [2,4]. Since both of the above processes produce significant carbon emissions, development of large-scale syngas and hydrogen production technologies with reduced emissions of greenhouse gases is of great commercial interest. High temperature co-electrolysis of carbon dioxide and water using solid oxide electrolysis cells (SOEC) has been proposed as a highly efficient technique for large-scale syngas production. Since electrolysis is carbon-neutral, the overall process would be nearly free of net carbon emissions when paired with a renewable energy source such as wind [5].

1.2. Operating principles of solid oxide cells

Solid oxide cells (SOC) are a highly efficient means for converting between chemical energy and electrical energy with minimal greenhouse gas emissions. The chemical energy is derived from fuel gases such as hydrogen, carbon monoxide, or methane. Solid oxide fuel cells (SOFC) usually combine hydrogen and oxygen gas to produce water and energy. Solid oxide electrolysis cells (SOEC) operate in the reverse manner, utilizing electrical energy to split water into hydrogen and oxygen [6]. Co-electrolysis of water and carbon dioxide produces both hydrogen and carbon monoxide.

A single SOC is comprised of a dense electrolyte layer and two porous electrodes. One electrode is exposed to a fuel-containing gas while the other electrode is exposed to an oxidizing gas (usually air). The two electrodes are separated by a gastight seal to prevent gas mixing and to maintain a steady gas composition for each electrode. During operation, electron-transfer reactions occur at the triple phase boundaries (TPB) between the electrode, electrolyte, and gas. The electrodes catalyze the reactions and provide conductive pathways for electrons. The electrolyte provides a pathway for oxygen ion (O^{2-}) transport. In an SOEC, oxygen ions diffuse through the electrolyte and exit as oxygen gas on the air electrode side. The electrolyte is not electronically conductive, so the electrons must pass through an external circuit to get from one electrode to the other. A schematic and half reactions of an SOEC are shown in Fig. 1.1. In an SOFC, the directions of the reactions and diffusion of the various gases would be reversed [6].

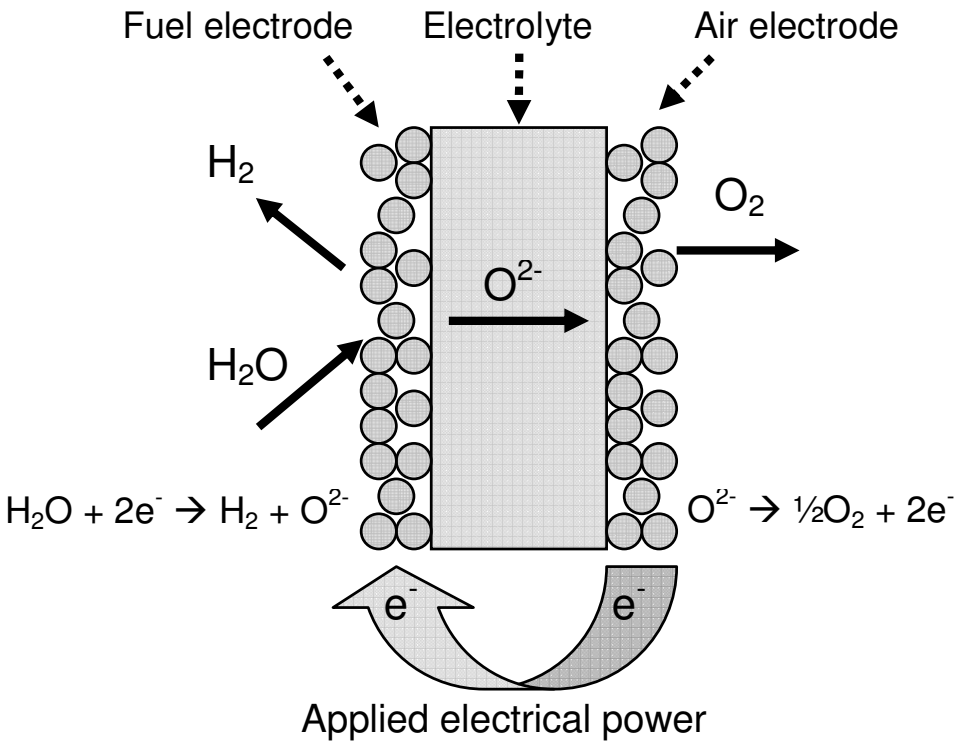

Fig. 1.1. Schematic and reactions of a solid oxide electrolysis cell.

SOCs operate at elevated temperatures (600–1000 °C) due to several advantages. While expensive precious metal catalysts such as platinum are needed to provide acceptable reaction rates at low temperatures (below 200 °C), relatively cheap ceramic-based catalysts are sufficient at elevated temperatures due to faster reaction kinetics. A variety of fuels besides hydrogen, such as carbon monoxide and methane, can undergo reaction at these high temperatures [6]. SOFCs can be used in highly efficient combined heat and power systems due to their high temperature waste heat [7]. Modeling of SOEC systems has shown the potential for thermal efficiency over 50% for water electrolysis, and slightly lower for co-electrolysis when operating at 850 °C [5].

In order for SOCs to withstand very high temperatures and to satisfy the requirements for conductivity and catalytic activity described above, the materials selection must be

carefully considered for each component. In both SOECs and SOFCs, the electrolyte is typically a dense yttria-stabilized zirconia (YSZ). The fuel electrode is usually a porous nickel-YSZ cermet composite, and the air (oxygen) electrode is commonly a porous strontium-doped lanthanum manganite (LSM) or a LSM-YSZ composite [8]. For large scale operation, the cells are connected in series using electronically conducting interconnects [9]. Interconnects are usually fabricated from stainless steel for low to intermediate temperatures (below 800 °C), or ceramics such as lanthanum chromite at high temperatures (above 800 °C) [10]. Seals can be fabricated from glass (e.g. SiO_2-based), other ceramics (e.g. Al_2O_3-based) or precious metals (e.g. gold) [11].

During co-electrolysis of water and carbon dioxide, the electrolysis of water (Eq. (1.2)) is the dominant reaction:

$$H_2O(g) \rightarrow H_2(g) + 0.5O_2(g) \tag{1.2}$$

Most CO is formed by the reverse water gas shift reaction (WGSR), Eq. (1.3):

$$CO_2(g) + H_2(g) \rightarrow CO(g) + H_2O(g) \tag{1.3}$$

However, CO can also be formed by direct electrolysis of CO_2 (Eq. (1.4)) when there is no H_2 or H_2O present in the gas stream:

$$CO_2(g) \rightarrow CO(g) + 0.5O_2(g) \tag{1.4}$$

The reason for the preference for water electrolysis is the higher adsorption capability of water on the fuel electrode [12]. As a result, SOEC performance decreases with higher CO_2/H_2O ratio, and performance is significantly worse during pure CO_2 electrolysis [13].

1.2.1. Thermodynamic explanation

When an SOC is exposed to a fuel and an oxidant, a cell potential develops due to the Gibbs free energy of fuel-oxidant reactions (e.g. Eq. (1.2)). The relationship between standard cell potential $E°_{cell}$ and Gibbs free energy of reaction ΔG is given by Eq. (1.5).

$$\Delta G = -nFE^{\circ}_{cell} \tag{1.5}$$

Here F is the Faraday constant, the amount of charge per mole of electrons, while n is the number of electrons transferred in the reaction; n = 2 for Eq. (1.2). Thus, the standard cell potential is a property of fuel-oxidant reaction, and is a function of temperature and reacting species as shown in Fig. 1.2.

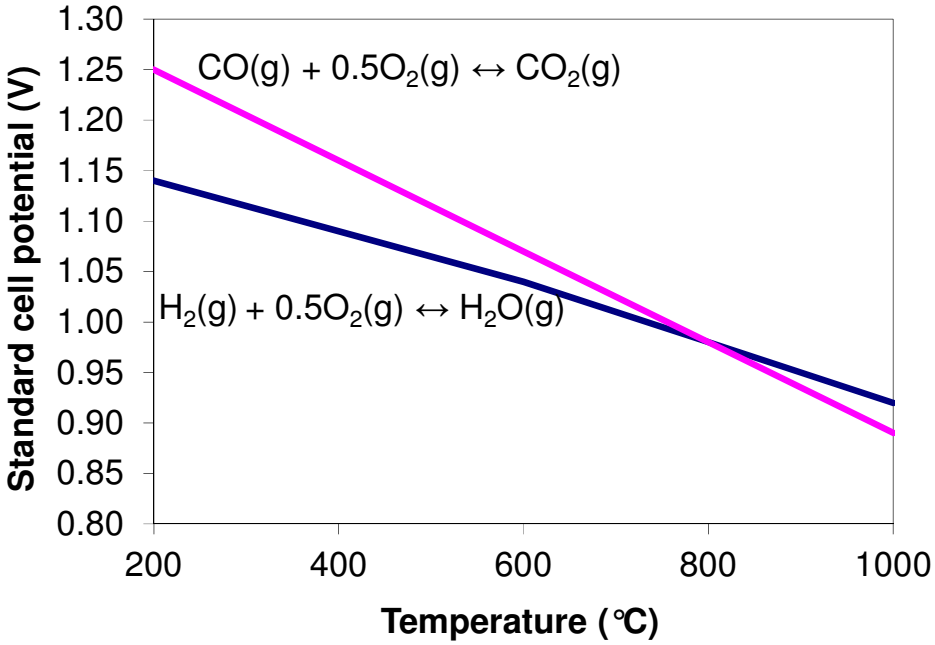

Fig. 1.2. Dependence of standard cell potential on temperature for equilibrium of Eq. (1.2) and (1.4).

The standard cell potential can be related to the equilibrium fuel-side gas composition as shown in Eq. (1.6) when using H_2/H_2O:

$$E_{cell}^{\circ} = \frac{RT}{nF} ln \frac{y_{H_2O,fuel}}{y_{H_2,fuel} y_{O_2,fuel}^{0.5}} \tag{1.6}$$

Here R is the gas constant, T is temperature, and the y_x terms represent the mole fractions of gases on the fuel side. Total pressure of 1 atmosphere and ideal gas behavior are assumed. Equilibrium fuel-side oxygen pressure will generally be very low (below 10^{-12} atm) in a reducing environment such as H_2/H_2O.

The actual cell potential can be explained in terms of the oxygen partial pressure gradient between the air and fuel electrodes, since this gradient is the driving force for oxygen ions to diffuse through the electrolyte. Therefore the actual cell potential depends on the ratio of air-side oxygen pressure to fuel-side oxygen pressure as shown in Eq. (1.7):

$$E_{cell} = \frac{RT}{nF} ln \frac{y_{O_2,air}^{0.5}}{y_{O_2,fuel}^{0.5}} \tag{1.7}$$

This potential is more commonly referred to as the open circuit voltage (OCV) because it represents the measured cell voltage when no current is flowing and gas compositions are therefore at equilibrium. Combining Eqs. (1.6) and (1.7) results in the commonly used Nernst equation, Eq. (1.8):

$$E_{cell} = E_{cell}^{\circ} - \frac{RT}{nF} ln \frac{y_{H_2O,fuel}}{y_{H_2,fuel} y_{O_2,air}^{0.5}} \tag{1.8}$$

OCV can also be determined when using co-electrolysis. The reverse WGSR (Eq. (1.3)) has a high enough rate constant under SOC operating conditions that equilibrium can be assumed [12]. The equilibrium composition of gases is first determined from the inlet

composition, mole balance equations, and the equilibrium constant for the reverse WGSR [14]. The equilibrium mole fractions of water and hydrogen are then used to calculate OCV via Eq. (1.8).

The OCV of each cell in an SOEC stack is approximately 0.8 to 1 V when using typical gas compositions ($0.1 < y_{H2}/y_{H2O} < 5$) and temperature (800–850 °C). During electrolysis operation, the voltage applied to each cell is typically thermal neutral voltage (TNV), approximately 1.3 V. At this voltage, the rate of thermal energy consumption by the electrolysis reaction is equal to the rate of thermal energy production due to ohmic heating in the cell. If an SOEC stack operating at TNV were perfectly thermally insulated, the stack temperature would remain constant without the addition or removal of heat. High voltages are avoided as the additional ohmic heating could result in localized overheating and high thermal gradients in the stack [15].

1.2.2. Cell performance

When an SOC is being operated, half reactions occur at the electrodes as shown in Fig. 1.1. A current flows due to the movement of electrons between the electrodes through an external circuit. Due to various energy losses (overpotential) within the cell, the voltage will deviate from OCV when current is flowing. When operating in fuel cell mode, the overpotentials cause voltage to decrease with current because power is being drawn from the cell. When operating in electrolysis mode, the overpotentials cause voltage to increase with current because power is being delivered to the cell [16]. The relationship between current density and voltage is called the current-voltage characteristic (Fig. 1.3). In this example,

current is zero at OCV = 0.97 V, and current density at TNV is approximately -0.45 A/cm^2 (by convention, current in the electrolysis direction is negative).

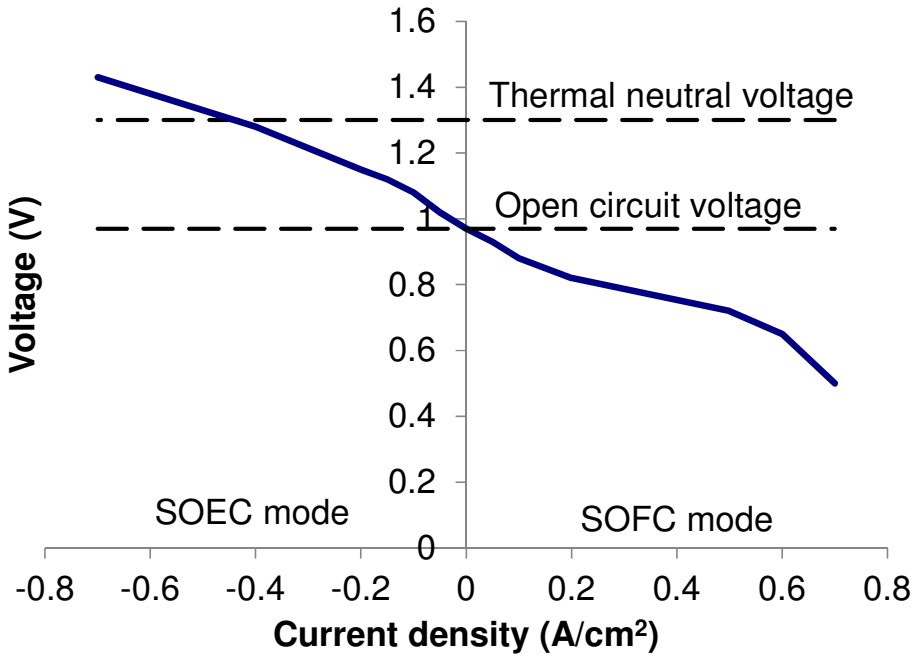

Fig. 1.3. Current-voltage characteristic of a typical SOC.

Sources of overpotential are usually grouped into three main categories: activation, ohmic, and mass transport [16]. Activation refers to the activation energies of the electrode reactions, which are related to the reaction kinetics. The reactions consist of several steps including gas adsorption, dissociation, electron transfer, and surface diffusion. Activation losses can be minimized by improving reaction kinetics by increasing operating temperature or using electrodes with better catalytic properties. Since the directions of the reactions in SOFC and SOEC are opposite to each other, their kinetic properties, and therefore the activation losses, will necessarily differ between SOFC and SOEC. It has been experimentally observed that increased activation losses are responsible for lower performance in SOEC than in SOFC for several air electrode materials [17].

Ohmic losses are due to direct resistance of current according to Ohm's law, V = IR. In an electrolyte-supported SOC, the ionic resistance of the electrolyte is dominant, since it is usually several orders of magnitude higher than the resistance of the electrodes. The use of a thin-film electrolyte can significantly reduce ohmic losses because ohmic resistance is proportional to thickness. Ohmic losses for SOFC and SOEC will be identical since Ohm's law does not depend on current direction.

Mass transport losses stem from the limitations of reactant gas diffusion from the gas stream, through the electrode pores, to the triple phase boundary, and of product gas diffusion in the reverse direction. Increasing gas flow rates or modifying the electrode pore structure can increase gas diffusion rates, reducing the mass transport losses. Since the directions of the reactions in SOFC and SOEC are opposite to each other, the diffusion direction of each gas will differ, so mass diffusion losses will necessarily differ between SOFC and SOEC.

1.3. Degradation issues in solid oxide electrolysis cells

One of the most important developmental barriers in SOC technology is that of long-term performance degradation, particularly in electrolysis mode [18]. Electrode-electrolyte materials interactions are primary causes of this degradation, encompassing a wide range of phenomena such as phase formation, interface segregation, and electrode delamination [19]. Foreign phases can also contribute to SOC degradation, as evidenced by chromium poisoning of the air electrode [9,20] and silica poisoning of the fuel electrode [21].

1.3.1. Air electrode

At temperatures above 800 °C, chromium evaporation from metallic interconnects and balance-of-plant components becomes a significant issue for SOC. Chromium evaporates in the form of $CrO_2(OH)_2$ or CrO_3 and travels through the air stream to deposit in the vicinity of the triple phase boundaries (TPB) on the cell. Since the cell reactions occur on the TPB, deposited chromium species block the reaction sites and result in performance degradation over time [20].

Under typical SOC operating conditions, the air electrode-electrolyte interface can be chemically unstable due to reactions between the electrode and electrolyte. The common pairing of an LSM-based air electrode and a YSZ electrolyte can cause cell degradation because of solid-state reaction between LSM and YSZ to form lanthanum zirconate (LZ) via Eq. (1.9):

$$La_{1-x}Sr_xMnO_3 + ZrO_2 \rightarrow \frac{1-x}{2}La_2Zr_2O_7 + xSrZrO_3 + MnO_y + \frac{3+x-2y}{4}O_2(g) \quad (1.9)$$

Since the number of strontium atoms per formula unit lies in the range $0.1 < x < 0.2$ in the standard LSM formulation, strontium zirconate will be significantly less prevalent than will LZ. The steps leading to LZ formation are as follows: (1) manganese, which is susceptible to solid state diffusion, moves from the LSM to the YSZ due to the higher manganese activity in LSM relative to YSZ; (2) reduced manganese content in the LSM reduces its thermodynamic stability and causes lanthanum oxide formation; (3) lanthanum oxide reacts quickly with the YSZ to form LZ. Since LZ is poorly conducting relative to LSM and YSZ, its formation at the interface results in significant performance degradation [22]. Other air electrode materials also form interfacial zirconates with YSZ, such as lanthanum strontium

cobalt ferrite (LSCF), which forms strontium zirconate due to its relatively high strontium content [23].

Air electrode (SOEC anode) delamination has been considered as the largest contributor to SOEC performance degradation [9]. Anode delamination from the electrolyte results in reduced electrochemically active area and increased ohmic loss. Although the delamination mechanism is not fully understood, several processes have been postulated, including high oxygen pressure development, morphological changes in LSM anodes, and electrolyte grain boundary separation [9,24–27].

It has been suggested that the transport of volatile chromium species from steel interconnects to the electrode-electrolyte interface could lead to the anode delamination [28]. The observations remain inconclusive as tests conducted in the absence of chromium-containing materials have also resulted in the electrode delamination [24].

Virkar et al. have proposed that the delamination of the SOEC anode is due to the buildup of high oxygen pressure near the anode–electrolyte due to differences in ionic and electronic conductivity between the anode and the electrolyte. For a primarily electronic conducting anode such as LSM, high oxygen pressure can build up within the closed pores at or near the anode–electrolyte interface according to Eq. (1.10) [29]:

$$p_{max} = p_{O_2,air}\, exp\left(\frac{4FE_{cell}\delta_1\delta_2(\sigma_{i(1)}\sigma_{e(2)} - \sigma_{i(2)}\sigma_{e(1)})}{RT(\sigma_{e(1)}\delta_2 + \sigma_{e(2)}\delta_1)(\sigma_{i(1)}\delta_2 + \sigma_{i(2)}\delta_1)} \right) \tag{1.10}$$

Here p_{max} is the theoretical maximum oxygen pressure, $p_{O2,air} = 0.21$ atm for air, δ is component thickness, σ_i and σ_e are ionic and electronic conductivities, respectively, and the subscripts 1 and 2 refer to the electrolyte and the anode, respectively. This equation calculates pressures of more than 10^{10} atm when inputting realistic parameter values, but real cell components will crack before such pressures are attained. This high-pressure mechanism

for mechanical separation has been refuted by Momma et al., who observed that a platinum anode did not degrade significantly or delaminate in a long term experiment [24]. Authors showed that high oxygen pressures developed at the platinum-YSZ interface were not sufficient to cause delamination.

Knibbe et al. [30] have proposed that the observed electrical performance degradation in the electrolysis cells consisting of an LSM-YSZ composite anode results from the formation of porosity in the YSZ electrolyte grain boundaries near the anode–electrolyte interface and not by the delamination of the anode. The porosity formation in the electrolyte is postulated to be due to high oxygen partial pressure buildup because of an increase in electromotive potential in the YSZ electrolyte near the interface.

Kaiser et al., on the other hand, concluded that the electrode delamination could be caused by the presence of doped aluminum in YSZ and formation of an electronically conducting $MnAl_2O_4$ layer near the anode–electrolyte interface [25]. Authors also suggest that the delamination can be prevented by coating a layer of pure YSZ near the interface. This is inconsistent with the observations of three groups that have observed delamination using a pure YSZ electrolyte [24,26,31].

Chen et al. concluded that delamination of the LSM anode from the electrolyte results from LSM disintegration near the anode–electrolyte interface [32]. The authors proposed that the electrode disintegration results from the development of tensile strains due to lattice shrinkage, caused by the formation of cation vacancies in the over-stoichiometric (oxygen excess) stability field of LSM at high oxygen partial pressures. However, this study is limited to a single, moderate current density. Authors do not report any resistive phase formation

(e.g. lanthanum zirconate) between the LSM and YSZ despite the well-known reactivity between these materials [22].

1.3.2. Fuel electrode

Ni-YSZ electrodes can also be significant contributors towards SOC degradation. Nickel particle agglomeration in Ni-YSZ fuel electrodes reduces the concentration of active sites for electron transfer, negatively affecting performance. Nickel agglomerates to a similar degree in both SOFC and SOEC, but the rate of agglomeration has been found to increase with H_2O partial pressure [33,34]. More severe degradation of Ni-YSZ during SOEC operation has been attributed to nickel evaporation and deposition at the electrode-electrolyte interface at high current densities (above 1 A/cm^2) [34]. However, nickel evaporation is less problematic in SOFC due to the comparatively low H_2O partial pressure [33,35]. The nickel evaporation is attributed to high volatility of $Ni(OH)_2$ in high H_2O partial pressure [33-36].

Exposure of Ni-YSZ electrodes to atmospheres containing CO or CO_2 can bring about carbon formation via disproportionation (the Boudouard reaction, Eq. (1.11)):

$$2CO(g) \leftrightarrow C(s) + CO_2(g) \tag{1.11}$$

Solid carbon is deposited on the electrode, reducing porosity and blocking reaction sites, which leads to cell performance degradation. This degradation mechanism is well-known to occur in SOFC [36] and has been proposed to occur in SOEC [13]. The H_2/H_2O ratio affects the degree of carbon deposition according to Eq. (1.12):

$$CO(g) + H_2(g) \leftrightarrow C(s) + H_2O(g) \tag{1.12}$$

Applying a current to the cell affects the H_2/H_2O and CO/CO_2 ratios in the vicinity of the fuel electrode, which in turn shifts the equilibrium of Eqs. (1.11) and (1.12). The apparent effect of current application is to reduce the extent of deposition in SOFC [37], but increase the extent of deposition in SOEC [13].

However, other authors have disputed the role of carbon deposition in SOEC degradation. Ebbesen and Mogensen [38] tested SOECs using conditions (70% CO_2, 30% CO) under which carbon formation is not thermodynamically favorable via Eq. (1.11) and observed more severe Ni-YSZ degradation than in an H_2/H_2O atmosphere. Although it is possible that applying a current could cause carbon deposition due to increased CO content in the vicinity of the fuel electrode, such deposition would be reversed when returning to OCV conditions. However, the degradation was not reversible when returning to OCV after applying current, so the degradation was instead attributed to poisoning of the electrodes by sulfur impurities in the CO/CO_2 gas stream. The sulfur impurities deposit on the active reaction sites at the TPB, which slows the reaction rates and decreases cell performance.

1.3.3. Electrolyte

Electrochemical testing at 750 °C with silver-based electrodes and YSZ electrolyte has revealed morphological damage at the electrode-electrolyte interfaces. The electrolyte surface develops a severely undulated surface in a few isolated locations in contact with the electrodes [39]. A similar YSZ morphology has been seen after contact with platinum [40] and nickel wire at 1000 °C. The morphology at the nickel-YSZ interface was found to depend on the direction of current passage as well as purity of the nickel. The authors explain

that the formation of YSZ undulations reduces the YSZ surface energy, and this effect is enhanced by nickel impurities segregating to the nickel-YSZ interface. The impurities involved include Si, Al, Ti, and Na and may originate from either the nickel or the YSZ. Cell resistance was significantly lower when using materials with lower impurity content [41].

1.4. Approaches to mitigate degradation

1.4.1. Composite electrodes

Using composite electrodes can significantly reduce the rate of degradation of SOC. One common composite electrode is LSM-YSZ. These electrodes are usually a 50-50 wt% mixture of micron-size LSM and YSZ. These are referred to as "mixed conducting" because the LSM provides electronic conductivity while the YSZ provides ionic conductivity. In general, there is a performance improvement compared to pure LSM due to the increased length of the triple phase boundary (TPB, between LSM, YSZ, and air) for the air electrode half reaction to take place [42,43]. In some cases, LSM-YSZ anodes can still delaminate from the electrolyte under electrolysis conditions, which is attributed to LSM disintegration near the interface with the electrolyte [44].

Such composites usually consist of micron-size particles, but can also be manufactured through infiltration of nanoparticles such as LSM onto a porous scaffold such as YSZ. This type of electrode structure significantly improves their durability, reducing the chances for delamination [44,45] and improving performance stability [46]. The improvement is attributed to the microstructural stability of the LSM nanoparticles, in

contrast to larger LSM particles which can disintegrate under electrolysis conditions [47]. However, Li et al. [48] have suggested that improvement of the infiltrated electrodes is due to the porosity of the YSZ scaffold, which prevents oxygen gas from building to high pressures at the anode-electrolyte interface according to Virkar's model [29]. The interconnected scaffold may have better mechanical adhesion to the electrolyte compared to the randomly distributed YSZ particles in the LSM-YSZ composite, which can also reduce the tendency for delamination.

1.4.2. Electrode-electrolyte interlayer

One technique to inhibit interfacial reactions is the use of a less reactive layer between the electrode and electrolyte. One commonly used interlayer between a lanthanum strontium cobalt ferrite (LSCF) electrode and a YSZ electrolyte is gadolinia-doped ceria (GDC) [23,49]. Since the GDC blocks direct contact between LSCF and YSZ, formation of strontium zirconate is significantly reduced and performance is improved. The GDC layer should be completely dense to prevent LSCF-YSZ contact, and it should be a thin layer (less than 5 μm) so as to not significantly increase cell resistance.

An interlayer of Mn-doped YSZ has been shown to reduce the rate of lanthanum zirconate (LZ) formation between an LSM electrode and a YSZ electrolyte. LZ formation is initiated by diffusion of manganese from LSM to YSZ due to the manganese activity gradient between LSM and YSZ. Using a Mn-doped YSZ layer adjacent to the LSM will reduce this activity gradient, slowing manganese diffusion and therefore slowing the LZ formation rate. However, manganese will eventually diffuse from the LSM to the Mn-doped YSZ interlayer

and to the pure YSZ electrolyte bulk. Therefore, LZ formation is slowed but not prevented using this technique [48].

1.4.3. Lower temperature operation

Lowering the operating temperature of solid oxide cells is an effective method of reducing the materials interactions that lead to performance degradation, thus improving long-term performance. Lower temperatures (below 650 °C) have several other benefits including shorter heat-up time, reduced stack heating requirements, and lower fabrication costs. Materials for interconnects and balance-of-plant components have less stringent requirements, further reducing the cost. However, many common solid oxide cell materials have poor performance at lower temperatures, such as LSM (poor reaction kinetics) and YSZ (low ionic conductivity) [50].

Gadolinia-doped ceria (GDC) is the most common electrolyte material for SOCs operating below 650 °C due to its high conductivity for oxygen ions at these temperatures. However, the GDC structure can be chemically unstable under reducing atmosphere, requiring careful consideration of atmospheric operating conditions [51]. Air electrode materials with good low-temperature performance include lanthanum strontium cobalt ferrite (LSCF) in the range of 500–800 °C [52] and barium strontium cobalt ferrite (BSCF) in the range of 500–700 °C [53].

Silver-based electrodes have been investigated for use in lower temperature solid oxide cells (550–750 °C) due to high catalytic performance even at lower temperature, in addition to good electronic conductivity and oxygen permeability [54]. While LSM and

similar ceramic electrodes are known to form insulating zirconate products at the electrode-YSZ electrolyte interfaces, there are no known reaction products between silver and YSZ. However, silver is typically used as a component of silver-ceramic composite electrodes to avoid the oversintering and evaporation during sintering of pure silver [55]. Good performance for an Ag-$Er_{0.4}Bi_{1.6}O_3$-YSZ composite electrode has been reported at 650 °C, but applied voltage causes performance degradation due to silver electromigration in the same direction as the current [56,57]. Promising results have also been reported for silver-doped or infiltrated electronic conductors such as LSM [58], as well as ionic conductors such as samarium-doped ceria (SDC) [59], although stability remains questionable. In general, lower temperature, lower voltage, and lower silver content improve stability (at the expense of performance) due to the reduced effects of electromigration and agglomeration.

1.4.4. Elimination of impurities

Since many SOC components are prone to impurity deposition and subsequent performance degradation, it is often preferable to reduce or remove these impurities from the SOC system. Coatings on the cell system components can be used to mitigate chromium evaporation and subsequent poisoning of the air electrode. Stainless steel interconnects can be coated with an electronically conducting cobalt-manganese spinel. Balance of plant components can be fabricated from nickel- or iron-base alloys that form a non-conducting Al_2O_3 surface layer at elevated temperatures [20].

Sulfur poisoning of the fuel electrode may occur when using impure fuel gases. Sulfur can be removed from the electrode surface by introducing hydrogen, which reacts with

any adsorbed sulfur to form the volatile hydrogen sulfide [38]. Alternatively, the inlet gases can be cleaned to remove the impurities before they reach the cell. Silica poisoning of the fuel electrode is possible when using silica-based seals [21], and can be mitigated by using a metallic seal such as gold.

Impurities may also originate in the solid state from the cell materials. Ni-YSZ interfacial degradation has been attributed to solid-state impurity migration from the materials to the interface. This degradation was mitigated by using higher purity component materials [41]. These findings emphasize the importance of using high purity materials throughout the SOC test system, as well as high purity gases.

1.5. Overall objectives and scope

The objective of this work is to develop a better understanding of materials interactions that lead to electrical performance degradation in solid oxide electrolysis cells. Although there is significant range of published literature on SOCs operated in fuel cell mode, work on SOECs has been much more limited. Previously reported studies on SOECs describe a wide range of degradation mechanisms that are often inconsistent with one another. This study seeks to provide explanations of degradation mechanisms that expand upon findings in literature. This knowledge can be used to develop new materials and fabrication methods that improve performance and long-term stability of SOECs.

Chapter 2 describes the experimental techniques used in this study. Cells were first fabricated from a variety of component materials, and a text fixture for supporting the cells was designed and assembled. In the study of air electrode-related degradation, a simplified

symmetric cell setup was used in order to focus on the root causes of degradation in the absence of complicating factors such as differing fuel electrode atmospheres and cell interconnects. The study of fuel electrode-related degradation required a full cell arrangement. High-temperature electrochemical tests were performed on the cells in order to quantify initial performance and the performance degradation rates. The cells were tested under a variety of atmospheric, temperature, and electrical conditions. Chemical and morphological changes at the electrode–electrolyte interfaces and in the electrode bulk were investigated using characterization techniques after electrochemical tests.

Chapter 3 discusses the delamination of the SOEC air electrode from the electrolyte, which is considered the most important contributor to SOEC degradation. Specifically, the delamination mechanisms are studied using the common LSM air electrode and YSZ electrolyte. The proposed mechanistic pathway leading to delamination includes both chemical reactions and mechanical effects at the LSM-YSZ interface.

Chapter 4 examines the use of silver in SOEC electrodes. Silver's benefits include good catalytic performance at lower temperature and chemical inertness with other SOEC components. Silver-ceramic composite electrodes show greatly improved performance and stability compared to purely metallic electrodes. However, despite silver's non-reactivity, trace impurities in the silver can migrate to the electrolyte and cause morphological instability at the silver-electrolyte interface. Mechanisms for this instability and its implications on cell performance are discussed.

Chapter 5 discusses SOEC fuel electrode degradation during both H_2O electrolysis and CO_2 electrolysis. Degradation of the Ni-YSZ fuel electrodes is characterized in terms of electrochemical performance, morphological stability, and chemical stability. Based on fuel

electrode behavior under various conditions, degradation mechanisms relating to nickel agglomeration, nickel volatilization, solid-state migration, and impurity deposition are evaluated as they relate to electrode composition and preparation.

Chapter 6 summarizes the conclusions on the materials interactions that lead to degradation in SOECs. Final recommendations are provided for materials and operating conditions to maximize cell performance while minimizing long-term degradation. Additional experiments for further understanding of degradation process are suggested. Finally, the impact of the findings on the body of SOEC literature is discussed.

CHAPTER 2: EXPERIMENTAL TECHNIQUES

2.1. Test preparation

2.1.1. Solid oxide button cell fabrication

Electrolyte-supported solid oxide button cells were fabricated from 25 mm diameter and 190 µm thick yttria-stabilized zirconia (YSZ) electrolyte substrates (Fuel Cell Materials). Electrode pastes were procured from Fuel Cell Materials and ESL ElectroScience. Electrodes were fabricated by screen printing of paste. The screen printing technique involves the use of a squeegee to push the paste through a screen mesh of a desired shape, resulting in a coating of uniform thickness that is later dried. In this study, 10 mm diameter circular electrodes were screen printed on the electrolyte substrates using a 105 size mesh. After drying, an identically sized electrode was screen printed on the other size of the electrolyte, concentric to the first electrode. Electrodes were subsequently heated in air to 400 °C for 1 hour to volatilize organics, and then sintered in air for 2 hours. If the two electrodes required different sintering temperatures, the higher sintering electrode was screen printed and sintered first. The area of the cell electrodes was approximately 0.8 cm^2; this is considered the electrochemically active area. Silver screen current collectors (Alfa Aesar, 50 mesh) with silver wires (Alfa Aesar, 0.25 mm) were attached to each electrode using silver-palladium contact paste (ESL ElectroScience). Sintering of the current collector was performed in air for 1 hour at 850 °C. All heating and cooling rates were 3 °C/min during the sintering cycles.

Cell component materials, composition stoichiometries, and sintering temperatures are listed in Table 2.1.

Table 2.1. Cell component material specifications (CC = current collection).

Material	Composition	Cell component	Sintering temperature (°C)
YSZ	$(ZrO_2)_{0.92}(Y_2O_3)_{0.08}$	Electrolyte	N/A
LSM	$(La_{0.8}Sr_{0.2})_{0.98}MnO_{3-x}$	Air electrode	1200
LSM-YSZ	50 wt% LSM, 50 wt% YSZ	Air electrode	1200
GDC	$Ce_{0.8}Gd_{0.2}O_{2-x}$	Air-side interlayer	1200–1400
NiO-YSZ	66 wt% NiO, 34 wt% YSZ	Fuel electrode	1400
Ag-Pd	$Ag_{0.85}Pd_{0.15}$	Air electrode/CC	850

2.1.2. Cell test fixture design and assembly

A schematic of the experimental test fixture is shown in Fig. 2.1. A 25 mm diameter Al_2O_3 tube was used to support the each cell assembly. For full cell testing, the cell was sealed to one end of the tube using Aremco Ceramabond 552 (Al_2O_3-based) cement, with the fuel electrode facing the inside of the tube. Fuel-side gas was fed through a 6 mm diameter Al_2O_3 tube inside of the 25 mm tube. Outlet product gas was fed to a vent. The assembly was positioned so that the cell was located in the center of the furnace's heating zone in order to minimize spatial thermal gradients near the cell. Another 6 mm diameter Al_2O_3 tube was positioned above the cell for feeding air. Each electrode was connected to two leads from a multi-channel potentiostat (VMP2, Bio-Logic) for electrochemical testing. On each electrode,

one of the leads was used for passing current while the other lead was used for applying voltage, in accordance with a standard "four-electrode" configuration. The silver wire leads (Alfa Aesar, 0.50 mm) were passed from the cell through two double-bore 6 mm diameter Al_2O_3 tubes attached to either side of the 25 mm tube. A type K (chromel-alumel) thermocouple with an Inconel 600 (nickel-chromium alloy) sheath was placed within 5 mm of the cell to monitor the operating temperature.

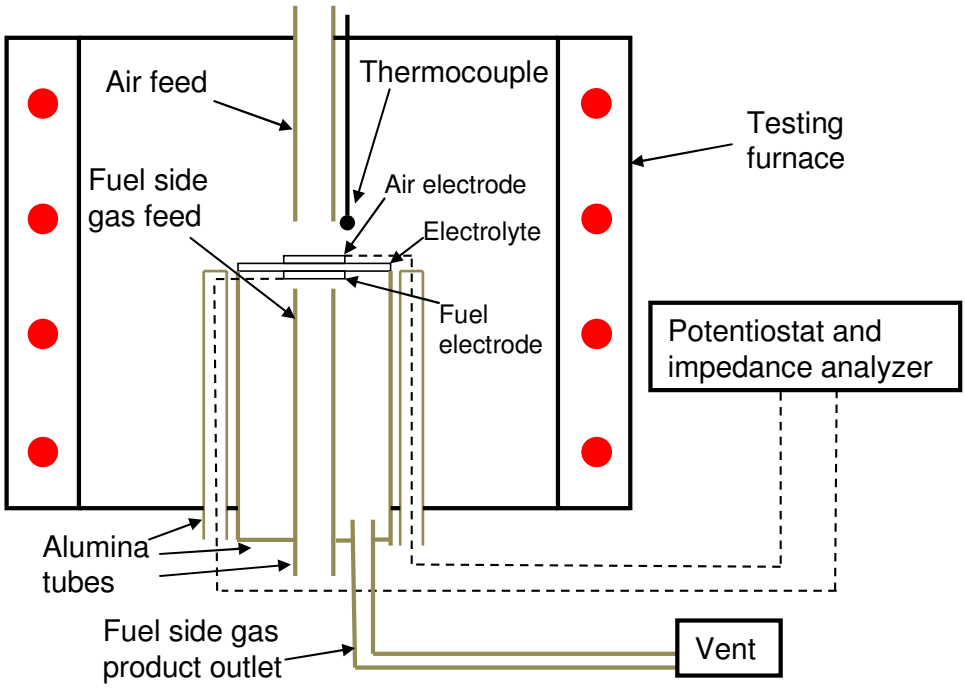

Fig. 2.1. Schematic of cell and test fixture in furnace.

Furnace temperature and gas flows through individual mass flow controllers were controlled remotely through computer software (Advanced Measurements, Integrity). The furnace was heated and cooled at 3 °C/min for all tests to avoid thermal shock of the cell and test fixture components. Fuel-side gases passed through a mixing chamber and then through a gas bubbler containing water. The temperature of the bubbler could be controlled to provide

a defined volume fraction of water in the gas stream, assuming full saturation. The tube leading from the bubbler to the furnace was heated to prevent water condensation.

2.2. High temperature electrochemical testing

Electrochemical testing software (Bio-Logic, EC-Lab) was used to characterize the performance of the cells using a variety of methods. Current-voltage characteristics (represented in Fig. 1.3) were used to give a picture of each cell's performance in both fuel cell and electrolysis mode, through a range of operating voltages. Current-voltage characteristics were generated by applying a series of fixed voltages to the cell and measuring the current responses. Voltages were applied in terms of deviation from OCV within the range of OCV - 0.5 V to OCV + 0.8 V using increments of 0.1 V. The current at each voltage initially changed with time due to electrode activation/deactivation processes [60], but typically reached a near-steady state within a few minutes. The final measured value of current at each voltage was used to plot the current-voltage characteristic. Each voltage was applied for a maximum of ten minutes to minimize cell degradation effects and avoid performance drifting.

Cell stability in electrolysis mode was tested for up to 200 h. Stability testing allowed for a quantitative measurement of performance degradation as a function of time. A constant voltage between OCV + 0.3 V and OCV + 0.8 V was applied, and current was recorded every 60 s. Although typical SOECs are operated at 0.3–0.4 V above OCV for thousands of hours, cells in the current study were tested in a wide voltage range to assess the degradation under simulated nominal and accelerated cell operating conditions. A potentiostatic (constant

voltage) rather than galvanostatic (constant current) technique was chosen because if severe degradation occurs while using a constant current, voltage may exceed the limits of the potentiostat. However, if severe degradation occurs while using a constant voltage, current will drop to near zero, avoiding any instrumental limitations. Current typically increased for the first few minutes to hours due to electrode activation processes, then decreased due to various degradation effects.

2.2.1. Electrochemical impedance spectroscopy

Electrochemical impedance spectroscopy (EIS) is a powerful technique for measuring the impedance of electrochemical cells. Impedance is a generalized form of resistance; while resistance measures the ratio of voltage to direct current according to V = IR, impedance refers to the relationship between a sinusoidal (alternating) voltage and current. During an impedance measurement, sinusoidal voltages are applied using a wide range of frequencies (e.g. 100 mHz to 200 kHz) while recording the sinusoidal current responses at each frequency (potentiostatic EIS). Alternatively, sinusoidal currents can be applied while recording the voltage responses (galvanostatic EIS). The impedance at each frequency has two components: the magnitude of the ratio between the amplitudes of the voltage and current, and the phase shift between the voltage and current responses. Impedance can also be converted to real and imaginary components using Euler's formula. When the impedances are expressed in terms of their real and imaginary components and plotted across a range of frequencies, a Nyquist plot is formed, which usually consists of one or more semicircles (Fig.

2.2). [61] Usually the impedances are multiplied by the active area of the cell giving the units of $\Omega \cdot cm^2$ in order to compare the performance of cells of different sizes.

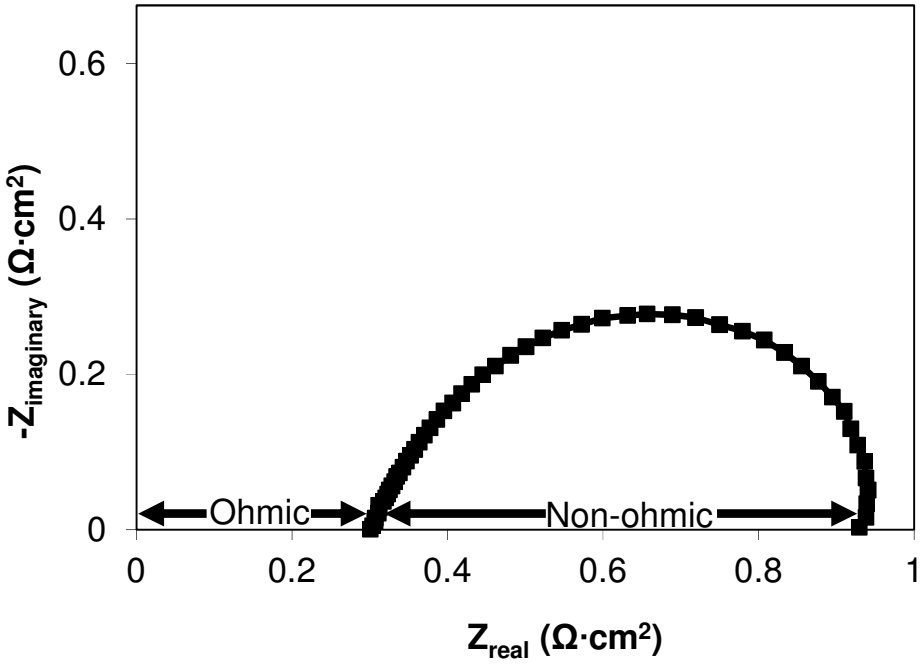

Fig. 2.2. Typical Nyquist plot of impedance data for an SOC. The horizontal axis represents the real component of impedance, while the vertical axis represents the imaginary component.

Impedance is able to distinguish between cell processes that are affected differently at different frequencies of current. For SOC, impedance measurements allow for the separation of cell resistance into ohmic and non-ohmic contributions. Ohmic resistance is primarily contributed by the electrolyte due to its large thickness and low conductivity compared to the electrodes. Ohmic resistance is the only type of resistance measured at high frequencies of current because electrons (or oxygen ions) are able to quickly reverse direction. The leftmost intercept of the semicircle with the horizontal axis in Fig. 2.2 is known as the high-frequency intercept, and it represents the ohmic resistance. Non-ohmic resistance refers to oxygen

surface exchange and migration (activation losses), as well as gas-phase transport (mass transport losses) [62]. Non-ohmic processes are relatively slow, so their impedances are only captured at low frequencies. The rightmost intercept of the semicircle with the horizontal axis in Fig. 2.2 is known as the low-frequency intercept. The diameter of the semicircle represents the non-ohmic resistance. In SOC, the semicircle is often depressed due to the considerable spatial variation in non-ohmic processes because of the complexity of the electrode microstructure [63]. The sum of ohmic and non-ohmic impedance is the total cell impedance, and is equivalent to the slope of the current-voltage characteristic (e.g. Fig. 1.3) at the applied bias voltage. This total impedance is often referred to as area-specific resistance (ASR), a commonly-used metric of SOC performance [6].

Impedance measurements were performed at both open circuit voltage and under bias voltages before and after stability tests to quantify initial and final performance. During the stability tests, impedance measurements were performed at four hour intervals under bias voltage using a 10 mV amplitude alternating current in the frequency range from 100 mHz to 200 kHz. These periodic impedance measurements were used to complement the current measurements during testing.

2.3. Post-test characterization

Post-test cells were analyzed for morphological and chemical changes in comparison with as-fabricated cells. Bulk electrode and electrode–electrolyte interfaces were examined for structural changes and reaction product formation.

2.3.1. Scanning electron microscopy (SEM)

An FEI Quanta 250 FEG scanning electron microscope (SEM) and was used for morphological study. Cells were either viewed “as is”, or were prepared for viewing by various methods. For viewing of fractured cross sections, cells were carefully bent until breaking. This simple method allowed for the viewing of a fracture section of the electrolyte, electrodes, and current collection. Electrode-electrolyte interfaces could also be examined for degradation effects due to testing.

To observe a top view of the electrolyte surface in contact with an electrode, the electrode needed to be removed. This was accomplished by dissolving in dilute hydrochloric acid (for perovskite electrodes) or nitric acid (for silver electrodes) for 1–2 h at room temperature. The YSZ electrolyte is insoluble in these acids, so the exposed surface could be examined for morphological changes or formation of reaction products.

Polished cross sections were also observed for additional morphological understanding and for more precision in measurement of composition. Epoxy was prepared by mixing 4 parts resin with 1 part hardener (Buehler, Epoheat) and mixing for 2–3 min at room temperature. The epoxy was added to a mold with a fractured cell sample and cured at 55 °C for 90 minutes. The hardened epoxy was removed from the mold and ground using successively finer grit grinding paper (Buehler, Carbimet 2, 180, 320, and 600 grit). Then the sample was polished using polishing cloth (Buehler, MicroCloth) and diamond polishing suspensions (Buehler, MetaDi, 9 μm and 3 μm) followed by a colloidal silica suspension (Buehler, MasterMet, 0.06 μm).

Prepared cell samples were attached to SEM sample mounts and coated with a thin layer of gold to improve surface conduction, which is necessary for effective SEM viewing. The gold was applied using a vacuum sputter coater (Denton Vacuum, Desk V HP). The resulting gold layer was too thin to affect surface morphology when viewing in the SEM.

Morphology of the electrolyte, electrodes, and interfaces was compared between as-fabricated and post-test cells. By observing cells tested under a variety of operating conditions, structural changes could be correlated to these operating conditions. Multiple cells tested under each set of conditions were observed in order to ensure consistency among identically tested cells.

2.3.2. Energy-dispersive X-ray spectroscopy (EDS)

Energy-dispersive X-ray spectroscopy (EDAX, attached to SEM) was used for the identification of elements while observing samples in the SEM. Sampling depth is on the order of 1 μm. The precision of the EDS is such that volumes as small as 1 μm^3 adjacent to the viewing surface can be analyzed. The analysis is only semi-quantitative, so it is generally not effective for determining precise composition. However, it is useful for comparing large (more than 10%) compositional differences among samples or different locations on one sample. Use of a flat polished cross section provides more EDS accuracy than an irregular fractured cross section. The detection limit is approximately 1 at%.

EDS was used to verify approximate compositions of the cell materials, for detection of foreign impurities, and for identification of reaction products formed among the cell materials. Elemental interdiffusion at solid-solid interfaces could be detected through the use

of line scans, which measure composition in successive locations along a line. Elemental mapping provides a two-dimensional picture of elemental distribution; this technique is useful when analyzing multi-phase composite electrodes.

2.3.3. X-ray diffraction (XRD)

A Bruker AXS D-8 Advance X-ray diffractometer (XRD) was used for the identification of compounds present in both as-fabricated and tested cells. Detection limits can be below 1 wt%. For most ceramic materials, the volume of analysis extends from the top surface of the sample to a depth of approximately 5–10 μm. This technique complements EDS, which can identify elements but not how they are combined into compound phases. However, XRD is limited in that the entire top surface of a sample is analyzed at once, rather than precise locations as is possible with EDS.

Minimal sample preparation was used for the XRD analysis of cells. When analyzing an as-fabricated or post-test electrode, the cell was placed on the sample holder as-is. When analyzing the electrolyte surface in contact with an electrode, the electrode was first dissolved in acid in the same manner as during SEM preparation, exposing the active area on the electrolyte surface. XRD would then detect if any reaction products insoluble in the acid had formed in measurable quantities on the electrolyte surface during testing.

2.3.4. Focused ion beam (FIB) and transmission electron microscopy (TEM)

An FEI Strata 400 DualBeam field emission scanning electron microscope (FESEM) with focused-ion beam (FIB) technology was used for preparation of transmission electron microscope (TEM) thin cross-section samples of cell electrolytes. A platinum layer was deposited on the electrolyte surface prior to FIB cutting. The cross-section was cut perpendicular to the electrolyte surface in order to observe YSZ surface morphology and to look for reaction products or impurity layers. The sample was then transferred to a TEM sample holder and thinned to a thickness of approximately 100 nm.

An FEI Tecnai Spirit TEM was used for sample imaging. The TEM allowed for a higher resolution cross-sectional view compared with the SEM for two main reasons. First, the minimum resolvable feature size on the samples was about 2 nm in the TEM, compared to 20 nm in the SEM. Second, the FIB cutting provided a much smoother cross-section compared to grinding and polishing for the SEM. Therefore the TEM could image the morphology with much greater precision.

TEM-EDS was used for compositional analysis of the samples. While SEM-EDS measures the composition of a volume approximately 1 μm^2 by 1 μm deep, TEM-EDS could analyze a significantly smaller volume due to the thickness (100 nm) of the sample. This allowed for more precise determination of the composition of small features such as impurities.

CHAPTER 3: LSM-YSZ INTERACTIONS AND ANODE DELAMINATION IN SOLID OXIDE ELECTROLYSIS CELLS

3.1. Objectives

Although anode delamination from the electrolyte is considered the most severe mode of degradation in SOEC, there are many competing theories regarding the delamination mechanism, and full understanding has not yet been achieved. In order to further the understanding of SOEC anode delamination, chemical and morphological changes at the anode–electrolyte interface have been investigated in this study using electrochemical tests with a symmetric cell configuration. The symmetric cells were electrochemically tested at various operating voltages to measure the overall electrochemical degradation and examine the chemical, structural and morphological changes at the anode–electrolyte interfaces. A mechanism for the electrode delamination has been developed based on experimental results and observations.

3.2. Experimental

Cells and test fixtures were fabricated as described in section 2.1. Symmetric cells had the configuration Ag-Pd/LSM/YSZ/LSM/Ag-Pd. Unlike the conventional full cell configuration, the use of symmetric cells simplifies the cell assembly and eliminates sealing requirements as both electrodes are exposed only to air. The electrochemical reaction associated with the oxygen reduction at the cathode remains identical to the cathodic reaction

in an SOFC, while the oxygen ion oxidation at the anode is identical to the anodic reaction in an SOEC. The cell arrangement therefore provides a simple configuration where air electrode behavior in both SOFC and SOEC conditions can be compared. Flowing air (less than 2% water vapor) was delivered to the cathode side at 300 standard cm^3/min (sccm). Due to the identical atmosphere on both sides of the cell, OCV was approximately 0 V. An operating temperature of 840 °C was used, in accordance with standard conditions for SOEC [5].

For each cell, a constant voltage was applied for 100 h and the cell current was recorded every 60 seconds throughout the duration of the test. Cells were tested in a wide voltage range (0 to 0.8 V) to assess the degradation under simulated nominal and accelerated cell operating conditions. Impedance measurements were performed at four hour intervals under the same voltage bias. Experiments were repeated several times at each voltage condition to ensure reproducibility.

3.3. Results

3.3.1. Electrochemical measurements and post-test observations

Fig. 3.1 shows Nyquist plots of typical impedance spectra exhibited by the symmetric cell assembly at 0.8 V. Ohmic and non-ohmic resistances at each time interval were determined from the high- and low-frequency x-intercepts.

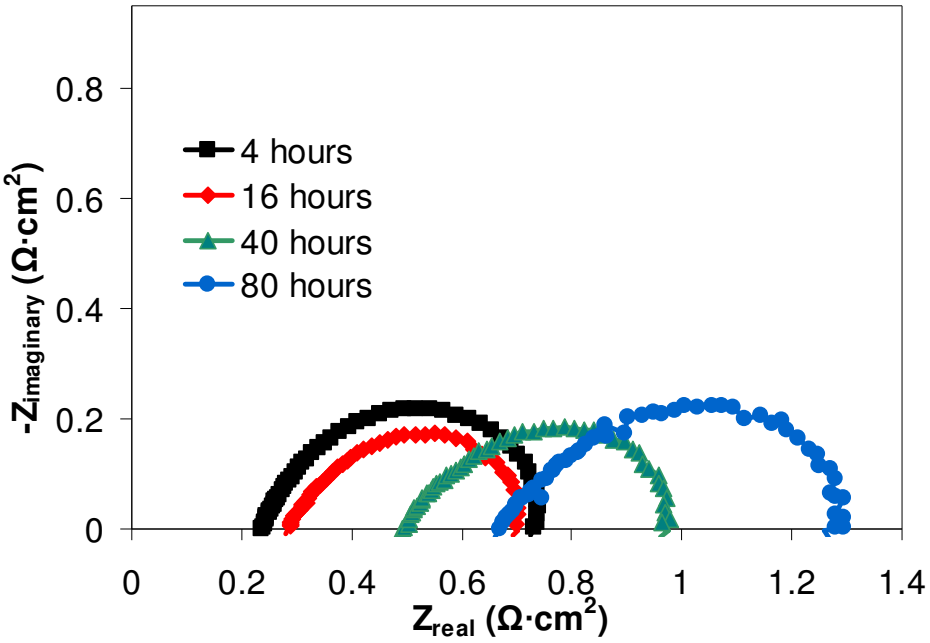

Fig. 3.1. Nyquist plots of impedance spectra obtained from a cell tested with 0.8 V from 4 to 80 hours. For clarity, only four spectra are shown.

Fig. 3.2 shows ohmic and non-ohmic resistances, as well as current density, as a function of time for cells tested at 0.8 V. The cells showed an initial improvement in both ohmic and non-ohmic performance with subsequent increase (degradation) of both resistances after 20 hours; the majority of the cell degradation after 4 hours was due to ohmic resistance degradation. Current density typically reached a maximum of approximately 2.0 A/cm^2 after an initial improvement. The trends in resistance changes tested at different voltages are shown in Fig. 3.3. Both ohmic and non-ohmic resistances showed more severe increases at higher applied voltages. While initial ohmic resistances at different voltages were similar, initial non-ohmic resistances showed a strong negative correlation with applied voltage. Non-ohmic resistances took longer to reach a minimum at lower applied voltages.

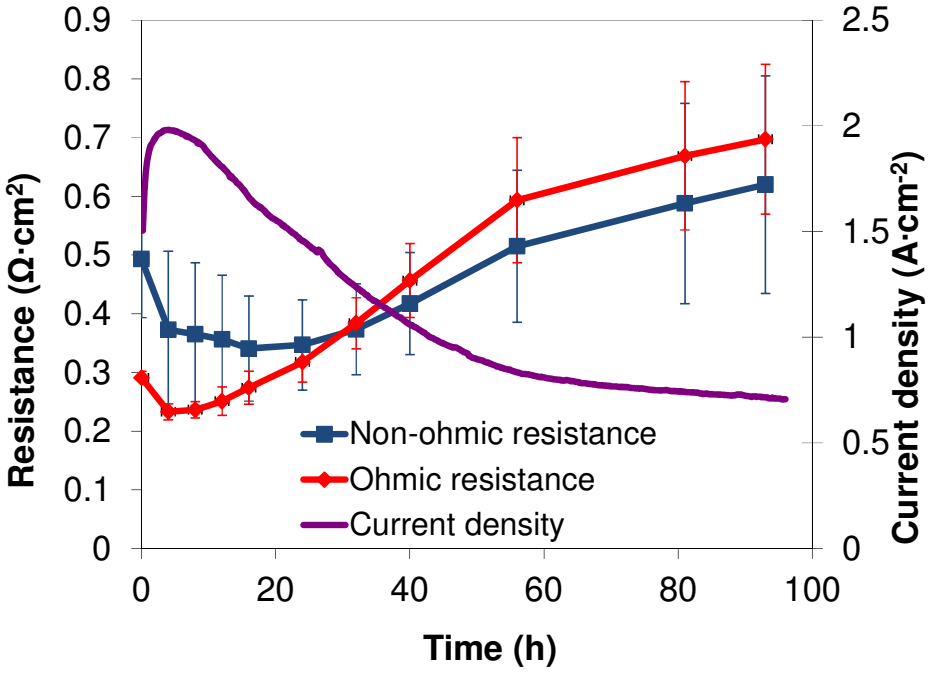

Fig. 3.2. Plots of average ohmic and non-ohmic resistances and current density over time during 100 hour tests with 0.8 V applied.

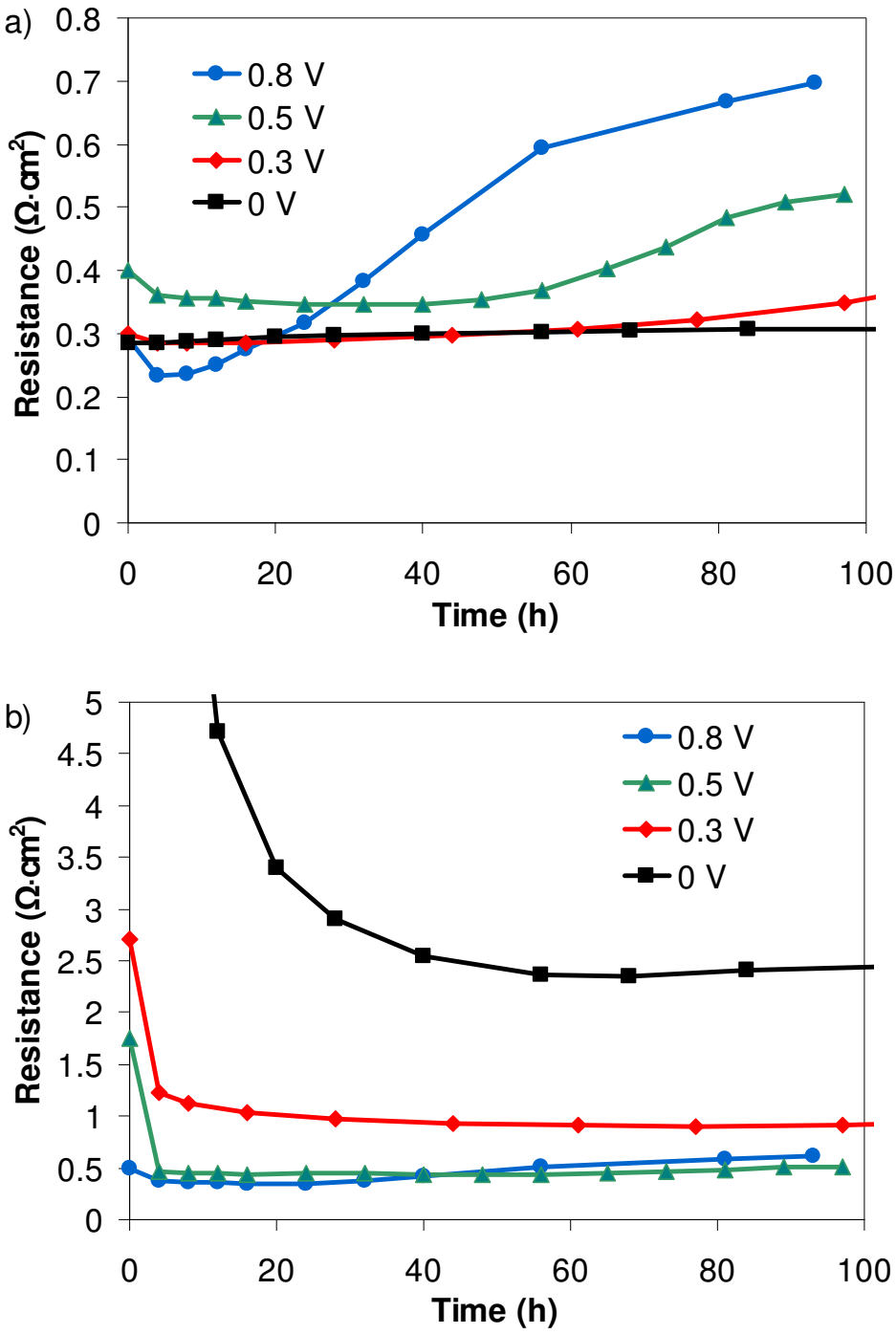

Fig. 3.3. Plots of average resistances over time during 100 hour tests at different applied voltages; a) ohmic; b) non-ohmic.

Fig. 3.4a represents the reproducibility of the ohmic resistance trend for four cells tested at 0.8 V. Using air flow rates below 300 sccm brought about variance in non-ohmic resistance due to mass transport limitations, while increasing the air flow above 300 sccm had no effect on non-ohmic resistance, indicating minimal contribution from mass transport limitations (Fig. 3.4b). Therefore, an air flow rate of 300 sccm was used for all experimental conditions.

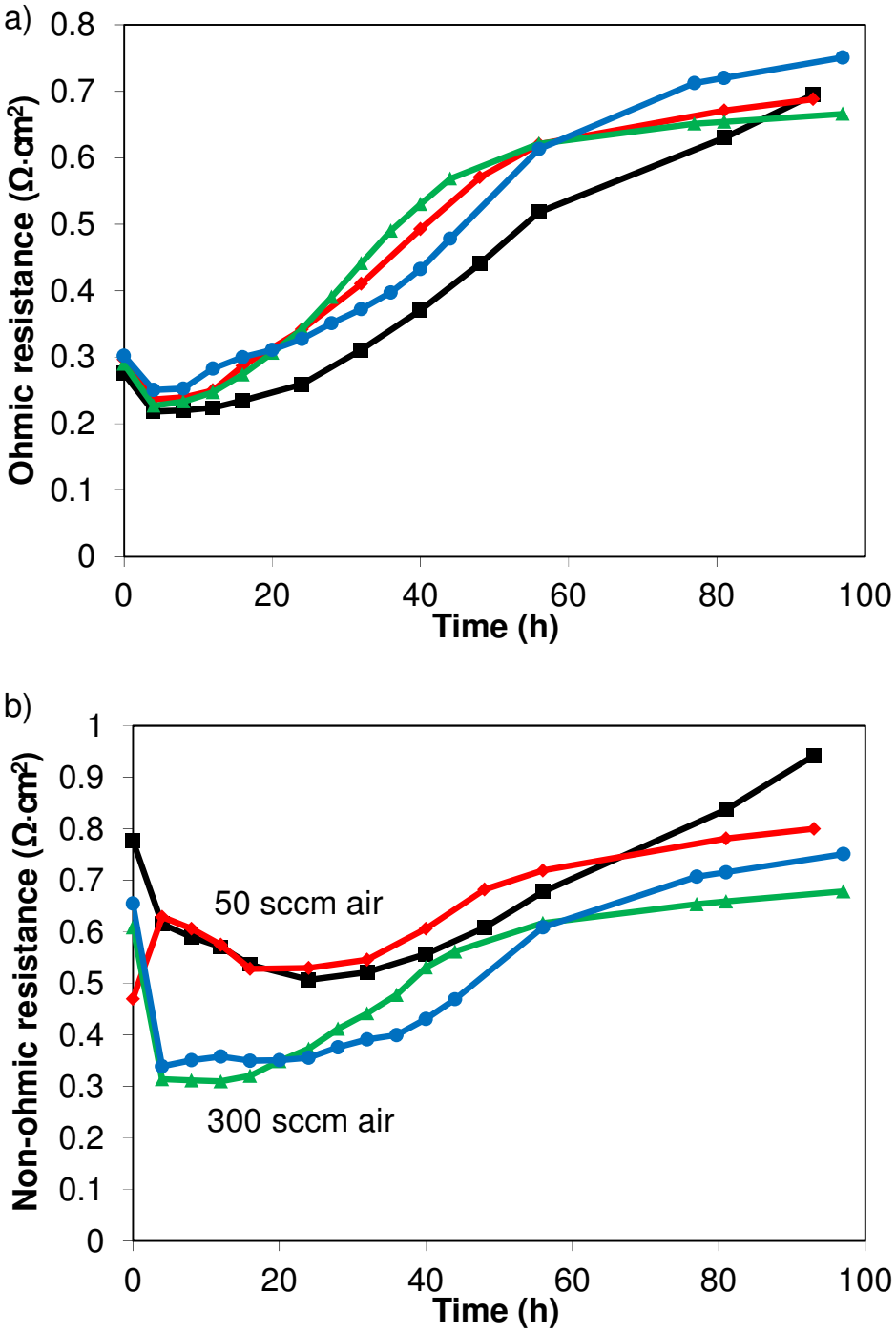

Fig. 3.4. Plots of a) ohmic and b) non-ohmic resistance changes with time for four cells tested at 0.8 V. The two tests shown with ■ and ◊ were operated with 50 sccm flowing air, while the tests shown with ▲ and ● were operated with 300 sccm flowing air.

After completion of the electrochemical tests, cells were visually examined for electrode integrity and attachment with the electrolyte. A complete delamination of the anode from the electrolyte of each cell tested at 0.8 V was observed during the cell disassembly. The anode left behind a dark-colored imprint on the electrolyte after delamination. Anodes from the cells tested at 0.5 V and 0.3 V also showed anode delamination, however, the degree of delamination (area fraction of the anode delaminated) varied from 80% to 90%. The cathode layer from the untested cells, on the other hand, remained well adherent to the electrolyte in all tests.

Table 3.1 summarizes the extent of anode delamination observed after the electrochemical measurements for the cells tested at four different voltages. Also shown are the average degradation rates of ohmic and non-ohmic resistances from 20 to 90 hours after the beginning of each test. The 0.8 volt tested cells exhibit an initial improvement in the performance for the first 20 hours. Degradation rates of ohmic and non-ohmic resistances and degree of anode delamination increase with voltage bias level.

Table 3.1. Rates of ohmic resistance (R_Ω) and non-ohmic resistance ($R_{non\text{-}\Omega}$) degradation between 20 and 90 hours, and degree of anode delamination as a function of applied voltage.

Applied voltage (V)	R_Ω degradation rate ($\Omega \cdot cm^2$/ 1000 h)	$R_{non\text{-}\Omega}$ degradation rate ($\Omega \cdot cm^2$/ 1000 h)	Degree of anode delamination
0	0.16	-13.94	0%
0.3	0.73	-1.51	80%
0.5	2.31	0.89	85%
0.8	5.63	3.83	100%

3.3.2. Compound formation

Electrode–electrolyte interaction and interfacial compound formation were examined using the X-ray diffraction technique. Fig. 3.5a shows x-ray diffraction patterns from electrolyte surfaces of electrochemically tested and untested cells after dissolving of the electrodes in hydrochloric acid. Diffraction patterns are shown from as-received, as-fabricated, and OCV cells as well as electrically tested cells at 0.3, 0.5, and 0.8 V for 100 hours. As the observed peaks are dominated by the yttria-stabilized zirconia electrolyte substrate, the y scale (peak intensity) was magnified to reveal the lower-intensity peaks of reaction compounds. The lanthanum zirconate ($La_2Zr_2O_7$) diffraction pattern (JCPDS 00-050-0837) is identified for the electrically tested cells. The intensity of the zirconate peaks increases with the applied voltage. XRD patterns of the cathode and anode side surfaces of the electrolyte of electrically tested cells (Fig. 3.5b) show that lanthanum zirconate is only present on the anode side of the cells. Also visible in Fig. 3.5 are small residual peaks of YSZ from copper Kβ radiation.

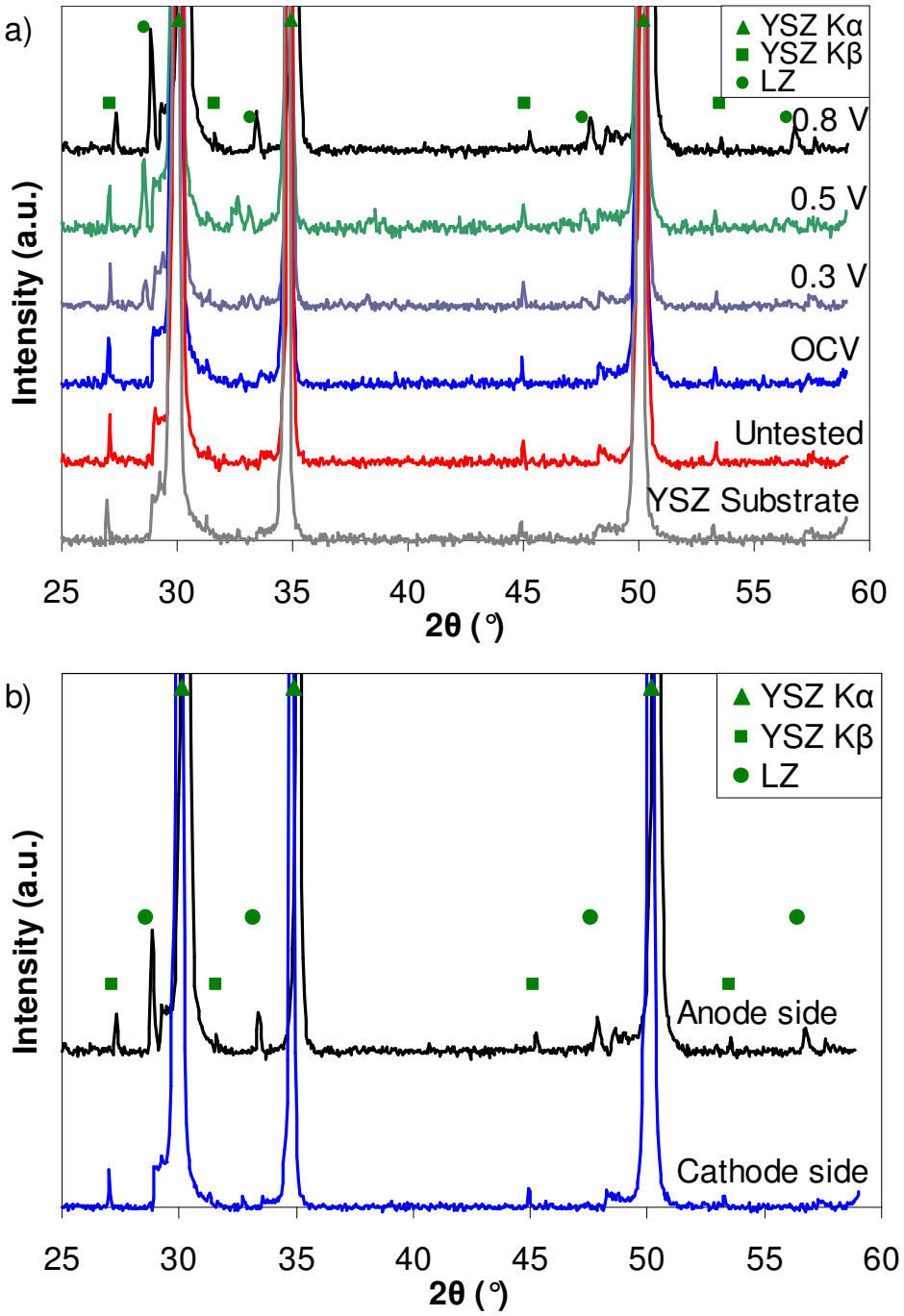

Fig. 3.5. X-ray diffraction patterns of electrolyte surfaces after hydrochloric acid treatment. a) Anode side before and after testing at various voltages; b) Anode and cathode sides after testing at 0.8 V. (▲,■): $(ZrO_2)_{0.92}(Y_2O_3)_{0.08}$ (JCPDS 01-070-4431); (●): $La_2Zr_2O_7$ (JCPDS 00-050-0837).

3.3.3. Morphological observations and chemical analysis

The surface morphology of the as-received YSZ electrolyte is shown in Fig. 3.6. The surface shows typical dense granular structure with well-defined grain boundaries and localized isolated pores formed during sintering. A fractured electrolyte cross section showed the YSZ to be uniformly dense throughout its thickness. Fig. 3.7 shows the LSM electrode surface morphology before and after electrochemical measurements and delamination. The as-sintered electrodes (Fig. 3.7a) are 30-40% porous with a particle size in the range of 1–2 μm. Thermal grooving on the LSM grains is evident on the surface. Electrode surface morphology (in contact with the electrolyte) does not show noticeable changes due to testing (Fig. 3.7b). This observation is distinct from the reported LSM disintegration [32].

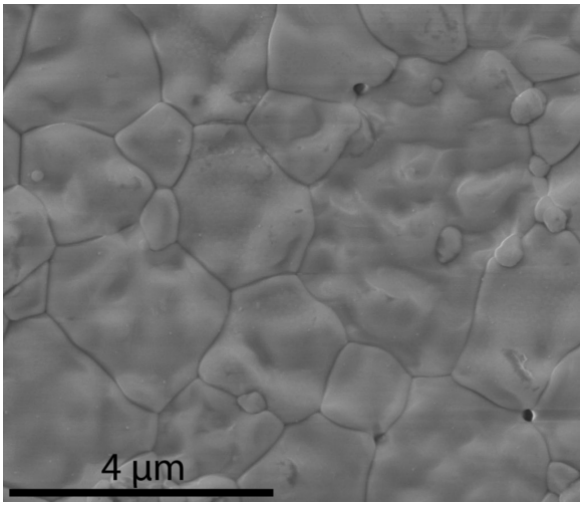

Fig. 3.6. Scanning electron micrograph of as-received electrolyte surface.

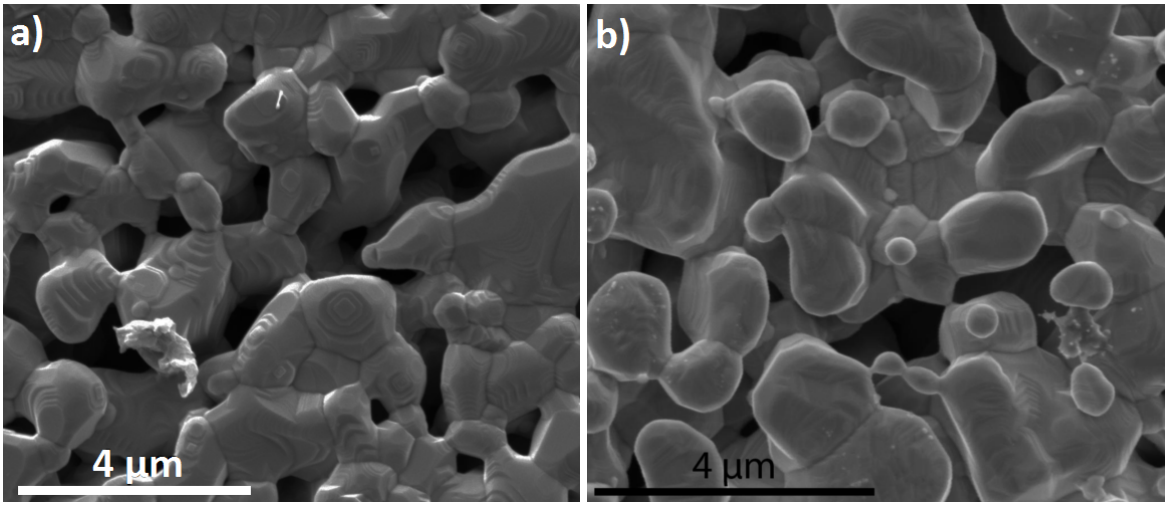

Fig. 3.7. Scanning electron micrographs of LSM electrode surfaces. a) Electrode surface as sintered; b) Anode surface after delamination in a cell tested at 0.8 V.

The electrode-electrolyte interface morphologies (obtained after the dissolution of electrode) of untested and electrochemically tested cells are shown in Fig. 3.8. Fig. 3.8a shows the surface morphology as developed on the YSZ after screen printing and sintering of the electrodes. The electrolyte maintains its dense granular structure with evidence of the formation of a peripheral impression of the electrode in the form of elevated ridges. The observed surface morphology was not altered by subjecting cells to 840 °C for 100 hours with no applied voltage (OCV). Furthermore, the morphology on the cathode side was not altered in cells tested under applied voltage. Fig. 3.8b shows the electrochemically active anode–electrolyte interface of a cell exposed to 0.3 V for 100 hours. The active YSZ surface shows broadening of the elevated ridges and formation of small particles that cover part of the active YSZ surface. These changes are present throughout the entire anode–electrolyte interfacial area. Fig. 3.8c shows the anode–electrolyte interface from a cell exposed to 0.5 V for 100 hours. The electrolyte surface morphology appears similar to that observed on cell

tested at 0.3 V, however, the extent of compound formation and grain boundary delineation increases. The elevated ridges are wider and the contacting electrolyte surfaces show more pronounced roughening as well as higher coverage due to the formation of surface reaction products. Many of the YSZ grain boundaries have opened up into long connected pores. Fig. 3.8d shows the anode YSZ surface from a cell exposed to 0.8 V for 100 hours. The reaction product coverage is further exaggerated compared to the 0.3 V and 0.5 V cells. Grain boundary pores are also present.

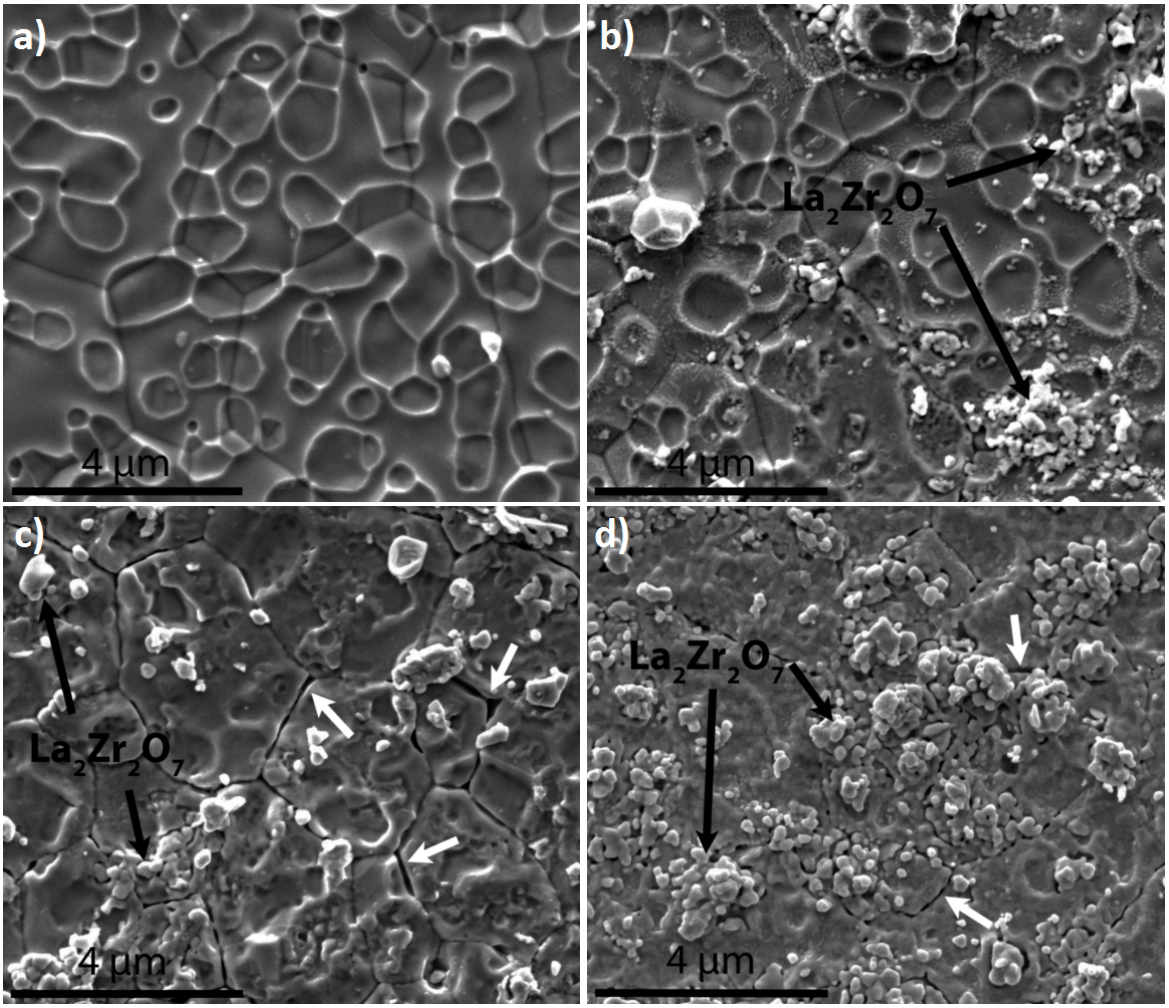

Fig. 3.8. Scanning electron micrographs of anode-side electrolyte surface morphologies after dissolving LSM in hydrochloric acid. Each cell was tested at a different voltage for 100 hours. Black arrows indicate lanthanum zirconate particles and white arrows indicate YSZ grain boundary porosity. a) Open circuit voltage (0 V); b) 0.3 V; c) 0.5 V; d) 0.8 V.

Energy dispersive x-ray spectroscopy of the anode-side electrolyte after testing at 0.8 V showed some lanthanum, strontium, and manganese left by the anode after delamination, in addition to the expected zirconium and yttrium from the electrolyte (Fig. 3.9a). After

treating with hydrochloric acid, the strontium and manganese were removed, but lanthanum remained, which is consistent with the XRD detection of lanthanum zirconate phase (Fig. 3.9b).

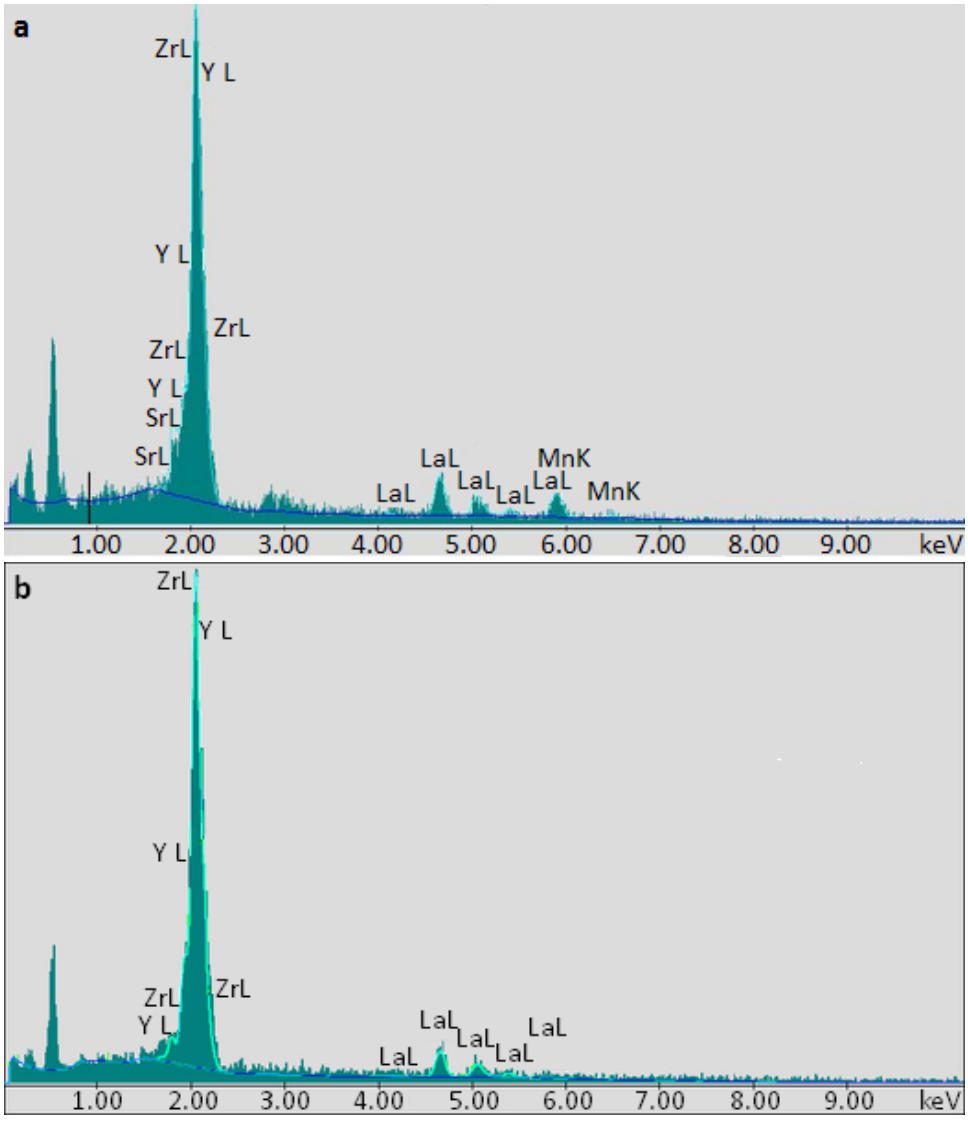

Fig. 3.9. Energy-dispersive X-ray spectroscopy of anode-side active electrolyte surface after testing at 0.8 volts. a) Before hydrochloric acid treatment; b) After treatment.

In summary, an increase in applied voltage on symmetric cells increases:

1. Degradation rate

2. Fraction of anode area delaminated from electrolyte

3. Lanthanum zirconate at anode-side electrolyte surface

4. Morphological changes on anode-side electrolyte surface including elevated ridge broadening and grain boundary porosity formation

3.4. Discussion

Electrochemical testing of cells under impressed voltage conditions measured increases in both ohmic and non-ohmic resistances with the applied voltage. Lanthanum zirconate formed at the anode–electrolyte interface, and the anode-side electrolyte surface experienced morphological changes including grain boundary porosity formation. A mechanism inclusive of changes in the electrical performance, interface morphology changes and compound formation has been developed and presented.

3.4.1. Electrochemical observations

The electrochemical measurements show a correlation between applied bias voltage, anode delamination and increases in both ohmic and non-ohmic resistances (Table 3.1). The initial decreases in ohmic and non-ohmic resistances (Figs. 3.2–3.3) are explained by well-documented electrode conditioning process under cathodic current [64,65] and in LSM-YSZ composite electrodes under anodic current [60]. Jiang et al. have also proposed a

re-equilibration process of surface strontium being responsible for the observed decrease in electrode resistance under cathodic currents [64]. Backhaus-Ricoult et al. related the improvement to activation of the manganite cathode due to an extension of the active area for oxygen incorporation from the triple phase boundary line to the free electrolyte surface due to mixed-conducting characteristics induced by manganese doping of the electrolyte [65].

The activation periods are 20, 50, and 80 h for cells tested at 0.8, 0.5, and 0.3 V, respectively, as these are the times at which the non-ohmic resistances reach their minimum values. The end of the activation period can be interpreted as the time when the rate of degradation exceeds the rate of activation. Lower voltage extends the activation period because both the activation processes and onset of degradation are slower at low currents. The long activation period in the 0.3 V tested cell is responsible for a net decrease in non-ohmic resistance as shown in Table 3.1.

The subsequent increase in the ohmic and non-ohmic resistance is consistent with loss of contact and delamination at the anode–electrolyte interface as demonstrated theoretically [66] and experimentally [30]. The observed increase in ohmic resistance is attributed to the formation of poorly-conducting $La_2Zr_2O_7$ and the loss of contact area at the anode–electrolyte interface. The increase in non-ohmic resistance is explained through the loss of triple phase boundary length resulting in a decrease in the area available for oxygen reduction and evolution. Degradation at the cathode side is considered negligible as no visible morphological or chemical changes were observed at the cathode-electrolyte interface after electrochemical testing.

3.4.2. Compound formation and morphological observations

Microscopic observations and X-ray diffraction indicate that major electrode–electrolyte interfacial changes are limited to the anode–electrolyte interfaces of cells operated under electrical bias conditions. The interface morphology and reaction products formed under the experimental conditions remain similar; however, the severity changes with the applied bias.

Since lanthanum zirconate was identified only on the anode–electrolyte interface of cells tested under applied voltage, the formation is attributed to the evolution of oxygen at that interface. Lanthanum zirconate formation at the anode–electrolyte interface is attributed to the following oxidative reactions [22,67,68]:

$$LaMnO_{3+\delta} + zZrO_2 + \left(\frac{\delta' - \delta}{2} + \frac{3z}{4}\right)O_2(g) \leftrightarrow La_{1-z}MnO_{3+\delta'} + \frac{z}{2}La_2Zr_2O_7 \qquad (3.1)$$

$$LaMnO_3 + ZrO_2 + 0.25O_2(g) \leftrightarrow 0.5La_2Zr_2O_7 + MnO_2 \qquad (3.2)$$

In these reactions, strontium has been excluded for simplicity since lanthanum content in LSM is significantly higher than that of strontium. Eq. (3.1) applies mainly to B-site (Mn) deficient LSM since the reaction removes lanthanum from the A-site (La,Sr), whereas the LSM used in this study is A-site deficient. This leaves Eq. (3.2) as the most likely pathway for lanthanum zirconate to form at high oxygen partial pressures. This reaction is equivalent to Eq. (1.9) with x = 0 and y = 2. The Gibbs free energy of Eq. (3.2) is positive at 840 °C and atmospheric oxygen pressure, but decreases with higher oxygen pressures due to oxygen being a reactant, as follows:

$$\Delta G = \Delta G^{\circ} + RT\,ln\left(\frac{a_{LZ}^{0.5}a_{MO}}{a_{LM}a_{ZO}a_O^{0.25}}\right) \qquad (3.3)$$

In Eq. (3.3), ΔG° is standard Gibbs free energy, R is the gas constant, T is temperature, and the a_i terms in parentheses are the activities of the species of Eq. (3.2) in terms of the reaction quotient. Using the thermodynamic data of Chen [67] at 840 °C, the Gibbs free energy of Eq. (3.2) becomes negative at oxygen partial pressure above approximately 3.7 atm, indicating a favorable forward reaction. Calculations for the oxygen pressure buildup at the anode–electrolyte interface yield a theoretical maximum of 10^{13} atm at 0.8 V and 10^4 atm at 0.3 V and 840 °C (based on equations from [29]). However, the actual maximum pressure is better estimated from the mechanical strength of the LSM anode, approximately 25 MPa (250 atm) at room temperature [69]. Noting that LSM strength does not appreciably decrease at high temperatures [70], the formation of lanthanum zirconate is thermodynamically favorable by Eq. (3.2) due to oxygen partial pressure above 3.7 atm. Since the oxygen partial pressure at the cathode-electrolyte interface will be no greater than atmospheric oxygen pressure, lanthanum zirconate formation by Eq. (3.2) is not expected on the cathode side. These findings are in agreement with the experimental observations of lanthanum zirconate on the anode side only.

The formation of pores along the YSZ grain boundaries (Figs. 3.8c,d) is associated with development of high internal oxygen pressure (as calculated) near the anode–electrolyte interface. The high pressure results from the oxidation of oxygen ions to oxygen gas at defects or closed pores near the YSZ surface, which leads to additional pore formation and damage to the electrolyte [29,71].

The as-sintered sample revealed the formation of an impression of the LSM in the YSZ in the form of ridges as explained by the nucleation of epitaxial (Mn)-YSZ at the LSM-YSZ triple phase boundary (TPB) during sintering [22,72,73]. It has been proposed that the

diffusion of manganese into the YSZ results in an excess of lanthanum in the LSM near the electrode–electrolyte interface and subsequent surface diffusion of La^{3+} and Zr^{4+} cations towards the TPB causes the formation of ridges and a lanthanum zirconate phase. Although the evidence for cation diffusion is seen in the form of thermal grooving in both LSM (Fig. 3.7a) and YSZ (Fig. 3.8a) [74], lanthanum zirconate did not form in detectable quantities in the as-sintered condition in the current study. During voltage application, the ridges broaden due to additional surface diffusion and lanthanum zirconate formation (Figs. 3.8b,c,d).

3.4.3. Anode delamination

Anode delamination is proposed to result from the development of a weakened anode-electrolyte interface due to formation of lanthanum zirconate under electrical testing as schematically shown in Fig. 3.10. The as-sintered interface (Fig. 3.10a) shows the initial ridge formation of YSZ at the triple phase boundary due to cation diffusion and surface migration as previously discussed [22]. Under electrochemical testing, oxygen ions transport through the YSZ electrolyte via bulk and grain boundary diffusion from the cathode to the anode side. Oxygen ions at the YSZ grain boundaries and the anode-side LSM-YSZ interface (Fig. 3.10b) are oxidized to oxygen gas to provide electrons necessary for current flow. The YSZ grain boundaries develop pores near the interface due to high oxygen pressure. Lanthanum zirconate and manganese dioxide similarly form according to Eq. (3.2), and accumulate at the LSM-YSZ interface (Fig. 3.10c). The poor conductivity of lanthanum zirconate [22] is also responsible for degradation and for part of the ohmic resistance

increase. The processes continue with electrical testing, resulting in the coverage of entire anode-side LSM-YSZ with reaction products severely weakening the interface (Fig. 3.10d).

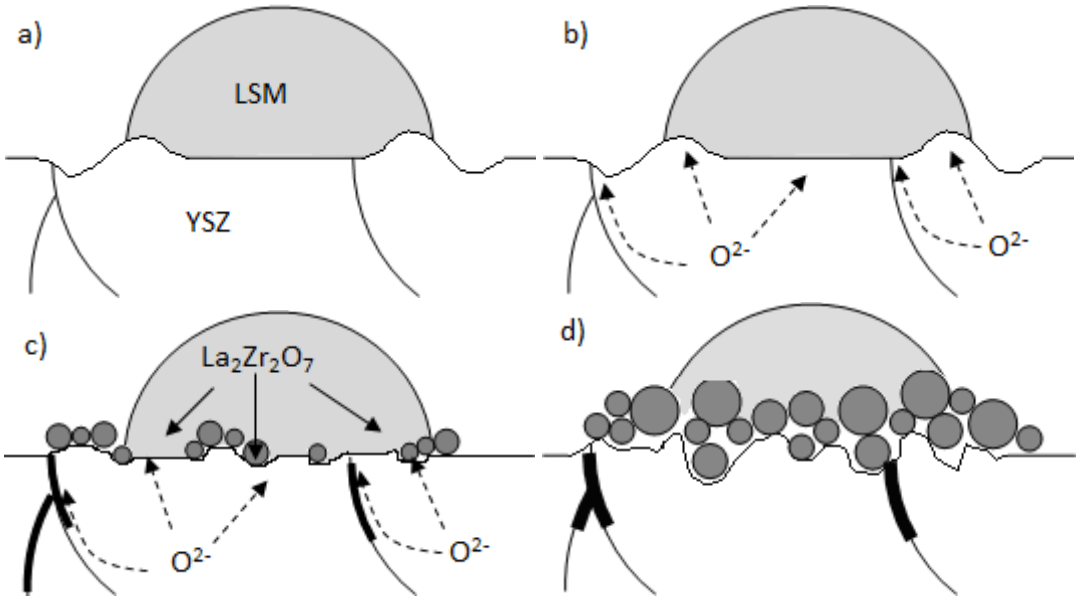

Fig. 3.10. Schematic of chemical and morphological changes at the SOEC anode-electrolyte interface; a) As-sintered LSM-YSZ interface; b) Voltage application initiated; c) Voltage application in progress; d) Voltage application complete.

Stresses developed at the interface due the mismatch in the thermal expansion coefficients of lanthanum zirconate, yttria stabilized zirconia and lanthanum strontium manganite also contribute to fracture and the observed delamination. It is known that lanthanum zirconate has a significantly lower thermal expansion coefficient (7.0×10^{-6} °C^{-1}) than either YSZ (9.6×10^{-6} °C^{-1}) or LSM (11.6×10^{-6} °C^{-1}) [68]. These findings are in contrast to previous observations [29,32] which attribute delamination solely to mechanical breakdown of the electrolyte or electrode material. The high oxygen pressure at the interface will exacerbate the delamination of the anode and electrolyte.

3.5. Summary

Symmetric cells of the configuration Ag-Pd/LSM/YSZ/LSM/Ag-Pd were fabricated and electrically tested under a range of operating conditions in order to understand the anode delamination behavior commonly observed in SOEC. Electrical performance degradation was measured with time at various applied voltages ranging from 0 to 0.8 V. Anode delamination from the electrolyte was observed in cells tested at voltages greater than 0 V. Elemental analysis of the same surfaces detected the formation of lanthanum zirconate. Microstructural analysis of the post-test electrolyte surfaces revealed extensive morphological changes such as the development of elevated ridges, small lanthanum zirconate particles, and grain boundary porosity. Lanthanum zirconate formation and morphological changes at the anode–electrolyte interface increased in severity with applied bias, while the cathode–electrolyte interface remained relatively unchanged. An anode delamination mechanism based on morphological change and compound formation at the anode–electrolyte interface was proposed.

CHAPTER 4: ELECTRICAL AND MORPHOLOGICAL STABILITY OF SILVER-BASED ELECTRODES IN SOLID OXIDE CELLS

4.1. Objectives

Silver is a promising material for inclusion in SOC electrodes due to its good catalytic activity at lower temperatures and chemically inert nature. It is also significantly less expensive than other precious metals with similar properties, such as gold and platinum. However, there has been little research completed on the stability of silver-based electrodes and of interfaces between silver and other SOC components. In this work, silver-palladium-based air electrodes have been electrochemically evaluated in contact with YSZ electrolytes using a symmetric cell configuration. The cells were operated in air to reproduce the standard atmosphere in contact with air electrodes. Trace impurities are known to cause morphological instability at electrode-electrolyte interfaces. To observe the effect of interfacial impurities, the interfaces have also been examined in the presence of a silicon oxide interlayer. Mechanisms for interfacial instability and the implications on cell performance are discussed.

4.2. Experimental

Cells and test fixtures were fabricated as described in section 2.1. Cells were fabricated using three electrode compositions: Ag-Pd, $(Ag\text{-}Pd)_{0.82}$-$GDC_{0.18}$, and $(Ag\text{-}Pd)_{0.68}$-$GDC_{0.32}$. The latter two compositions were composites, made by mixing Ag-Pd and GDC in

the appropriate ratios in a mortar and pestle, screen printing on YSZ substrates, and sintering at 850 °C. Symmetric cells had the configuration Ag-Pd/$(Ag\text{-}Pd)_x$-GDC_{1-x}/YSZ/$(Ag\text{-}Pd)_x$-GDC_{1-x}/Ag-Pd, with x = 1, 0.82, or 0.68. Sealing was not used, as both electrodes were exposed to air. Flowing air (less than 2% water vapor) was delivered to the cathode side at 100 sccm. Due to the identical atmosphere on both sides of the cell, OCV was approximately 0 V. An operating temperature of 750 °C was used in order to balance the requirements of low temperature for silver stability and high temperature for acceptable YSZ ionic conductivity. For each cell, a constant voltage was applied for 100 hours and the cell current was recorded every 60 seconds throughout the duration of the test. Cells were tested in a wide voltage range (0 to 0.8 V) to assess the degradation under simulated nominal and accelerated cell operating conditions. Impedance measurements were performed at four hour intervals under the same voltage bias. Experiments were repeated several times at each condition to ensure reproducibility.

Representative impurity contents of the symmetric cell components are given in Table 4.1. The impurity contents of the YSZ substrates and the Ag-Pd paste were not available; the data given represent those of commercial YSZ, silver, and palladium powders. The impurity contents of the mesh and wires are those of different batches of these products from the same supplier.

Table 4.1. Representative impurity contents of the various components of the symmetric cells given in parts per million (ppm) by mass.

Component	Na	Fe	Cu	Ca	Al	Zn	Cr	Si
YSZ	600	30	-	-	50	-	-	40
Ag in paste	870	7	4	30	4		3	-
Pd in paste	387	1355	268	170	516	516	253	-
Ag mesh	-	10	90	-	-	-	-	-
Ag wire	6	1	2	41	12	-	-	8

In order to directly observe the effect of foreign impurity phases on the electrode-electrolyte interfaces, a layer of silicon oxide was deposited on both sides of a YSZ electrolyte substrate. A water-based colloidal silicon oxide suspension (Buehler MasterMet) was diluted by a volumetric factor of 300 with distilled water, and 0.5 g of the resulting solution was pipetted onto the YSZ substrate. The suspension was allowed to dry at room temperature and the final silicon oxide layer thickness was approximately 1 μm. The YSZ was subsequently screen-printed with Ag-Pd paste and electrically tested at 0.8 V in an identical manner to cells without the silicon oxide layer.

4.3. Results

4.3.1. As-prepared symmetric cells

After screen-printing and drying the Ag-Pd paste on a YSZ substrate, the morphology in Fig. 4.1a is observed. The average particle size is approximately 200 nm. After bisque-firing, a bimodal particle size distribution is observed as in Fig. 4.1b. Average particle sizes are 200 nm and 1.5 μm. After sintering, average particle size increases to 7 μm (Fig. 4.1c). The effect of high-temperature treatment is thus significant particle sintering and densification. Final sintered thickness is about 10 μm.

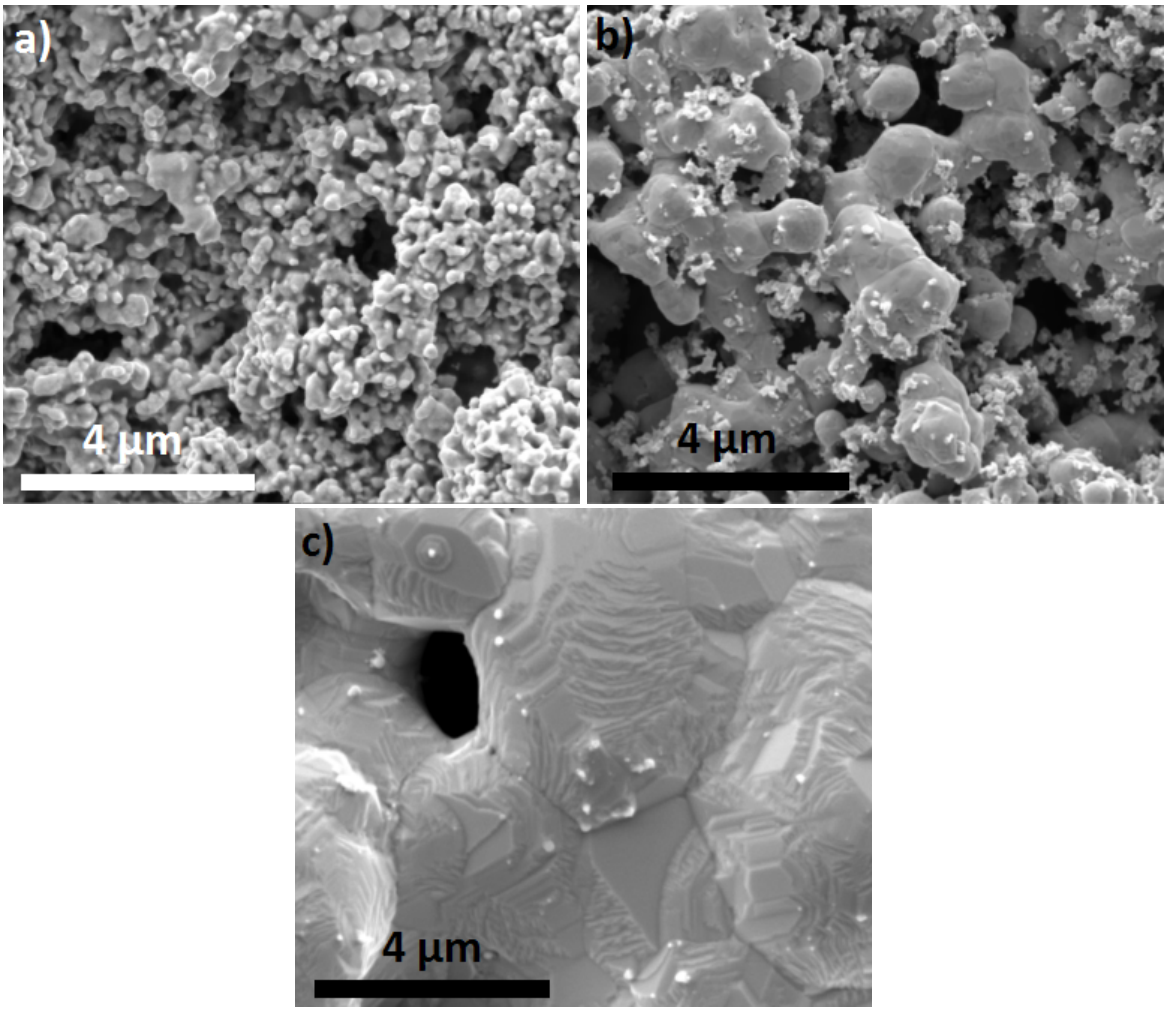

Fig. 4.1. SEM images of screen-printed, untested Ag-Pd electrode; a) Dried at 80 °C for 1 hour; b) Fired at 450 °C for 1 hour; c) Sintered at 850 °C for 1 hour.

After sintering the three $(Ag\text{-}Pd)_x\text{-}GDC_{1-x}$ compositions at 850 °C, significant differences in morphology are observed (Fig. 4.2). Average silver particle sizes are approximately 7 µm, 3 µm, and 2 µm for x = 1, 0.82, and 0.68, respectively. Average GDC particle size is approximately 150 nm in both composites.

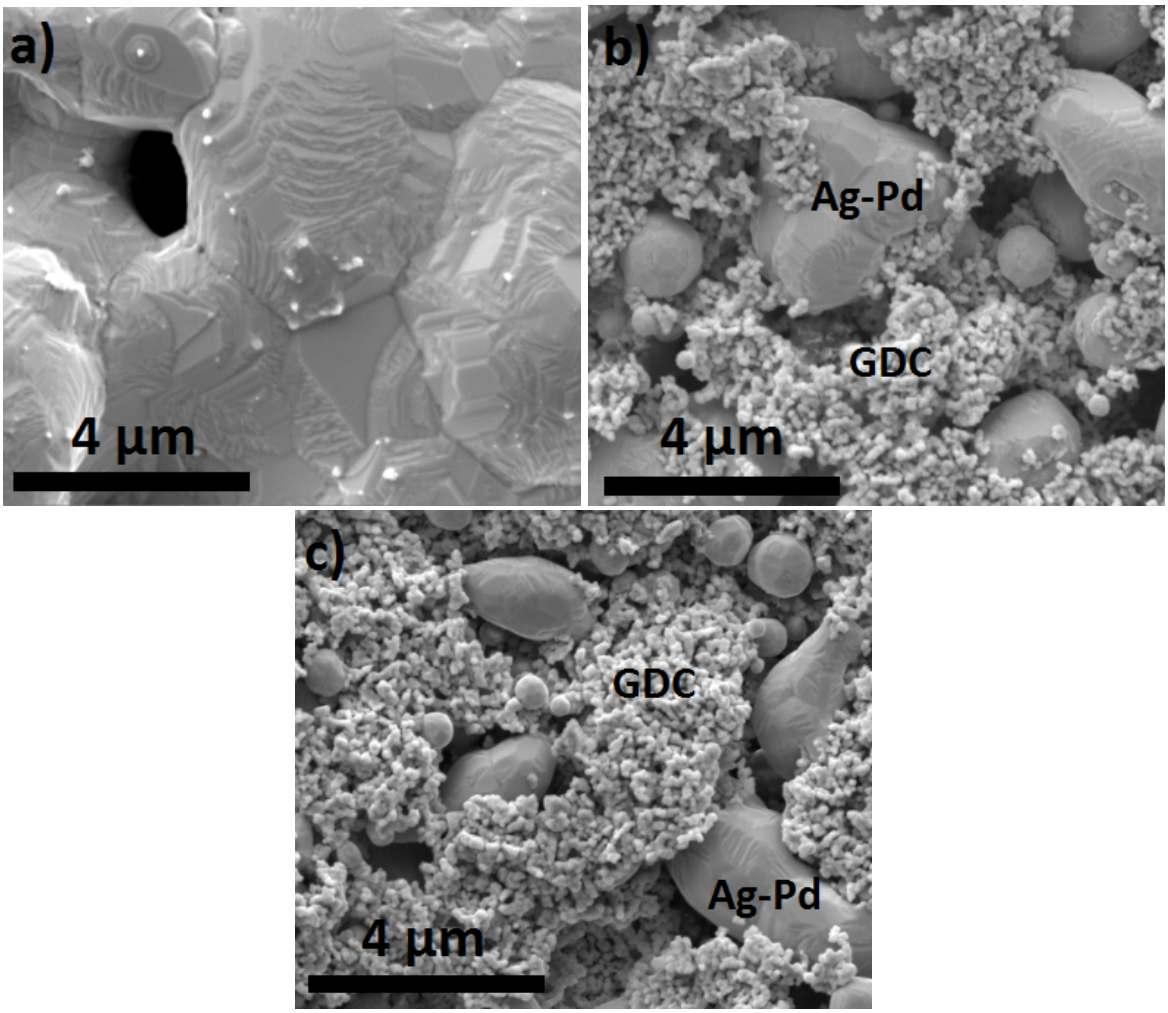

Fig. 4.2. SEM images of $(Ag\text{-}Pd)_x$-GDC_{1-x} electrodes sintered at 850 °C but untested; a) Ag-Pd; b) $(Ag\text{-}Pd)_{0.82}$-$GDC_{0.18}$; c) $(Ag\text{-}Pd)_{0.68}$-$GDC_{0.32}$.

4.3.2. Electrochemical measurements

After heating cells to 750 °C, impedance measurements were taken at zero voltage to establish initial cell performance and determine the degree of cell to cell variation. Among all cells, the relative standard deviation of initial zero bias ohmic resistance was 4% while that of non-ohmic resistance was 14%. Thus, most of the initial cell resistance variation stems from the non-ohmic contribution.

Fig. 4.3 shows typical impedance spectra exhibited by an Ag-Pd symmetric cell at 0.8 V. Ohmic and non-ohmic resistances at each time interval were determined from the high- and low-frequency x-intercepts.

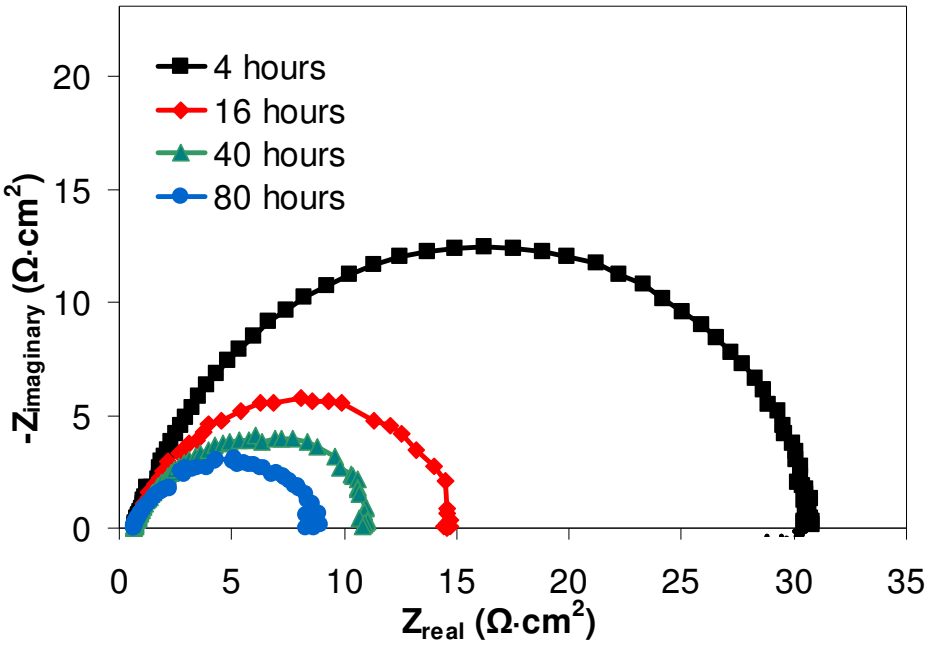

Fig. 4.3. Nyquist plot of impedance spectra from a symmetric cell with Ag-Pd electrodes tested at 0.8 V. For clarity, only four spectra are shown.

The ohmic and non-ohmic resistances taken from the Nyquist plots are plotted as functions of time in Fig. 4.4 for cells with Ag-Pd electrodes at various operating voltages. Cell to cell variation is considerable, particularly for non-ohmic resistance, with variation of over 50% among cells tested at 0.8 V. Within the period of 40 to 100 h, the resistances of some cells increased, while others decreased. Both ohmic and non-ohmic resistances show a decreasing trend for at least the first 8 h of testing. Non-ohmic resistance is inversely related to the applied voltage, and is always significantly higher than ohmic resistance.

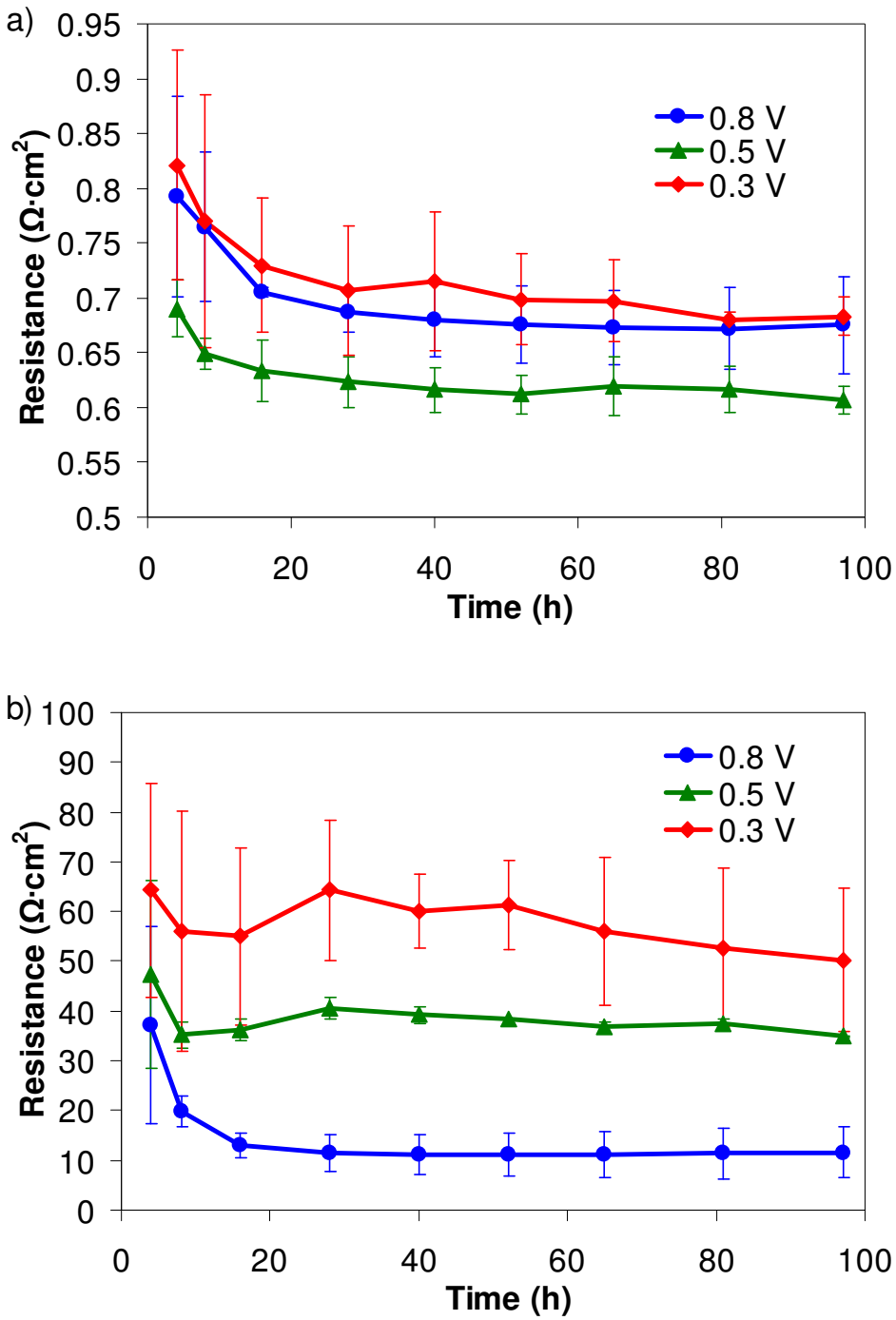

Fig. 4.4. Resistances of symmetric cells tested at 0.8, 0.5, and 0.3 V with Ag-Pd electrodes as functions of time; a) Ohmic; b) Non-ohmic.

Fig. 4.5 shows the ohmic and non-ohmic resistances of cells tested at 0.8 V with $(Ag\text{-}Pd)_x\text{-}GDC_{1-x}$ composite electrodes. The typical trend is an initial resistance decrease followed by stabilization. Ohmic resistance variation increases with higher GDC content, while non-ohmic resistance variation generally decreases with higher GDC content. Steady-state ohmic resistance increases with higher GDC content, while non-ohmic resistance decreases with higher GDC content. The composite electrodes have significantly improved performance due to the large decreases in non-ohmic resistance compared to single phase Ag-Pd. The ohmic resistance of the x = 0.68 composition is significantly higher than the other two, while the non-ohmic resistance of the x = 1 composition is significantly higher than the other two. Therefore the x = 0.82 composition has the lowest total resistance at steady state. Non-ohmic (electrode-associated) resistance for $(Ag\text{-}Pd)_{0.82}\text{-}GDC_{0.18}$ is as low as 0.625 $\Omega\cdot cm^2$ after 100 h, increasing to 0.630 $\Omega\cdot cm^2$ after 160 h (data after 100 h not shown). This corresponds to a degradation rate of 0.08 $\Omega\cdot cm^2$/1000 h, a factor of 50 lower than the degradation of LSM tested at 0.8 V (3.83 $\Omega\cdot cm^2$/1000 h in Table 3.1).

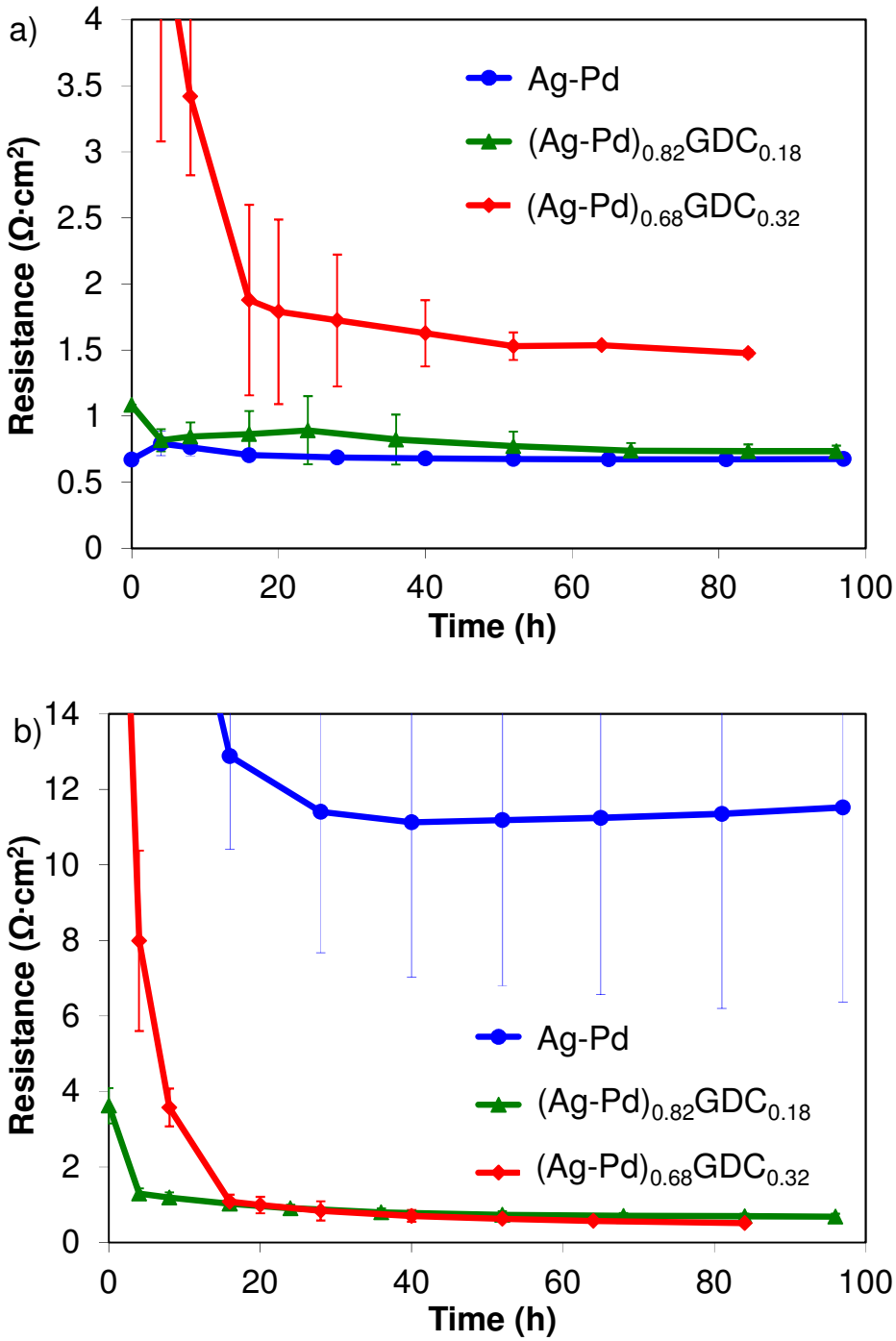

Fig. 4.5. Resistances of symmetric cells tested at 0.8 V with $(Ag\text{-}Pd)_x$-GDC_{1-x} electrodes as functions of time; a) Ohmic; b) Non-ohmic.

4.3.3. Chemical and morphological evaluation of electrochemically tested cells

SEM observation was performed on the electrodes for observation of morphological changes. In cells tested with Ag-Pd electrodes, while the cathodes retained their porous structure in all cases, the anodes of some of the cells showed considerable densification after testing at 0.8 V (Fig. 4.6). The anodes of cells with increasing non-ohmic resistance tended to densify (Fig. 4.6a), while those of cells with decreasing non-ohmic resistance tended to retain their porous structure (Fig. 4.6b). In cells tested at 0.8 V with $(Ag\text{-}Pd)_{0.82}$-$GDC_{0.18}$ composite electrodes, the silver particles agglomerated and densified significantly despite the presence of GDC particles (Fig. 4.6c). Silver agglomeration in the composite was not as severe after testing at OCV (Fig. 4.6d).

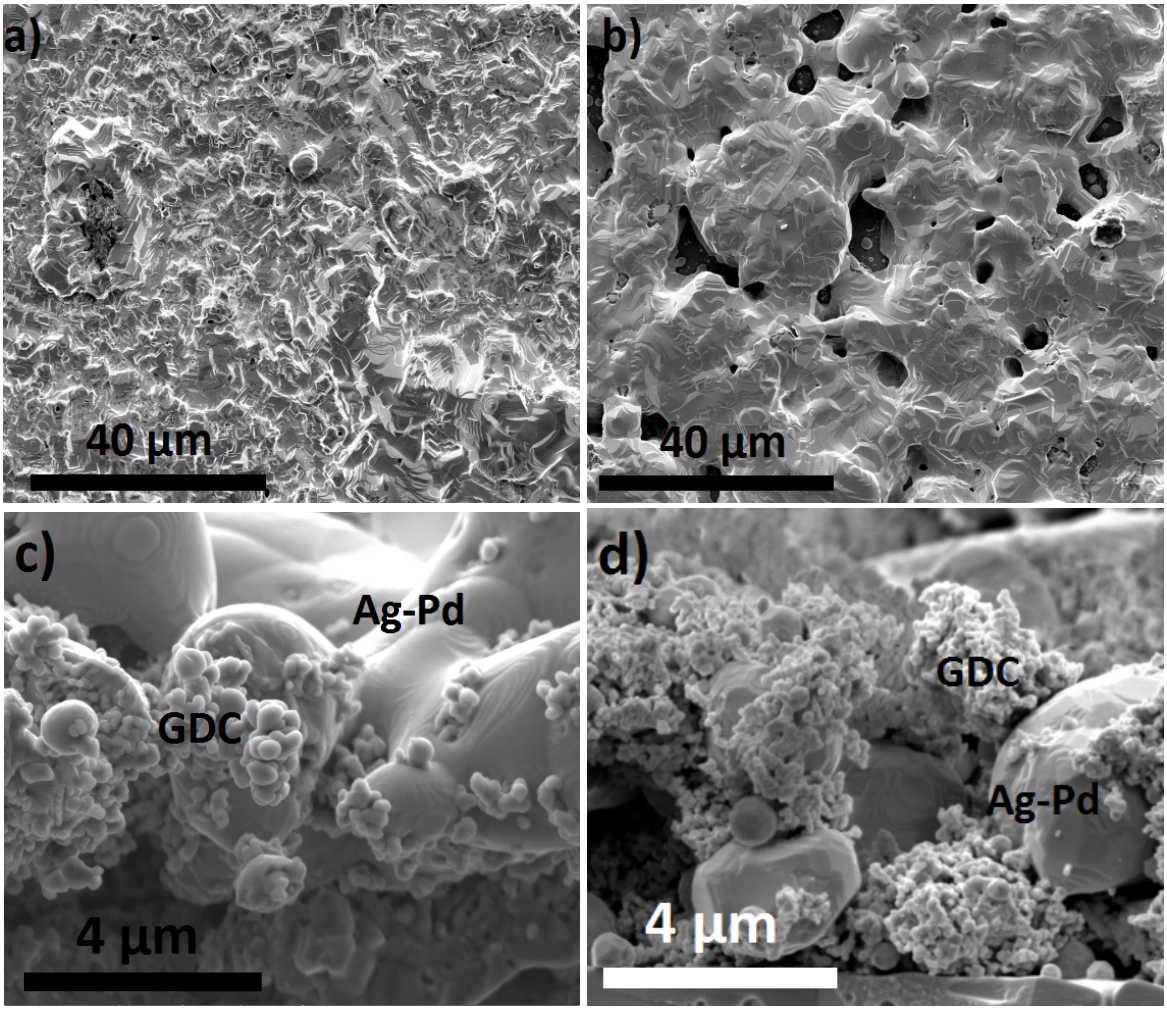

Fig. 4.6. Anodes of symmetric cells tested at 0.8 V; a) Densified Ag-Pd tested at 0.8 V; b) Porous Ag-Pd tested at 0.8 V; c) $(Ag\text{-}Pd)_{0.82}$-$GDC_{0.18}$ tested at 0.8 V; d) $(Ag\text{-}Pd)_{0.82}$-$GDC_{0.18}$ tested at OCV.

X-ray diffraction was performed on the active YSZ surfaces after applying 0.8 V for 100 h at 750 °C to cells with Ag-Pd electrodes and subsequently dissolving the Ag-Pd in dilute nitric acid. The diffraction patterns for both the anode and cathode sides match well with the standard YSZ pattern (Fig. 4.7).

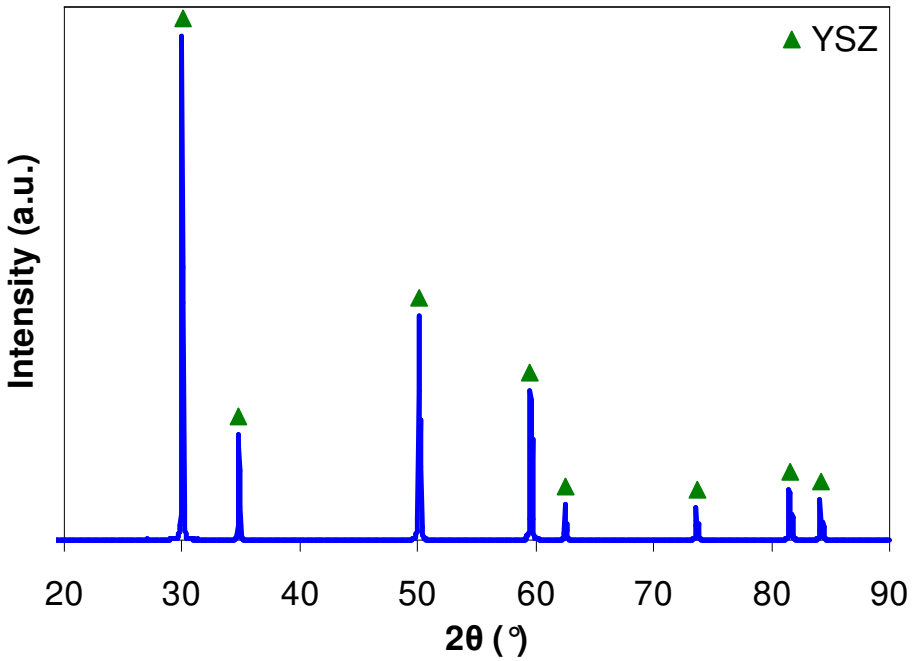

Fig. 4.7. X-ray diffraction pattern of anode-side YSZ surface of symmetric cell after applying 0.8 V for 100 h at 750 °C and dissolving Ag-Pd electrodes in nitric acid. (▲):$(ZrO_2)_{0.92}(Y_2O_3)_{0.08}$ (JCPDS 01-070-4431).

After electrochemical testing of symmetric cells with Ag-Pd electrodes, the cells showed no changes upon initial visual inspection, and the electrodes were still firmly adhered to the YSZ electrolyte. After dissolving the electrodes in nitric acid, the inactive YSZ surface (Fig. 4.8a) has few features except for the grain boundaries and some sparsely distributed small pores. Images that are representative of the morphology in the majority of the electrochemically active YSZ surfaces are shown in Figs. 4.8b (cathode side) and 4.8c (anode side). These surfaces were in contact with the Ag-Pd electrodes during electrochemical testing. In most of the area, the surfaces have minimal morphological changes compared with the inactive YSZ surface, and no significant morphological differences were observed among

cells tested at different positive voltages (0.3, 0.5, and 0.8 V). However, there are a few remaining particles and evidence of a slight imprint from the electrode in many areas.

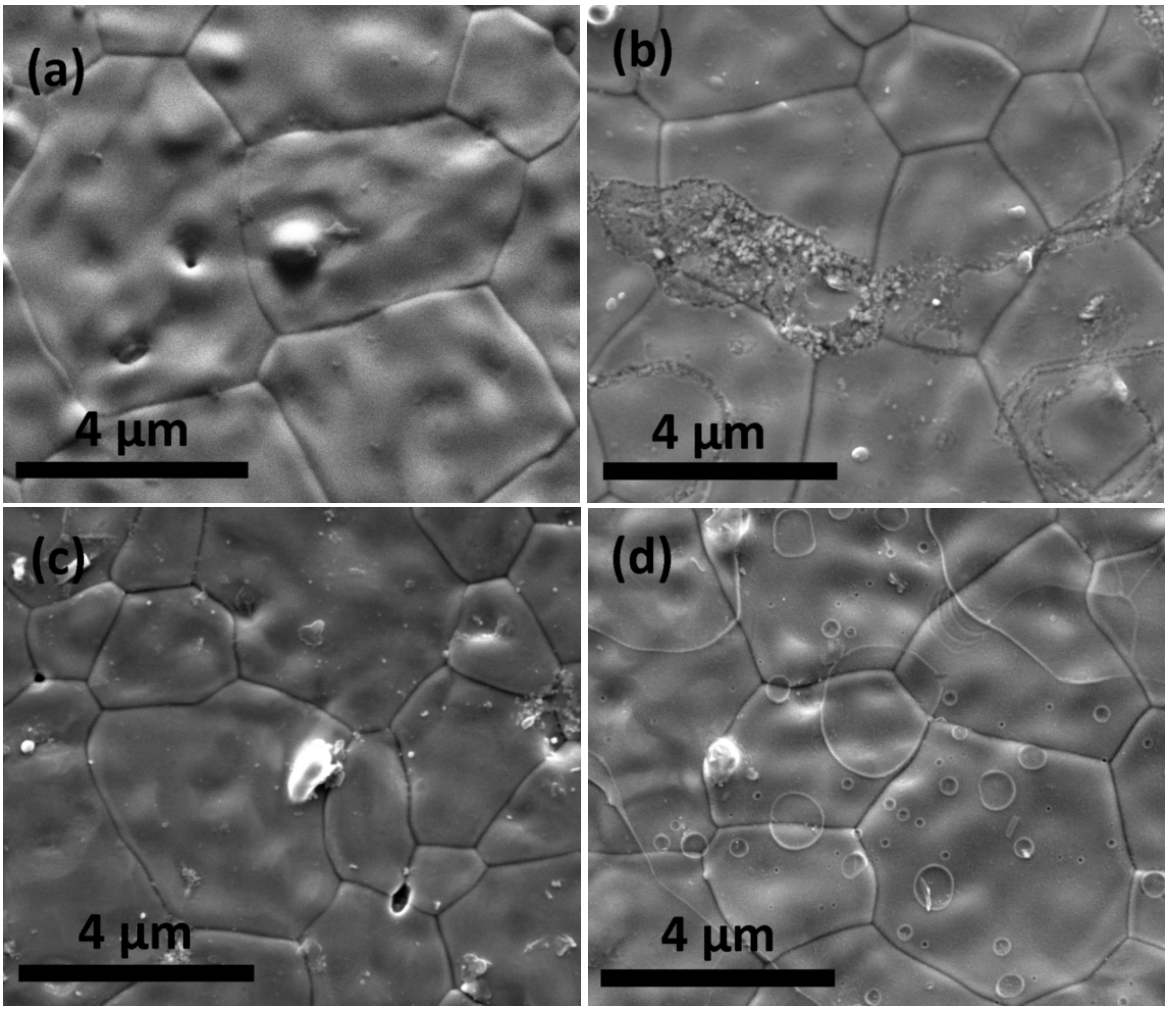

Fig. 4.8. a) b) c) YSZ surface morphologies of symmetric cells after applying 0.8 V for 100 h at 750 °C and dissolving Ag-Pd electrodes in nitric acid; a) Inactive surface; b) Active surface on cathode side; c) Active surface on anode side; d) YSZ surface morphology after sintering with Ag-Pd electrode to 900 °C for 10 h and dissolving electrode in nitric acid.

The silver-YSZ interface was also studied under no voltage load conditions (Fig. 4.8d). Sintering Ag-Pd electrode on YSZ for 10 h at 900 °C only results in a slight imprint of the electrode on the YSZ surface in the form of elevated ridges around the edges of the Ag-Pd grains.

Despite the stability of most of the active silver-YSZ interface, there are a few isolated regions in the active areas that show severe morphological changes (Fig. 4.9). The cathode-side electrolyte has developed surface undulations, with the appearance of small particles (50-200 nm) covering the surface (Fig. 4.9a). On the anode side, the YSZ grain boundaries have become separated, with the separation extending 1-2 μm into the inactive area. The YSZ grains have also developed a complex network of interconnected porosity and surface undulations, with periodicity of 100-200 nm (Fig. 4.9b). This unusual morphology is only observed on a very small portion (less than 1%) of the active area. Cells tested at lower than 0.8 V do not display these morphological changes. There is no discernable pattern as to the location of these regions; they appear randomly distributed within the active area. EDS analysis of the undulated areas usually detects only zirconium, yttrium, and oxygen from the electrolyte, but silicon was also occasionally detected.

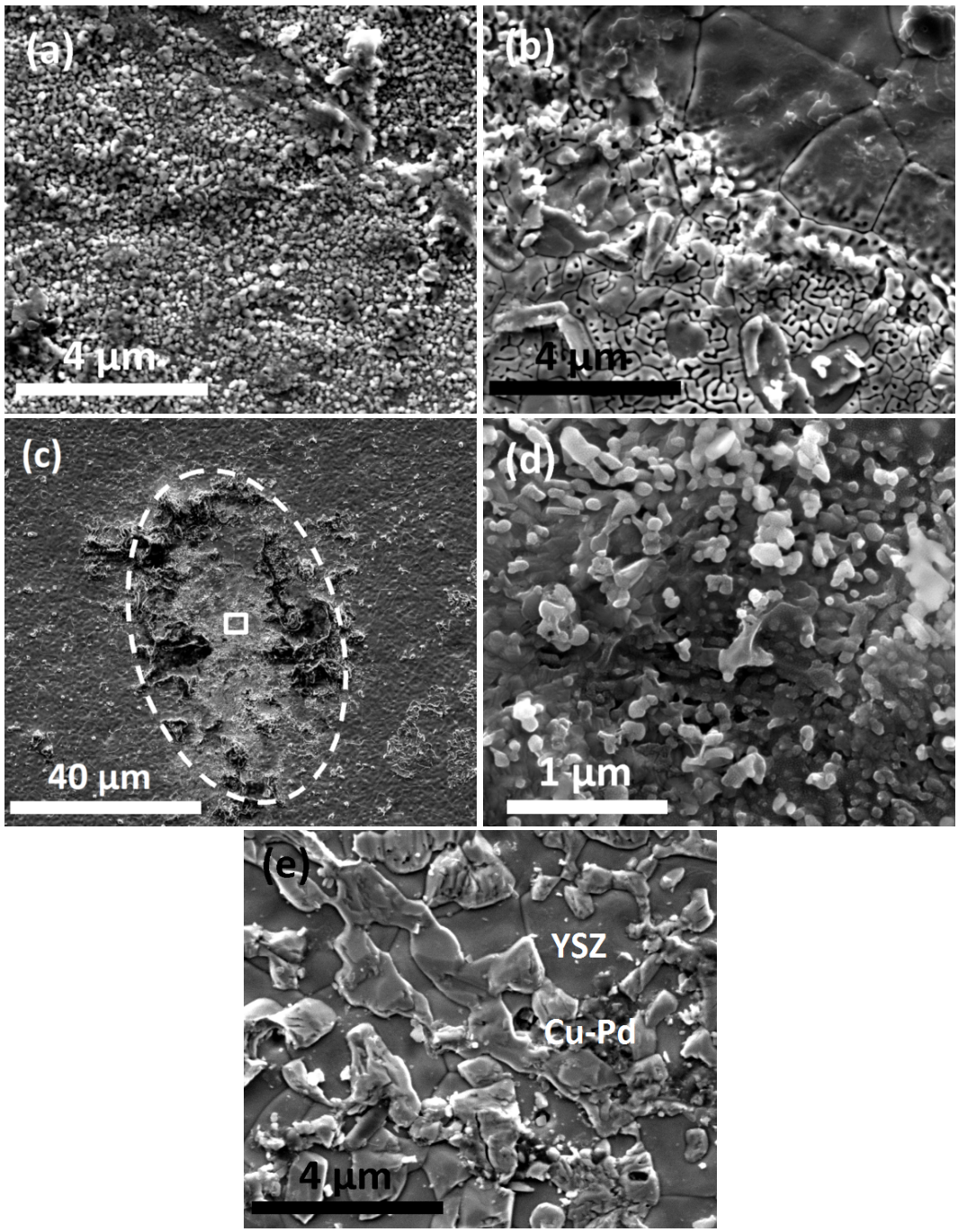

Fig. 4.9. YSZ surface morphologies of symmetric cells after applying 0.8 V for 100 h at 750 °C and dissolving Ag-Pd electrodes in nitric acid. a) Region of damaged active surface on cathode side; b) Region of damaged active surface on anode side; c) Region of damaged active surface on anode side showing ring of impurities; d) High magnification of the location indicated by the box in Fig. 4.9c; e) Copper-palladium deposits on anode side.

Another region of morphological damage on the anode-side electrolyte surface is shown in Figs. 4.9c and 4.9d. The damaged area is surrounded by a ring of impurities that take the form of glassy-phase particles up to 10 μm in diameter. The impurities are primarily silicon-based as detected by EDS (Fig. 4.10). These impurities were not detected in any regions with undamaged YSZ surface. The detected metal impurities include silicon, aluminum, sodium, and copper. These impurities match with those expected from the cell components (Table 4.1).

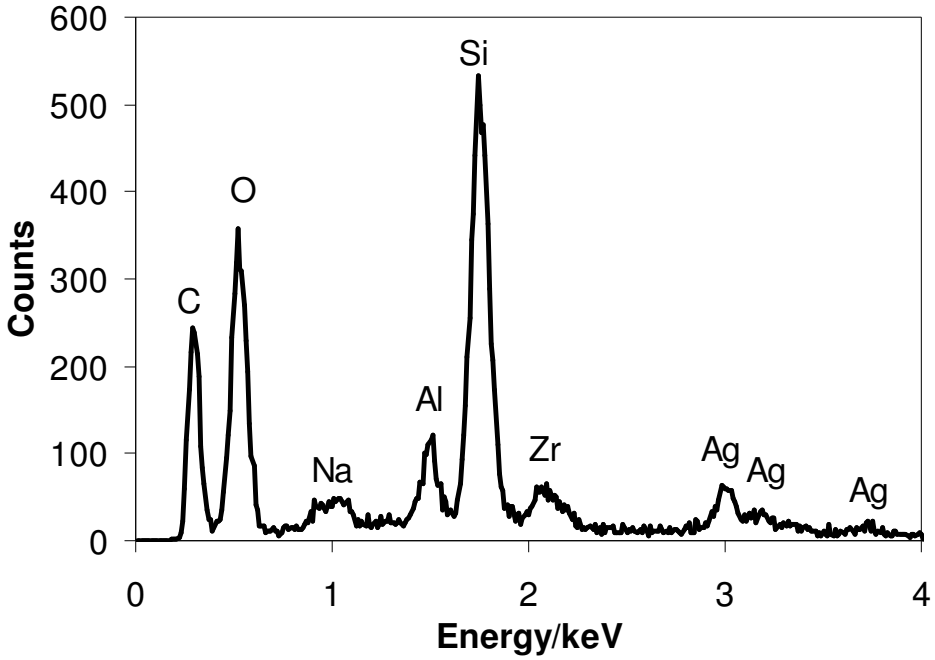

Fig. 4.10. Energy dispersive x-ray spectrum from the impurity ring imaged in Fig. 4.9c.

Other regions in the anode-side active areas have material deposits on top of an otherwise unaltered YSZ surface (Fig. 4.9e). The deposits consist of interconnected particles approximately 1 μm in diameter and less than 1 μm thick. EDS analysis of these regions

shows Cu and Pd in addition to the Zr, Y, and O from the electrolyte. The atomic ratio of Cu to Pd ranges from 1 to 3 across different regions in various cells, averaging 2. The percentage of active area covered by the Cu-Pd deposits varies, but remains less than approximately 10%. The Cu-Pd deposits are randomly (and on a large scale, uniformly) distributed over the entire anode-side active area of each cell, and is observed to a similar degree among cells tested at 0.3, 0.5, and 0.8 V. However, they do not induce YSZ morphological changes under any conditions.

Cross-sectional micrographs of the Ag-Pd electrodes are shown in Fig. 4.11. Si-based impurities are seen in both as-fabricated and post-test electrodes. Impurities were found distributed throughout the thickness of the as-fabricated electrodes. One representative impurity is shown in Fig. 4.11a. In contrast, impurities in the post-test anodes (Fig. 4.11b) were consistently found at the anode-electrolyte interface.

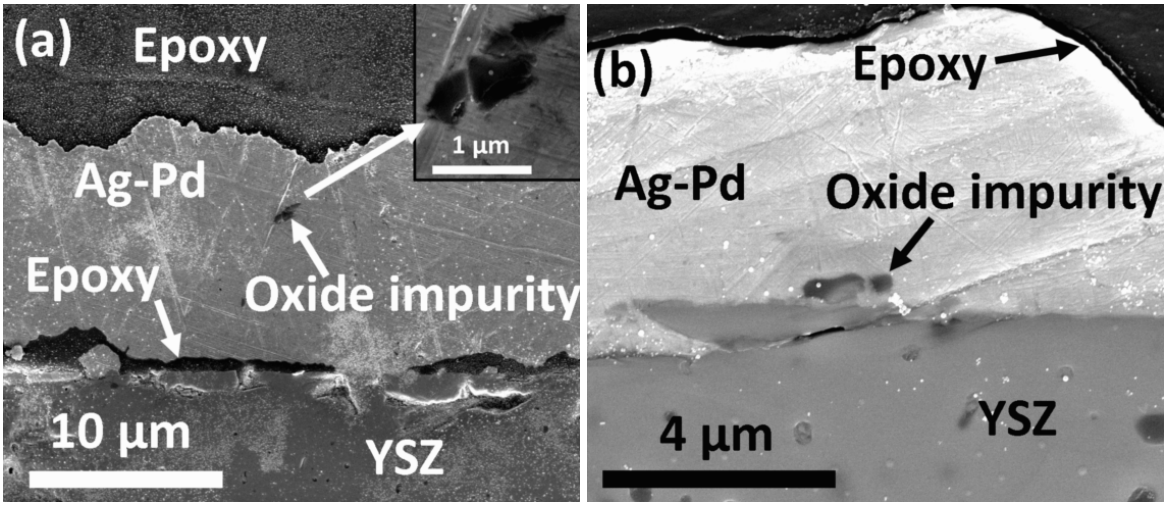

Fig. 4.11. Cross-sectional micrographs of Si-based impurities in Ag-Pd electrodes; a) As-fabricated electrode, (inset) Si-based impurity at increased magnification; b) Anode after testing under 0.8 V.

FIB was used to prepare cross sections of the undulated YSZ surface and impurities (from Figs. 4.9b, 4.9c, 4.9d) for viewing in TEM. Fig. 4.12a verifies the undulations' periodicity of approximately 200 nm. Fig. 4.12b shows one of the impurities from Fig. 4.9c with underlying YSZ undulations. TEM-EDS analysis on the impurity particle shows that it consists of a calcium silicate phase within a silicon oxide phase. The silicon oxide detection is in accordance with the SEM-EDS of a similar impurity particle (Fig. 4.10).

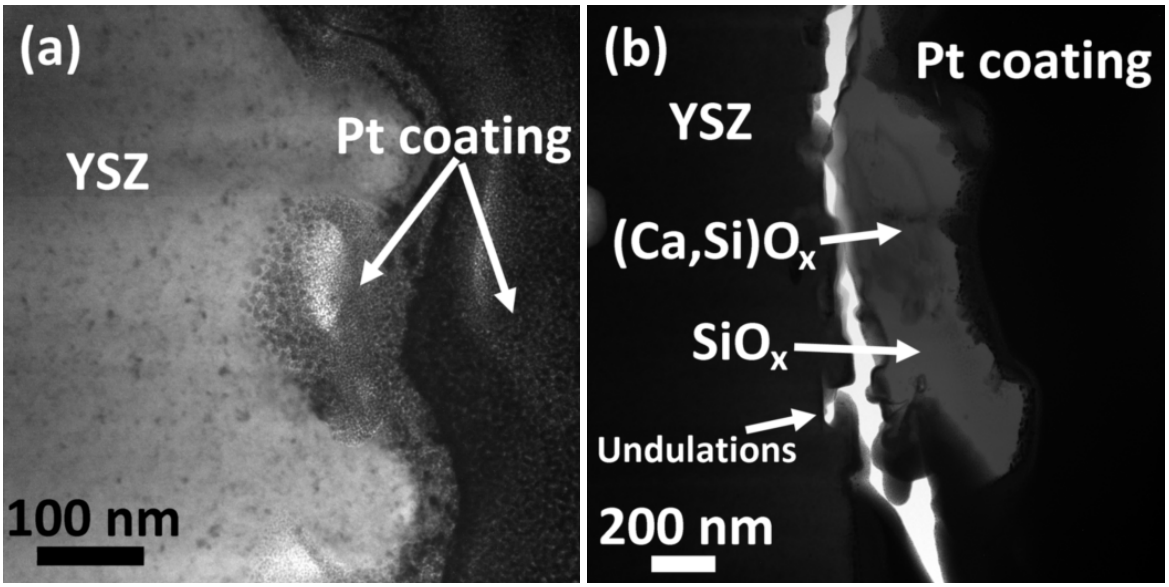

Fig. 4.12. Cross-sectional transmission electron micrographs of the anode-side YSZ surface after testing and dissolving Ag-Pd electrodes in nitric acid; a) Undulated surface as imaged in Figs. 4.9b and 4.9d; b) particle from the impurity ring imaged in Fig. 4.9c, showing underlying YSZ undulations. The white crack is a gap created during sample preparation.

Symmetric cells were prepared using 1 μm silicon oxide interlayers between the YSZ electrolyte and Ag-Pd electrodes and were tested with 0.8 V for 100 h at 750 °C. After dissolving the electrodes in nitric acid, the YSZ surface morphologies were imaged in SEM

(Fig. 4.13). The inactive area (Fig. 4.13a) shows the silicon oxide layer as deposited, which covers the entire YSZ surface but has a slightly cracked and porous structure. Both the anode and cathode side active areas (Figs. 4.13b,c) have undulations distributed across the active surface with approximately 50% coverage. The undulated regions are approximately 2-5 µm in diameter, similar to the size of the Ag-Pd grains. The deposited silicon oxide layer has also undergone morphological rearrangement and only covers about 50% of the active surface.

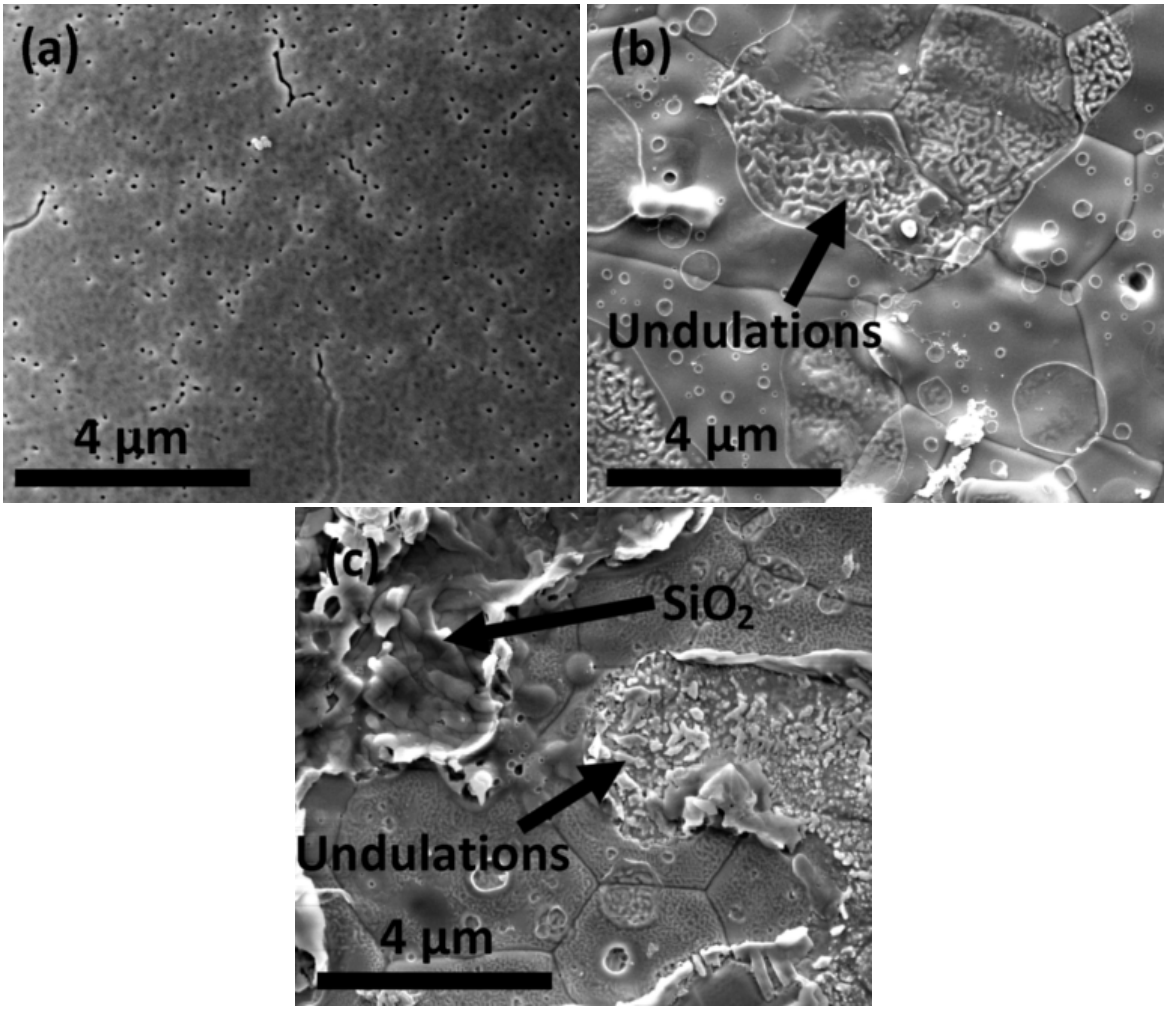

Fig. 4.13. YSZ surface morphologies of symmetric cells with silicon oxide interlayer after applying 0.8 V for 100 h at 750 °C and dissolving Ag-Pd electrodes in nitric acid; a) inactive area showing silicon oxide layer as deposited; b) anode side active area; c) cathode side active area.

4.4. Discussion

4.4.1. Electrochemical observations

The low initial ohmic resistance variation for cells with Ag-Pd electrodes is expected because the electrolyte substrates are commercial and have a uniform composition, thickness, and microstructure. The Ag-Pd electrodes and current collection are applied via screen printing and brush painting, allowing for significant microstructural variation that contributes to initial non-ohmic resistance variation. The initial microstructure-based variation in non-ohmic resistance is worsened by voltage application (Fig. 4.4), with up to 50% variation in cells being tested compared with 14% before testing.

Despite the variation, a few trends are evident. Both the ohmic and non-ohmic resistances show a decreasing trend for at least the first 8 hours of cell testing, which may indicate current-driven removal of a passive surface layer on the electrodes. A similar effect is seen in lanthanum manganite-based electrodes, which have a surface layer with different composition from the bulk before current passage [64]. Higher applied voltage is associated with lower non-ohmic resistance throughout the duration of the tests. This trend is also explained by the removal of a passive surface layer on the electrodes. Higher voltage leads to higher current, which in turn increases electrode passivation and decreases resistance.

Non-ohmic resistance of cells with Ag-Pd electrodes is generally 1 to 2 orders of magnitude above ohmic resistance. The high non-ohmic resistance is attributed to the large particle size and low porosity of sintered Ag-Pd electrodes (Fig. 4.1c), which result in a low

electrode-electrolyte-air triple phase boundary (TPB) length. Low TPB length is associated with a small area for oxygen reduction and reoxidation, and thus lower performance [75].

Mixing GDC with the Ag-Pd to form a composite significantly improves performance due to decreased non-ohmic resistance (Fig. 4.5b). Ohmic resistance increases with higher GDC content since GDC has much lower conductivity compared to the purely metallic conduction of Ag-Pd. However, this ohmic resistance increase is more than compensated for by the decrease in non-ohmic resistance. The composite $(Ag\text{-}Pd)_x\text{-}GDC_{1-x}$ has a large contact area (triple phase boundary length) between the ionic conducting GDC and electronic conducting Ag-Pd, so that there is more area for the electrochemical reactions to take place, decreasing the non-ohmic resistance. The increase in TPB length is the same reason for performance improvement as with LSM-YSZ composite compared to pure LSM.

The $(Ag\text{-}Pd)_{0.82}\text{-}GDC_{0.18}$ composition has the best overall performance (0.625 $\Omega\cdot cm^2$ non-ohmic resistance) and is stable for the testing time of 100 h at 750 °C and 0.8 V. After 100 h, non-ohmic resistance degrades at 0.08 $\Omega\cdot cm^2$/1000 h, a factor of 10 lower than reported for $Ag\text{-}Er_{0.4}Bi_{1.6}O_3$-YSZ composite electrodes (0.8 $\Omega\cdot cm^2$/1000 h) [56]. The $Ag\text{-}Er_{0.4}Bi_{1.6}O_3$-YSZ was tested at lower temperature (650 °C) and lower voltage (0.25 V), both of which would tend to make degradation less severe, but also had much lower initial resistance (0.065 $\Omega\cdot cm^2$) due to small particle size. Hence, the $(Ag\text{-}Pd)_{0.82}\text{-}GDC_{0.18}$ particle size and structure still need significant optimization to increase performance while maintaining good electrical stability.

4.4.2. Chemical and morphological evaluation of electrochemically tested cells

In cells tested with Ag-Pd electrodes, some electrodes densified while other remained porous (Fig. 4.6a,b). These observations support the hypothesis that the cell to cell variation in non-ohmic resistance is largely due to microstructural variation. The positive correlation between anode densification and non-ohmic degradation is likely due to a reduction in the TPB length. In dense electrodes, oxygen is unable to diffuse to or from the Ag-Pd-YSZ interface (except to a limited extent through the Ag-Pd bulk), limiting the current flow.

Using an $(Ag\text{-}Pd)_x\text{-}GDC_{1-x}$ composite reduces Ag-Pd particle agglomeration during sintering (Fig. 4.2b,c). Since testing the composite at OCV does not result in significant further agglomeration (Fig. 4.6d), it is apparent that exposure to 750 °C alone does not have a great effect on the Ag-Pd structure. This is to be expected since the sintering temperature is 100 °C higher. However, testing the composite at 0.8 V still results in Ag-Pd densification and agglomeration as in the single phase material (Fig. 4.6c). Therefore the primary driver of silver migration is the applied voltage. Silver is known to be very susceptible to migration under an electric field (electromigration) [76]. The observed silver migration does not appear to negatively affect performance, which improves and stabilizes within the 100 h testing time.

There are five primary sets of observations on YSZ surface morphological changes that will be discussed: 1. YSZ ridge formation (Fig. 4.8d); 2. grain boundary porosity (Fig. 4.9b); 3. surface undulations that may be accompanied by impurities (Figs. 4.9a, 4.9b, 4.9d, 4.13b, 4.13c); 4. copper-palladium deposits (Fig. 4.9e); and 5. the effect of applied voltage on impurities and surface undulations.

The ridge formation at the silver-YSZ interface (Fig. 4.8d) is attributed to surface diffusion of Zr^{4+} cations, as has similarly been observed with LSM electrodes on YSZ [22]. Due to the high contact angle of Ag-Pd on the YSZ substrate, the cations diffuse towards the Ag-Pd grains in order to decrease the free surface energy by reducing the curvature at the edges of the grains, forming the observed imprint.

The grain boundary porosity in the anode-side YSZ electrolyte (Fig. 4.9b) is explainable through the buildup of oxygen gas at the anode-electrolyte interface. Since oxygen ions are released from the YSZ lattice and oxidized to oxygen gas, the gas can reach high pressures inside closed pores at the interface [30]. The upper bound for interfacial pressure at 0.8 V is approximately 10^8 atm at 750 °C, calculated using equations by Virkar et al. [29]. However, such a high pressure will not be achieved due to the limitations from the mechanical strength of the Ag-Pd anode. The tensile strength of silver at 750 °C is approximately 100 atm [77], which provides a rough estimation of the upper limit of interfacial oxygen pressure. At the cathode-side interface, there is no observed grain boundary porosity (Fig. 4.9a), as oxygen gas is being consumed rather than produced. The nucleation of high-pressure oxygen gas in the electrolyte near the anode-electrolyte interface is responsible for some the observed morphological damage in the YSZ.

If the undulated structures were solely due to oxygen pressure buildup, they would be expected to be present throughout the entire anode-electrolyte interface, as was previously observed using LSM electrodes. Therefore, there must be another mechanism that accounts for the highly localized nature of these structures.

The evidence presented suggests that the undulated structures on YSZ are related to certain interfacial impurity species such as silicon oxide. No silicon oxide impurities are

detected on the unaltered YSZ surfaces (Fig. 4.8), but silicon oxide was detected on several undulated regions (Figs. 4.9c, 4.10). The random and localized nature of the undulated regions is characteristic of contaminants introduced from the lab or in the form of glass frits, which are commonly added to metal pastes [78]. The use of high-purity materials without these impurities is expected to prevent the YSZ morphological damage and will be the subject of future study.

When adding a 1 μm thick silicon oxide layer between the electrolyte and electrodes, the morphological changes became much more widespread (Figs. 4.13b,c), which further supports the role of silicon oxide in forming the undulations. The silicon oxide layer only covers about half of the active surface after testing, which may be a result of migration during testing or removal during electrode dissolution. This removal of silicon oxide explains why impurities are not detected in some undulated regions of cells (Figs. 4.9a,b).

Cu-Pd is observed on the YSZ surface after testing at 0.3 V or higher and subsequently dissolving the Ag-Pd (Fig. 4.9e). Sources of copper are the paste, mesh, or wire (Table 4.1). The Cu-Pd deposits are left behind due to the low solubility of the intermetallic in nitric acid relative to the single metal components [79]. The possibility that the Pd in the deposits had remained dissolved in the electrode alloy after testing can be ruled out because Ag-Pd alloy is soluble in nitric acid [80]. Since the deposits are only observed after testing under voltage and only on the anode side, their presence is attributed to voltage-induced migration. Since silver is more susceptible to electromigration than palladium [76], and because electromigration acts in the same direction as electron flow [81], there is expected to be a tendency for silver in the anode to flow away from the anode-electrolyte interface, causing a net migration of copper and palladium toward the interface as observed.

Before testing, impurities (e.g. oxides of Si and Ca) are found in the electrode bulk (Fig. 4.11a), while after testing at 0.8 V, the anode impurities are found primarily at the anode-electrolyte interface (Fig. 4.11b). The interfacial impurities are accompanied by YSZ morphological damage (Figs. 4.9c, 4.10, 4.12b). As with Cu and Pd, the difference in electromigration rates of various species is one mechanism for the transport of these impurities to the YSZ surface. The higher voltage required to transport the $(Ca,Si)O_x$-type impurities can be attributed to their much larger size (5-10 μm, Fig. 4.9c) relative to the Cu-Pd impurities (1 μm, Fig. 4.9e). It is also known that impurities readily migrate to the surfaces of nickel at elevated temperature to reduce the impurity-to-nickel interfacial energy [41]; this effect may be even more pronounced with silver due to its lower melting temperature (962 °C) compared to nickel (1455 °C).

4.4.3. Mechanism for YSZ surface rearrangement

Severe YSZ surface rearrangement in the form of undulations takes place in the presence of oxide impurities such as $(Ca,Si)O_x$. Although such morphological changes may be expected to relate to chemical interactions between the YSZ and the silver or impurities, EDS and XRD results show no evidence for substantial dissolution of silicon or silver in the YSZ lattice, in accordance with other findings in the literature [82,83]. There are also not expected to be any phase changes in the silver such as oxidation or melting according to the Ag-O phase diagram (Fig. 4.14) [84], even considering the possibility of elevated oxygen partial pressures at the anode-electrolyte interface up to 100 atm.

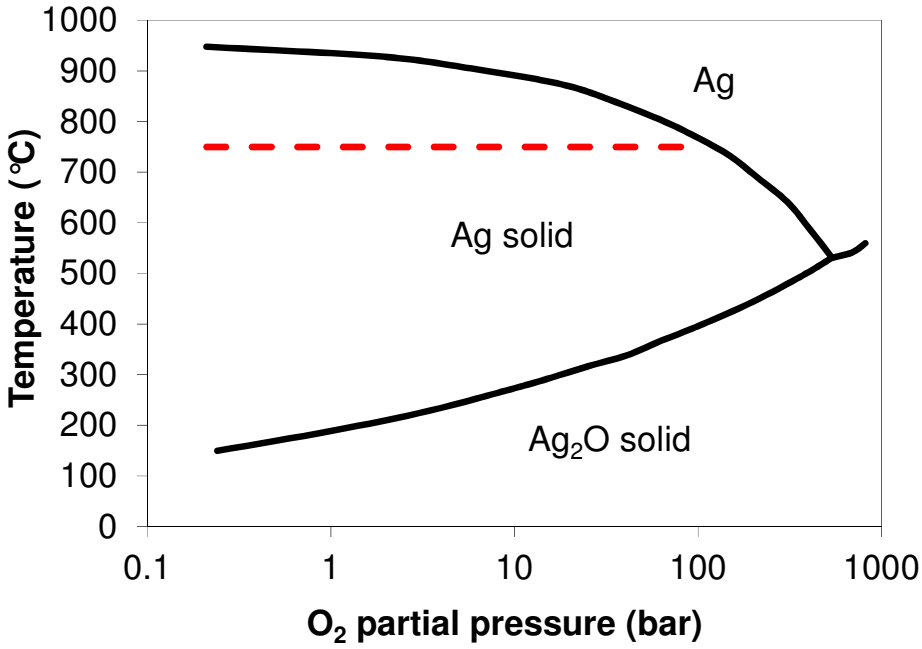

Fig. 4.14. Ag-O phase diagram based on oxygen partial pressure and temperature. The dotted line indicates the operating temperature and range of possible oxygen pressures at the anode-electrolyte interface; these conditions remain inside the solid silver region.

According to Jensen et al. [41] the formation of YSZ surface undulations is thermodynamically favorable when there is an accompanying reduction in surface free energy. The presence of other species (i.e. impurities) alters the surface energy characteristics of the interface, exposing lower energy facets on the YSZ surface. The faceting presumably also takes place via surface diffusion of cations.

A summary of impurity diffusion and anode-electrolyte interfacial processes is shown in Fig. 4.15. The application of current causes a counterflow electromigration of Cu-Pd from the anode bulk to the anode-electrolyte interface. Combined effects of electromigration and interfacial energy minimization drive the movement of Si-based impurities to the same interface. YSZ surface undulations form only in the vicinity of Si-based impurities due to

changes in YSZ surface energy characteristics. These findings show that silver-based electrodes and YSZ surfaces in contact with the electrodes may not be structurally stable under the combined effects of impurities and voltage application.

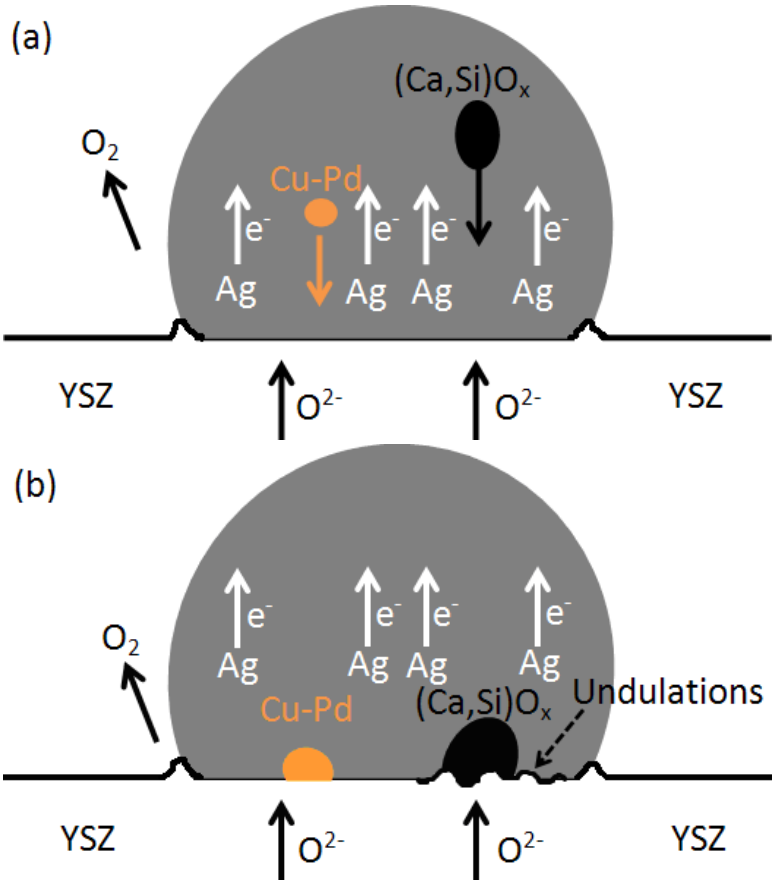

Fig. 4.15. Schematic showing anode-electrolyte interfacial processes during current flow. a) At the initiation of current flow, silver in the electrodes undergoes electromigration, causing a net migration of Cu-Pd in the opposite direction. Oxide impurities also migrate towards the silver-YSZ interface to reduce interfacial energy among the silver, YSZ, and impurities. b) With continued current flow, the Cu-Pd and oxide impurities remain at the silver-YSZ interface, and YSZ surface undulations form in the vicinity of the oxide impurities.

4.5. Summary

Symmetric cells of the configuration Ag-Pd/$(Ag\text{-}Pd)_x$-GDC_{1-x}/YSZ/$(Ag\text{-}Pd)_x$-GDC_{1-x}/Ag-Pd have been used to investigate the stability of silver-based electrodes at 750 °C under applied voltage bias. $(Ag\text{-}Pd)_x$-GDC_{1-x} composite electrodes have much higher performance and stability compared to single-phase Ag-Pd electrodes due to the mixed conducting characteristics of the composites. Despite silver's non-reactivity, surface porosity and undulations, as well as trace impurities, were observed on the contacting YSZ surfaces using electron microscopy and energy dispersive X-ray spectroscopy. Voltage bias as low as 0.3 V drives the counterflow electromigration of Cu-Pd from the anode to the anode-electrolyte interface. The combined effects of applied voltage bias and interfacial energy minimization drive the diffusion of Si-based impurities from both electrodes to the silver-YSZ interfaces; this effect is seen only at high voltage (0.8 V). The impurities affect the YSZ surface energy characteristics, leading to YSZ surface diffusion and undulation formation.

CHAPTER 5: CATHODE DEGRADATION DURING ELECTROLYSIS OF WATER AND CARBON DIOXIDE

5.1. Objectives

Solid oxide electrolysis cells show great promise for syngas production through the co-electrolysis of water and carbon dioxide. However, there is very limited published literature on the degradation of Ni-based SOEC fuel electrodes, particularly in atmospheres containing CO/CO_2. The objective of this work is to develop a further understanding of how the Ni-YSZ fuel electrode degrades during CO_2 electrolysis in SOEC, and how it differs from degradation during H_2O electrolysis. Ni-YSZ degradation has been characterized in terms of cell electrochemical performance, morphological changes, and compositional changes in the electrode.

5.2. Experimental

Cells and test fixtures were fabricated as described in section 2.1. Cells had the configuration Ag-Pd/Ni-YSZ/YSZ/LSM-YSZ/Ag-Pd. Alumina-based cement (Aremco, Ceramabond 552) was used to seal each cell against a 25 mm diameter alumina tube, with the Ni-YSZ electrode facing to the inside. An operating temperature of 840 °C was used. Air was delivered to the LSM-YSZ electrode at 300 cm^3/min. The fuel-side gas mixture consisted of either $H_2/H_2O/N_2$ (9.4 standard cm^3/min (sccm) H_2, 3–30 vol% H_2O, 50 sccm N_2) or CO/CO_2 (10–50 sccm of CO, 90–117 sccm of CO_2, with CO ranging from 10–30 vol%). The fuel-side

gas composition was allowed to reach steady state by monitoring cell open circuit voltage (OCV) and waiting for the rate of change in OCV to decrease below 1 mV/min, which typically took less than 2 h. During this time, the NiO in the fuel electrode was reduced to Ni. The initial performance of the cell was electrochemically characterized using chronoamperometry to create a current-voltage characteristic, as well as electrochemical impedance spectroscopy (EIS) to deconvolute ohmic and non-ohmic contributions to cell resistance. The cell was run in electrolysis operation for 100 h, and EIS was recorded every 4 h. Cells were tested in a wide voltage range (0, 0.3, 0.5, and 0.8 V above OCV) to observe degradation effects under both standard and accelerated conditions. Experiments were repeated several times at each condition.

A symmetric cell of the configuration LSM-YSZ/YSZ/LSM-YSZ was fabricated and tested in air at 840 °C and 0.8 V. The symmetric cell's LSM-YSZ anode was under the same conditions and atmosphere as the anode of the SOEC. The performance difference between the symmetric cell and an SOEC could thus be attributed to performance differences between the LSM-YSZ cathode in air and the Ni-YSZ cathode in $H_2/H_2O/N_2$.

Energy-dispersive X-ray spectroscopy (EDS) was used for semi-quantitative analysis of the Ni-YSZ electrode composition after each test. For each cell, several EDS measurements were taken of the electrode top surface and cross section, and the average mass ratio of nickel to zirconia was recorded. The Ni/Zr mass ratio was also measured for untested electrodes. Since zirconia content is expected to remain stable under the present testing conditions, the Ni/Zr ratio provided a normalized value for measuring the nickel content in the electrodes.

5.3. Results and Discussion

5.3.1. Electrochemical performance and degradation

The performance stability of a symmetric cell with LSM-YSZ electrodes was compared with performance of the SOEC with a Ni-YSZ cathode and LSM-YSZ anode (Fig. 5.1). Ohmic and non-ohmic contributions were determined from the high and low-frequency intercepts on EIS Nyquist plots. Ohmic contributions are mostly attributed to the ionic resistance of the electrolyte support, while non-ohmic contributions include the electrochemical reactions at the electrodes, as well as gas phase transport [63]. The initial ohmic resistances of the two cells are similar because both cells use nominally identical YSZ electrolyte supports. The initial non-ohmic resistance of the SOEC is higher than that of the symmetric cell. This difference is attributed to increased resistance of the H_2O reduction reaction at the Ni-YSZ cathode relative to the oxygen reduction reaction at the LSM-YSZ cathode. Performance of the symmetric cell is stable over the testing time of about 80 h. However, both the ohmic and non-ohmic resistances of the SOEC increase with time. The stability of the symmetric cell shows that the degradation of the SOEC can be attributed primarily to the Ni-YSZ electrode.

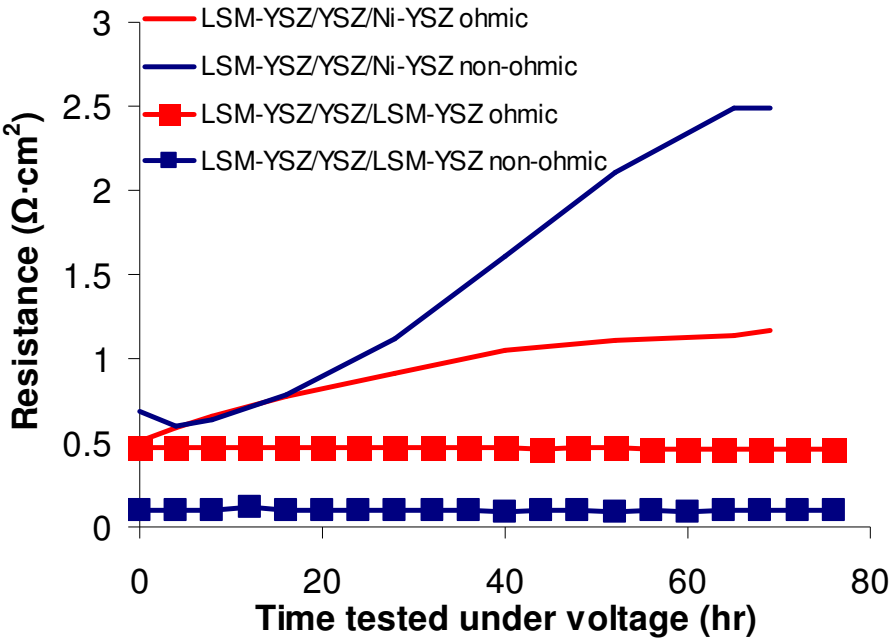

Fig. 5.1. Ohmic and non-ohmic resistance degradation with time for an electrolysis cell (air/LSM-YSZ/YSZ/Ni-YSZ/11 vol% H_2, 30 vol% H_2O, balance N_2) and a symmetric cell (air/LSM-YSZ/YSZ/LSM-YSZ/air) with 0.8 V applied.

In order to optimize Ni-YSZ electrode composition and structure, various compositions (50 wt% NiO, 50 wt% YSZ and 66 wt% NiO, 34 wt% YSZ), sintering temperatures (1350–1400 °C), and sintering times (1–2 h) were used on different cells. Cells were tested at 840 °C with a fuel side atmosphere of 11 vol% H_2, 30 vol% H_2O, balance N_2, and an applied voltage of 0.8 V. Cell electrical performance and stability varied widely with Ni-YSZ preparation technique, and the best performing composition was 66 wt% NiO, 34 wt% YSZ, sintered at 1400 °C for 2 h (Fig. 5.2). Therefore, this preparation technique was used for the remainder of the tests.

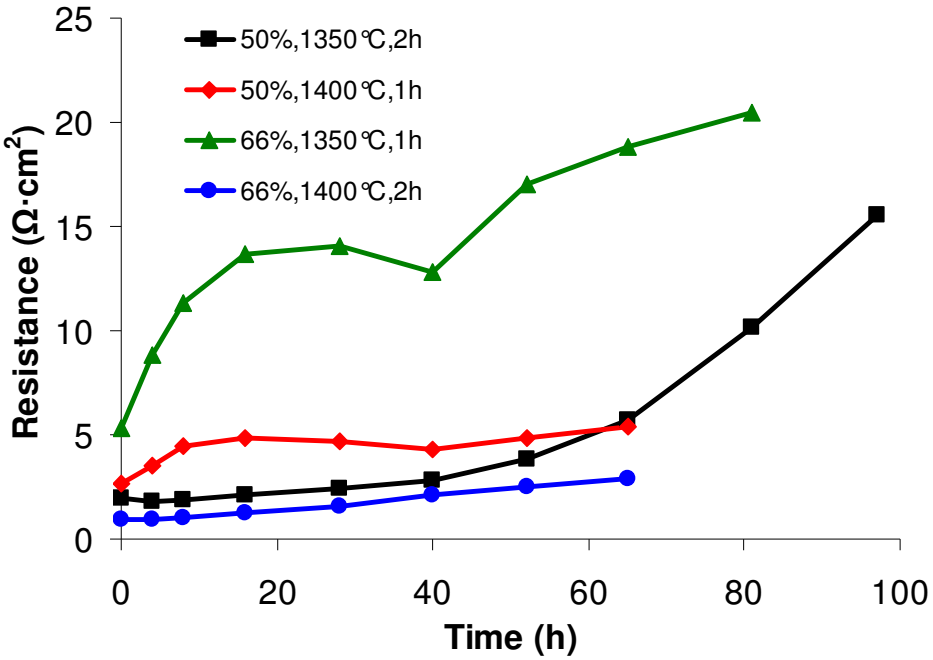

Fig. 5.2. Total resistance over time for cells tested at 840 °C and 0.8 V, and Ni-YSZ electrodes prepared with various NiO weight percents, sintering temperatures and times.

The 50 wt% NiO composition is equivalent to 35 vol% Ni on a solids basis; this content is too low to provide a well-interconnected Ni particle network in the electrode [85]. The poor performance for the 50 wt% NiO compositions is attributable to insufficient Ni particle interconnectivity, resulting in low conductivity. Sintering the 66 wt% NiO composition at 1350 °C for 1 h also resulted in relatively poor performance, and can be attributed to poor Ni particle interconnectivity due to insufficient sintering temperature and time.

SOEC performance was characterized using a variety of fuel-side atmospheres using chronoamperometry to create a current density-voltage characteristic (Fig. 5.3). Performance was higher during SOFC operation than during SOEC operation, higher in H_2/H_2O

atmosphere than in CO/CO_2 atmosphere, and higher with low CO_2 content. These observations agree qualitatively with results found in literature [13].

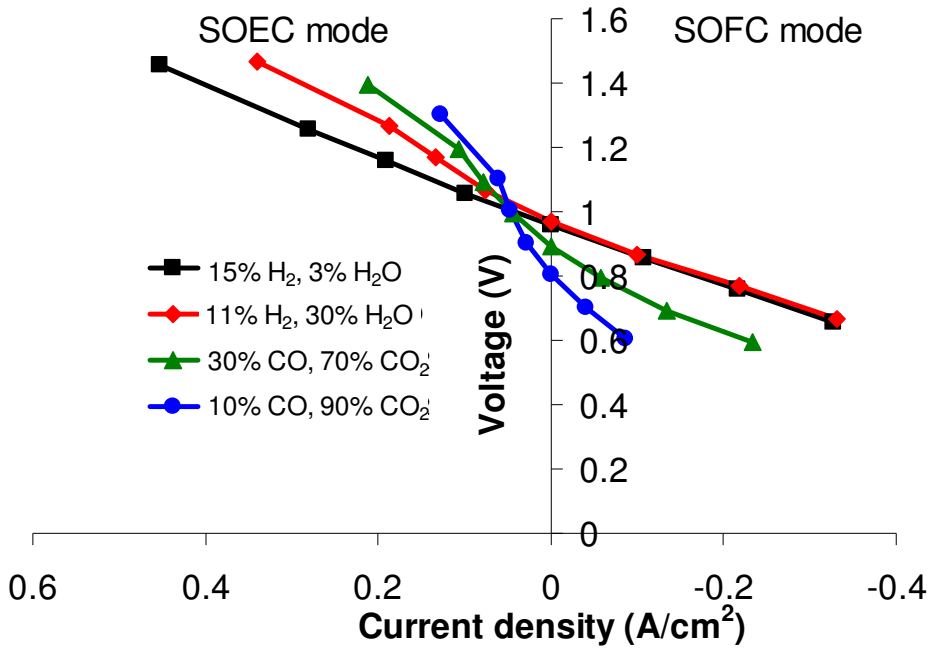

Fig. 5.3. Current density-voltage characteristics of SOECs under various fuel-side atmospheres prior to long-term voltage application.

SOECs were tested under a variety of fuel-side gas compositions and applied voltages. Ohmic degradation was accelerated at higher applied voltages and higher H_2O content (Fig. 5.4a). Under 0.5 V applied, ohmic degradation rates were similar between H_2/H_2O and CO/CO_2 atmospheres. Non-ohmic degradation was also accelerated in higher H_2O content, and was more severe in CO/CO_2 than in H_2/H_2O (Fig. 5.4b). However, there is no clear correlation between non-ohmic degradation rate and applied voltage. The cell tested at 750 °C experienced less ohmic and non-ohmic degradation than similarly tested cells at 840 °C.

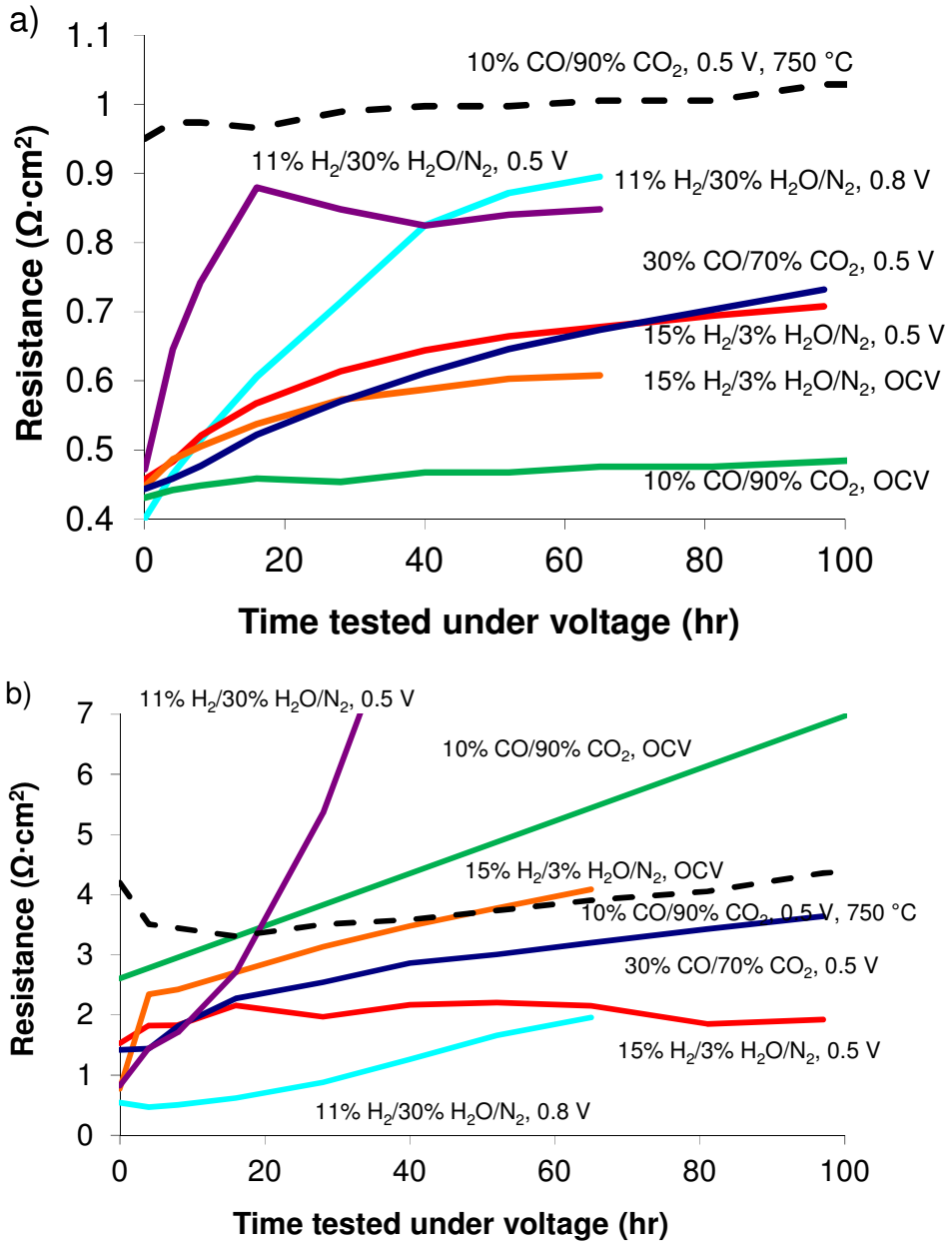

Fig. 5.4. Resistance degradation with time for SOECs tested at 840 °C under various atmospheric and applied voltage conditions; dotted line is cell tested at 750 °C; a) ohmic; b) non-ohmic.

5.3.2. Morphological observations

Sintered Ni-YSZ electrodes were imaged using scanning electron microscopy before (as NiO-YSZ) and after NiO reduction and electrochemical testing. After sintering, the NiO and YSZ particles are well connected and have a smooth surface morphology, although some particle agglomerations reach up to 3–4 μm in diameter (Fig. 5.5a). NiO was reduced to Ni metal by introducing an atmosphere of 15% H_2, 3% H_2O, and balance N_2 (Fig. 5.5b). After the reduction, the YSZ particles remain under 1 μm diameter, but Ni particles take the form of agglomerates 3–4 μm in diameter with surface roughness. Electrode porosity has increased significantly, and gaps are visible between the Ni and YSZ particles. These effects are due to the lattice volume shrinkage that accompanies the reduction of NiO to Ni [86].

Slightly increased Ni agglomeration was observed after exposure to 840 °C under various conditions, including 15% H_2, 3% H_2O, and balance N_2 at OCV for 67 h (Fig. 5.5c), 15% H_2, 3% H_2O, and balance N_2 at 0.5 V for 170 h (Fig. 5.5d), 11% H_2, 30% H_2O, and balance N_2 at 0.8 V for 69 h (Fig. 5.5e), and 30% CO and 70% CO_2 at 0.5 V for 97 h (Fig. 5.5f).

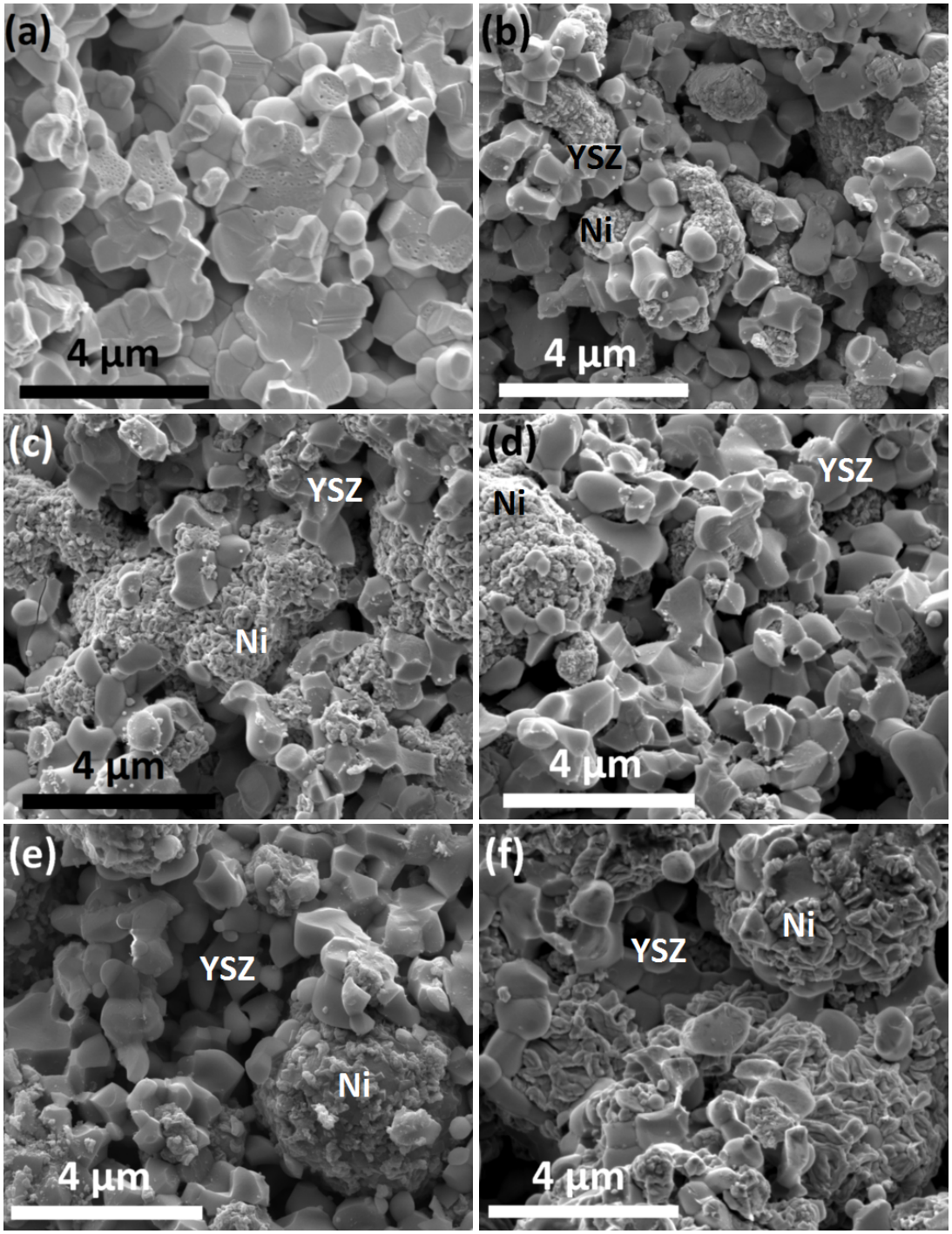

Fig. 5.5. Scanning electron micrographs showing cross-sectional microstructure of the Ni-YSZ electrodes; a) NiO-YSZ as-sintered; b) Ni-YSZ after NiO reduction; c) tested in 15% H_2, 3% H_2O at OCV; d) tested in 15% H_2, 3% H_2O at 0.5 V; e) tested in 11% H_2, 30% H_2O at 0.8 V; f) tested in 30% CO, 70% CO_2 at 0.5 V.

Table 5.1 shows the average nickel particle diameters after testing under different temperatures, fuel-side gas compositions and voltages. Particle diameters were estimated from several SEM pictures at each condition. The particles are as large as 12 μm in diameter, with the sizes of the larger (>1 μm) particles averaging 3–4 μm. These particle sizes are unusually large compared with the typical Ni-YSZ electrode particle size around 1 μm or less [87]. Average particle size is about 3.1 μm before testing, and increases to 3.5–4.0 μm after testing at 840°C. However, particle size does not increase after testing at 750 °C. No correlations are found between particle size and gas composition, applied voltage, or testing time due to large scatter in the data.

Table 5.1. Average nickel particle diameters in Ni-YSZ electrodes of cell tested under a variety of temperatures, fuel-side gas compositions and voltages.

Temperature (°C)	Fuel gas composition	Applied voltage (V)	Time under voltage (h)	Average Ni particle size (μm)
840	15% H_2/3% H_2O/N_2	0	0	3.1 ± 0.3
840	15% H_2/3% H_2O/N_2	0	67	3.9 ± 0.4
840	15% H_2/3% H_2O/N_2	0.5	170	3.9 ± 1.1
840	11% H_2/30% H_2O/N_2	0.5	69	4.0 ± 0.7
840	11% H_2/30% H_2O/N_2	0.8	69	3.6 ± 0.3
840	10% CO/90% CO_2	0	115	3.5 ± 0.7
840	30% CO/70% CO_2	0.5	97	4.0 ± 0.4
750	10% CO/90% CO_2	0.5	117	2.7 ± 0.3

5.3.3. Possible explanations for degradation

Nickel is known to evaporate in the form of $Ni(OH)_2$ in an atmosphere containing H_2O [33-36]. During nickel oxide reduction, nickel evaporation may be attributed to Eq. (5.1) or Eq. (5.2):

$$NiO(s) + H_2O(g) \leftrightarrow Ni(OH)_2(g) \quad (5.1)$$

$$2NiO(s) + H_2(g) \leftrightarrow Ni(s) + Ni(OH)_2(g) \quad (5.2)$$

It was calculated that a significant amount of nickel (equivalent to a 1 µm thick layer) could evaporate during one hour of nickel oxide reduction if the partial pressure of $Ni(OH)_2$ were 5×10^{-5} atm. If $Ni(OH)_2$ were formed via Eq. (5.2), it was calculated this partial pressure would be possible if the activity of solid nickel were 0.004 [84]. This low nickel activity may be possible in the early stages of nickel oxide reduction when there is very low nickel content in the electrode. Thus it is plausible that nickel evaporation occurred during the initial nickel oxide reduction at 840 °C.

EDS measurements were taken from the exposed surface of the Ni-YSZ electrode, providing a representation of the Ni/YSZ content to a depth of approximately 1 µm. In all tested electrodes, it was found that the surface Ni/Zr mass ratio decreased compared to the untested electrodes. The percent change in Ni/Zr mass ratio shows a negative correlation with testing time at 840 °C as shown in Fig. 5.6. Immediately after NiO reduction (0 h testing time), the Ni/Zr mass ratio decreased by 11%, while in cells tested for 4–200 h, the mass ratio was 8–35% below that of the untested NiO-YSZ. There is much scatter in the data due to the different conditions experienced by each cell, as well as the semi-quantitative nature of the EDS measurements. The observed trend suggests that surface nickel content is decreasing

with time exposed to 840 °C. For the cell tested at 750 °C, the percent change in Ni/Zr mass ratio is less severe than in cells tested at 840 °C for the same time. Therefore, elevated testing temperatures as well as increased exposure time both tend to diminish surface nickel content by a greater degree.

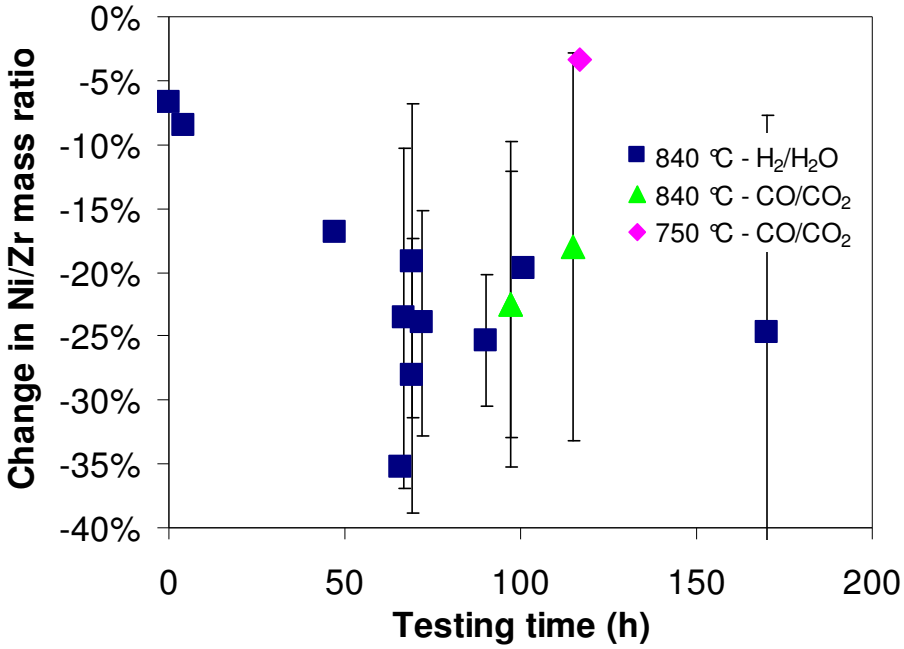

Fig. 5.6. Percent change in Ni/Zr mass ratio as detected by EDS of the Ni-YSZ electrode top surface as a function of testing time and temperature.

EDS measurements were also taken from the cross section, encompassing the entire depth of the electrode, providing a representation of the average Ni/YSZ mass ratio in the electrode. However, no correlation was observed between the change in Ni/Zr mass ratio and testing time, and data scatter was significant (Fig. 5.7). There were also no correlations found

between Ni/Zr mass ratio change and other factors such as fuel-side gas composition, applied voltage, or degradation rate.

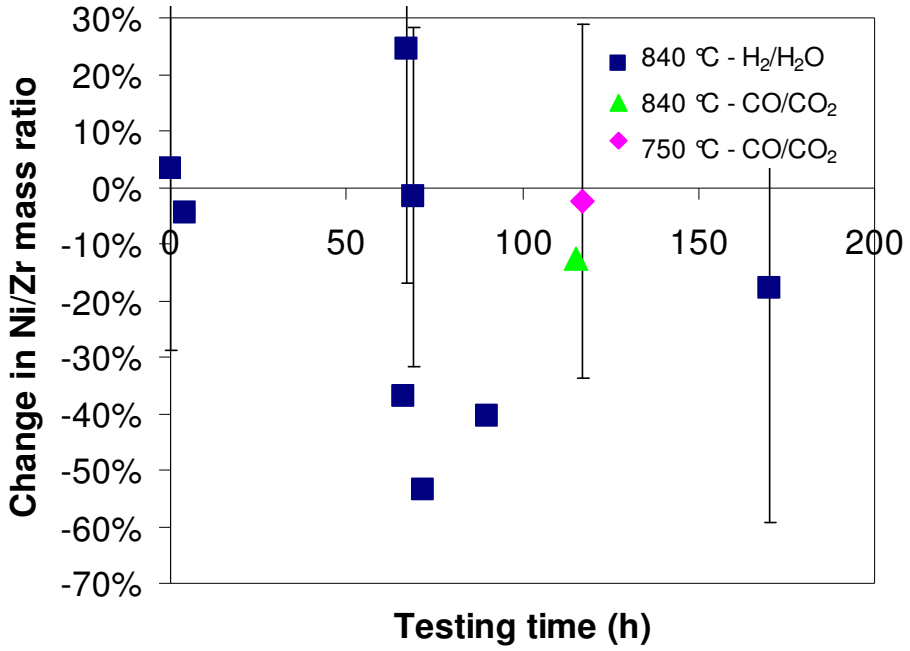

Fig. 5.7. Percent change in Ni/Zr mass ratio as detected by EDS of the Ni-YSZ electrode cross-section as a function of testing time and temperature.

The decrease in surface nickel content may be a factor in the rapid electrical degradation observed under nearly all testing conditions. With less nickel present near the surface, the electrical connectivity of the nickel structure would be lowered, leaving only the YSZ structure interconnected. Since YSZ has significantly lower conductivity than nickel, the effect would be a decrease in performance. Another effect of the decreased surface nickel content was to lessen the contact area between the Ag-Pd current collection paste and nickel in favor of contact between Ag-Pd and YSZ. While silver contacts well with nickel in a low-

oxygen environment [88], metal to oxide contact is known to be poor in such environments [89]. The resulting poor contact between Ag-Pd and YSZ could significantly decrease the area for electrical contact and cause significant performance degradation. Ag-Pd makes better contact with the LSM-YSZ air electrode, as metal to oxide contact is better in a high-oxygen environment due to oxygen dissolution into the metal [89].

Fig. 5.8 shows a post-test cell after the silver screen current collectors and wires have been removed. Ag-Pd paste remained mostly adhered to the LSM-YSZ electrode (Fig. 5.8a), but separated with the screen from the Ni-YSZ electrode (Fig. 5.8b). These observations are consistent with the expected good contact between Ag-Pd and LSM-YSZ and poor contact between Ag-Pd and YSZ in the Ni-YSZ.

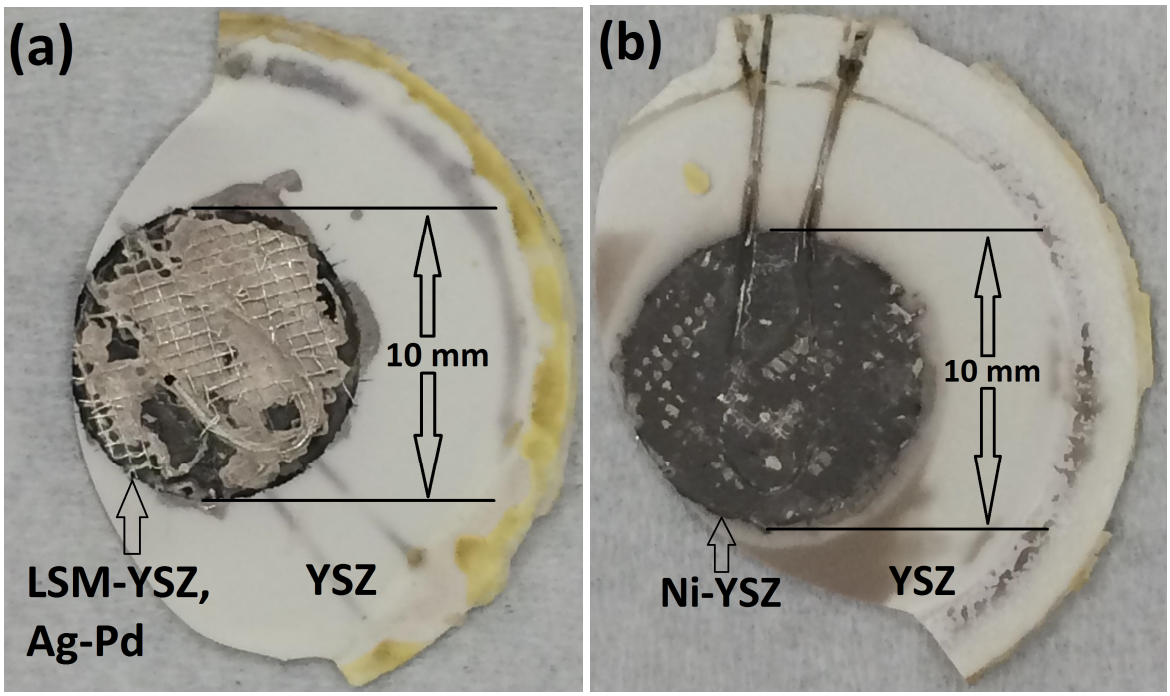

Fig. 5.8. Post-test cell tested in 15% H_2/3% H_2O/N_2 at 0.5 V for 47 h after removing silver screen current collectors and wires; a) LSM-YSZ side; b) Ni-YSZ side.

The decrease in nickel content near the Ni-YSZ electrode surface after testing may be due to either nickel evaporation or migration. During testing, the nickel is fully reduced, but there appears to be further nickel loss based on Fig. 5.6. Nickel metal can react with H_2O to form $Ni(OH)_2$ according to Eq. (5.3):

$$Ni(s) + 2H_2O(g) \leftrightarrow Ni(OH)_2(g) + H_2(g) \tag{5.3}$$

Nickel can also react with CO to form $Ni(CO)_4$ according to Eq. (5.4):

$$Ni(s) + 4CO(g) \leftrightarrow Ni(CO)_4(g) \tag{5.4}$$

Based on equilibrium thermodynamic data [84], the maximum partial pressures of $Ni(OH)_2$ and $Ni(CO)_4$ under the testing conditions was determined Based on the estimated mass of nickel in each electrode, it was calculated that a maximum of approximately 0.003% of the nickel can evaporate in the form of $Ni(OH)_2$ during 100 h of testing in an 11% H_2, 30% H_2O atmosphere. Only 10^{-8}% of the nickel can evaporate in the form of $Ni(CO)_4$ during each 100 h test in a 30% CO, 70% CO_2 atmosphere. These calculations suggest that nickel cannot undergo significant evaporation during testing.

Surface nickel content may also be diminished through nickel migration. The nickel movement is not primarily a result of electromigration, as the decrease in surface nickel content was also observed for cells tested at OCV. Instead the nickel movement is attributed to agglomeration as was observed in SEM (Table 5.1). Nickel agglomeration in the Ni-YSZ electrode is more severe with higher Ni content [85,90] due to increased initial contact among Ni particles. Therefore the observed agglomeration is attributed to the high (66 wt% of NiO, equivalent to 51 vol% Ni) Ni content, compared with the optimal composition of about 40 vol% Ni [85]. In addition to loss of contact with the current collector, Ni agglomeration will reduce electrode conductivity [90], further impacting performance.

There is no evidence of carbon deposition in the CO/CO_2 tested cell (Fig. 5.5f) which would be visible as reduced porosity in the nickel particles [37]. This observation agrees with expectations from thermodynamic calculations for equilibrium of the Boudouard reaction (Fig. 5.7). The region of carbon deposition corresponds to a carbon activity of greater than unity [91]. The current operating temperatures and CO/CO_2 ratios lie well outside the region with potential for carbon formation. During electrolysis, the CO/CO_2 ratio will increase in the vicinity of the electrode. However, this effect will be minimal due to CO_2 utilization below 1.2% (calculated from 0.20 A maximum current, 117 sccm of CO_2), meaning that carbon deposition is not expected even during electrolysis.

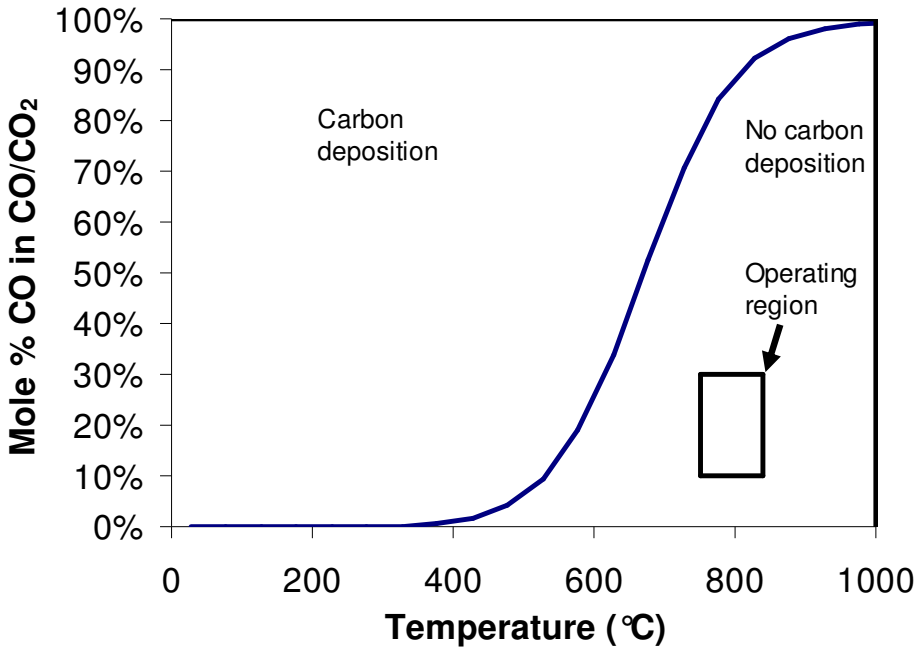

Fig. 5.9. Equilibrium diagram of the Boudouard reaction 2 CO(g) □ C(s) + CO_2(g). Carbon should not deposit under the operating conditions used for the cell tests [84].

Other possible sources of degradation are solid or gas phase impurities. Silica (SiO_2) is present in the sealing cement. Although silica has been found to poison Ni-YSZ electrodes [34], large particles of silica were detected by SEM/EDS in that study, accompanied by moderate degradation. No silica was detected in any of the cells tested in the current study, but degradation was still very severe. Therefore silica is not a primary reason for degradation.

Hydrogen sulfide (H_2S) is known to cause degradation in solid oxide cells with as low as 0.05 ppm content [92], but the resulting degradation is still less severe than the current observations. Additionally, all gases being used were ultra-high purity and are not expected to contain sulfur compounds in ppm-level quantities. Even if sulfur compounds were present, they should not significantly affect degradation when H_2 is present since H_2 would prevent significant sulfur deposition on the electrode [38]. So sulfur also cannot be a primary reason for degradation.

When the nickel is reduced, gaps appear between the nickel and the YSZ particles (most visibly in Fig. 5.5b). This is due to the volume reduction (approximately 40%) of the NiO when it is reduced to nickel. This may reduce the electrical contact among the nickel particles and between the nickel and YSZ particles. However, this shrinkage effect is completed after the initial NiO reduction and does not increase in severity during the test, as the degradation does. Additionally, there is no known literature about nickel shrinkage causing degradation, so this can also be eliminated as a possible degradation cause.

Silver-palladium is used as a current collector paste on both the fuel and air electrodes. If silver were evaporating more on the fuel electrode relative to the air electrode, electrical contact area would be reduced and degradation would result. Visual observations post-test show there may be less silver remaining on the fuel electrode than the air electrode. In some

inactive areas on the fuel electrode side, EDS shows small particles of silver which may be evidence of evaporation. However, the flow rate of gas on the fuel side (85 sccm) is lower than on the air side (300 sccm), which means more evaporation would be expected on the air side. It is known that reducing atmospheres (as on the fuel side) reduce the rate of silver evaporation compared to air exposure [93]. Therefore it seems unlikely that additional silver evaporation on the fuel electrode would be the cause for such fast degradation.

5.4. Summary

The following explanations have been ruled out as causes for rapid electrical degradation observed in SOECs tested in both H_2/H_2O and CO/CO_2 environments:

- LSM-YSZ degradation of any type
- Carbon deposition on Ni-YSZ electrode in CO/CO_2 atmosphere
- Nickel evaporation
- Silica or hydrogen sulfide impurity deposition on Ni-YSZ electrode
- Nickel particle shrinkage upon NiO reduction
- Silver evaporation from current collector on Ni-YSZ electrode

The degradation is attributed to NiO particle agglomeration after sintering, which continues as Ni particle agglomeration during testing at 840 °C. This effect decreases the Ni content at the surface of the electrode in contact with the Ag-Pd current collector, reducing contact area between the electrode and current collector, and reducing conductivity within the electrode. Performance degradation is less severe at 750 °C due to less severe Ni agglomeration and a less significant decrease in surface Ni content.

CHAPTER 6: CONCLUSIONS AND FUTURE WORK

Solid oxide cell performance degradation has been evaluated using electrochemical tests with a variety of materials, operating temperatures, atmospheres, and voltages. In order to simulate long-term (thousands of hours) testing in a shorter time period, voltages up to 0.8 V above OCV were applied for up to 200 h. Investigation of air electrode degradation was conducted using symmetric cells in order to simplify the test setup by eliminating seal requirements. The fuel electrode degradation study required the use of full cells with distinct fuel-side and air-side gas flows separated by a gas-tight seal.

The electrochemical performance of symmetric cells with LSM electrodes and YSZ electrolyte degraded severely in 100 h tests. Cell anodes consistently delaminated from the electrolytes, while cathodes remained well-adhered to the electrolytes. Post-test analysis revealed lanthanum zirconate ($La_2Zr_2O_7$) formation, YSZ porosity, and YSZ surface roughening at the anode-electrolyte interfaces, while cathode-electrolyte interfaces did not exhibit any detectable changes. The formation of small $La_2Zr_2O_7$ particles weakens the anode-electrolyte interface bonding. This weakening, together with the known oxygen pressure buildup at the anode-electrolyte interface, causes gradual separation of the LSM anode from the YSZ electrolyte. This separation decreases contact area, causing rapid performance degradation. The interfacial $La_2Zr_2O_7$ formation also negatively affects performance due to its poor electrical conductivity.

Additional studies could be performed on composite LSM-YSZ anodes fabricated by infiltration of LSM on a porous YSZ network, or by using a porous YSZ interlayer. A porous YSZ structure in contact with LSM anode may better allow the nucleating oxygen gas to

escape, suppressing oxygen pressure buildup, subsequent $La_2Zr_2O_7$ formation, and delamination at the anode-electrolyte interface.

Silver-based composites show promise as stable air electrodes in reduced-temperature solid oxide cells. The performance of symmetric cells with $(Ag\text{-}Pd)_{0.82}\text{-}GDC_{0.18}$ composite electrodes and YSZ electrolyte was stable for 100 h at 750 °C under an accelerated voltage of 0.8 V, and degraded at a rate of just 0.08 $\Omega \cdot cm^2$/1000 h in the time period from 100 to 160 h. However, the minimum non-ohmic resistance of 0.625 $\Omega \cdot cm^2$ is high compared to published results for similar silver-composite electrodes, meaning that additional particle size and structural optimization is required to improve performance while maintaining stability. Electromigration of silver under current application also remains a major barrier to morphological stability, particularly over long time scales. Further reducing the operation temperature would slow the electromigration effect and further improve stability, but electrode structure and composition would still need optimization in order to provide acceptable performance.

While silver is a mostly chemically inert material even at elevated temperatures, morphological damage was observed on YSZ surfaces after contact with Ag-Pd alloy electrodes at 750 °C under applied voltage. The YSZ surface became severely undulated, with a periodicity of about 200 nm. The damaged regions occurred in the vicinity of impurities such as SiO_x and $(Ca,Si)O_x$, while undamaged regions were free from these impurities. Impurities were observed to migrate towards the electrode-YSZ interface, particularly on the anode side. This migration is a combined effect of silver-impurity interface energy minimization and impurity counterflow due to silver's high susceptibility to electromigration. Once the impurities make contact with the YSZ, the YSZ surface

rearranges to expose facets with lower surface energy, giving the appearance of undulations. Future studies could investigate silver-based materials with higher purity in order to eliminate the interfacial morphological damage. Great care would need to be taken to avoid even the slightest contamination from external sources during cell preparation and testing, since impurity particles as small as one micron were observed to affect electrolyte surface structure.

Solid oxide electrolysis cells with LSM-YSZ air electrodes, YSZ electrolytes, and Ni-YSZ fuel electrodes were tested in both H_2/H_2O and CO/CO_2 fuel-side gas atmospheres at different temperatures and voltages. Performance and degradation worsened with higher H_2O content and higher CO_2 content, and was worse in CO/CO_2 than in H_2/H_2O. These observations are consistent with previous findings relating to fuel electrode surface kinetics. However, degradation of the Ni-YSZ electrode was unusually rapid in all testing conditions. The degradation was attributed to nickel particle agglomeration, causing a decrease in electrical connectivity and poor contact with the current collector.

Future studies could examine tested Ni-YSZ electrodes for low-level impurities such as sulfides, oxides, and carbonates which may be depositing near the triple phase boundary and negatively impacting performance. Mass spectrometry and gas chromatography would be used to analyze the outlet fuel gas composition for gas-phase impurities. Since the initial nickel particle size was unusually large compared to electrodes in published literature, electrodes with reduced initial particle size could be investigated. Smaller particle size would increase the triple phase boundary length and improve nickel electrical connectivity.

The current work furthers the understanding of high temperature materials interactions that lead to performance degradation in solid oxide electrolysis cells. Although

several mechanisms for LSM anode delamination have been proposed, this work provides the first observations on $La_2Zr_2O_7$ formation at the anode-electrolyte interface. While $La_2Zr_2O_7$ formation was previously known to be favorable at low O_2 partial pressure, this work provides a mechanism for formation at high O_2 pressure (above 1 atm). Silver-based electrodes are promising for use at temperatures below 750 °C, but electromigration and impurity-induced morphological damage both remain problems during operation under applied voltage. Ni-YSZ electrodes are not susceptible to carbon deposition, nickel coarsening or evaporation during H_2O and CO_2 electrolysis. However, the performance of Ni-YSZ electrodes is highly sensitive to their composition, sintering conditions, and morphology, including nickel particle connectivity.

APPENDIX A: PEER-REVIEWED PUBLICATIONS AND PROCEEDINGS

Michael Keane, Prabhakar Singh. Effects of Impurities on Silver-$(ZrO_2)_{0.92}(Y_2O_3)_{0.08}$ Interface Morphology in Solid Oxide Cells. *Ceramics International* 40 (2014) 7261–7268.

Boxun Hu, **Michael Keane**, Manoj K. Mahapatra, Prabhakar Singh. Stability of strontium-doped lanthanum manganite cathode in humidified air. *Journal of Power Sources* 248 (2014) 196–204.

Na Li, **Michael Keane**, Manoj K. Mahapatra, Prabhakar Singh. Mitigation of the delamination of LSM anode in solid oxide electrolysis cells using manganese-modified YSZ. *International Journal of Hydrogen Energy* 38 (2013) 6298–6303.

Michael Keane, Manoj K. Mahapatra, Atul Verma, Prabhakar Singh. LSM-YSZ interactions and anode delamination in solid oxide electrolysis cells. *International Journal of Hydrogen Energy* 37 (2012) 16776–16785.

Michael Keane, Prabhakar Singh. Silver-Palladium Alloy Electrodes for Low Temperature Solid Oxide Electrolysis Cells (SOEC). *Proceedings of the 36th International Conference on Advanced Ceramics and Composites*. Sanjay Mathur, 2012.

Michael Keane, Atul Verma, Prabhakar Singh. Observations on the Air Electrode-Electrolyte Interface Degradation in Solid Oxide Electrolysis Cells. *Proceedings of the 35th International Conference on Advanced Ceramics and Composites*. Sanjay Mathur, 2011.

APPENDIX B: COPYRIGHT PERMISSIONS

Chapter 3 of this dissertation was modified from the following published article: M. Keane, M.K. Mahapatra, A. Verma, P. Singh. LSM-YSZ interactions and anode delamination in solid oxide electrolysis cells. Int J Hydrogen Energ 2012;37:16776–85. Copyright permission was received from the International Journal of Hydrogen Energy for use of the full article in the author's dissertation.

Chapter 4 of this dissertation was modified from the following published article: M. Keane, P. Singh. Effects of Impurities on Silver-$(ZrO_2)_{0.92}(Y_2O_3)_{0.08}$ Interface Morphology in Solid Oxide Cells. Ceram Int 2014;40:7261–8. Copyright permission was received from Elsevier for use of the full article in the author's dissertation.

REFERENCES

[1] K. Zhang, X.S. Li, Y. Duan, D.L. King, P. Singh, L. Li. Roles of double salt formation and $NaNO_3$ in Na_2CO_3-promoted MgO absorbent for intermediate temperature CO_2 removal. Int J Greenh Gas Con 2013;12:351–8.

[2] R. Elder, R.W.K. Allen. Nuclear heat for hydrogen production: Coupling a very high/high temperature reactor to a nuclear power plant. Prog Nucl Energ 2009;51:500–25.

[3] I. Ridjan, B.V. Mathiesen, D. Connolly, N. Duić. The feasibility of synthetic fuels in renewable energy systems. Energy 2013;57:76–84.

[4] R. Ramachandran, R.K. Menon. An Overview of Industrial Uses of Hydrogen. Int J Hydrogen Energ 1999;23(7):593–8.

[5] J.E. O'Brien, M.G. McKellar, E.A. Harvego, C.M. Stoots. High-temperature electrolysis for large-scale hydrogen and syngas production from nuclear energy – summary of system simulation and economics analyses. Int J Hydrogen Energ 2010;35:4808–19.

[6] S.C. Singhal, K. Kendall. High Temperature Solid Oxide Fuel Cells: Fundamentals, Design and Applications. Oxford: Elsevier Ltd, 2003.

[7] V. Liso, A.C. Olesen, M.P. Nielsen, S.K. Kær. Performance comparison between partial oxidation and methane steam reforming processes for solid oxide fuel cell (SOFC) micro combined heat and power (CHP) system. Energy 2011;36:4216–26

[8] C. Yang, A. Coffin, F. Chen. High temperature solid oxide electrolysis cell employing porous structured $(La_{0.75}Sr_{0.25})_{0.95}MnO_3$ with enhanced oxygen electrode performance. Int J Hydrogen Energ 2010;35;3221–6.

[9] J.R. Mawdsley, J.D. Carter, A.J. Kropf, B. Yildiz, V.A. Maroni. Post-test evaluation of oxygen electrodes from solid oxide electrolysis stacks. Int J Hydrogen Energ 2009;34:4198–207.

[10] J.W. Fergus. Lanthanum chromite-based materials for solid oxide fuel cell interconnects. Solid State Ionics 2004;171:1–15

[11] M.K. Mahapatra, K. Lu. Glass-based seals for solid oxide fuel and electrolyzer cells – A review. Mater Sci Eng R 2010;67:65–85.

[12] Z. Zhan, L. Zhao. Electrochemical reduction of CO_2 in solid oxide electrolysis cells. J Power Sources 2010;195:7250–4.

[13] P. Kim-Lohsoontorn, J. Bae. Electrochemical performance of solid oxide electrolysis cell electrodes under high-temperature coelectrolysis of steam and carbon dioxide. J Power Sources 2011;196:7161–8.

[14] J.E. O'Brien, C.M. Stoots, J.S. Herring, J.J. Hartvigsen. High-Temperature Co-Electrolysis of Steam and Carbon Dioxide for Direct Production of Syngas; Equilibrium Model and Single-Cell Tests. Fifth International Fuel Cell Science, Engineering, and Technology Conference, Brooklyn, NY (2007).

[15] J.E. O'Brien, C.M. Stoots, J.S. Herring, J.J. Hartvigsen. Performance of planar high-temperature electrolysis stacks for hydrogen production from nuclear energy. Nucl Technol 2007;158:118–31.

[16] EG&G Technical Services, Inc. Fuel Cell Handbook (Seventh Edition). Prepared for the U.S. Department of Energy, Office of Fossil Energy, Under Contract DE-AM26-99FT40575, National Energy Technology Laboratory, Morgantown, WV., November 2004.

[17] O.A. Marina, L.R. Pederson, M.C. Williams, G.W. Coffey, K.D. Meinhardt, C.D. Nguyen, E.C. Thomsen. Electrode Performance in Reversible Solid Oxide Fuel Cells. J Electrochem Soc 2007;154(5):B452–9.

[18] V.I. Sharma, B. Yildiz. Degradation Mechanism in $La_{0.8}Sr_{0.2}CoO_3$ as Contact Layer on the Solid Oxide Electrolysis Cell Anode. J Electrochem Soc 2010;157(3):B441–8.

[19] M. Backhaus-Ricoult. SOFC – A playground for solid state chemistry. Solid State Sci 2008;10:670–88.

[20] L. Ge, A. Verma, R. Goettler, D. Lovett, R.K.S. Raman, P. Singh. Oxide Scale Morphology and Chromium Evaporation Characteristics of Alloys for Balance of Plant Applications in Solid Oxide Fuel Cells. Metall Mater Trans A 2013;44A:S193–206.

[21] S.D. Ebbesen, C. Graves, A. Hauch, S.H. Jensen, M. Mogensen, Poisoning of Solid Oxide Electrolysis Cells by Impurities, J Electrochem Soc 2010;157(10):B1419–29.

[22] A. Mitterdorfer, L.J. Gauckler. $La_2Zr_2O_7$ formation and oxygen reduction kinetics of the $La_{0.85}Sr_{0.15}Mn_yO_3$, $O_2(g)$|YSZ system. Solid State Ionics 1998;111:185–218.

[23] A. Mai, V.A.C. Haanappel, S. Uhlenbruck, F. Tietz, D. Stöver. Ferrite-based perovskites as cathode materials for anode-supported solid oxide fuel cells. Solid State Ionics 2005;176:1341–50.

[24] A. Momma, T. Kato, Y. Kaga, S. Nagata. Polarization Behavior of High Temperature Solid Oxide Electrolysis Cells (SOEC). J Ceram Soc Jpn 1997;105(5):369–73.

[25] A. Kaiser, E. Monreal, A. Koch, D. Stolten. Reactions at the Interface $La_{0.5}Ca_{0.5}MnO_3$-YSZ/Al_2O_3 under Anodic Current. Ionics 1996;2:184–9.

[26] J. Guan, N. Minh, B. Ramamurthi, J. Ruud, J. Hong, R. Riley, D. Weng. High Performance Flexible Reversible Solid Oxide Fuel Cell. Final Technical Report, Performed under DOE Cooperative Agreement DE-FC36-04GO14351, GE Global Research Center, Torrance, CA., 2004-2006.

[27] H. Lim, A.V. Virkar. A study of solid oxide fuel cell stack failure by inducing abnormal behavior in a single cell test. J Power Sources 2008;185:790–800.

[28] R. Hino, K. Haga, H. Aita, K. Sekita. R&D on hydrogen production by high-temperature electrolysis of steam. Nucl Eng Des 2004;233:363–75.

[29] A.V. Virkar, J. Nachlas, A.V. Joshi, J. Diamond. Internal Precipitation of Molecular Oxygen and Electromechanical Failure of Zirconia Solid Electrolytes. J Am Ceram Soc 1990;73(11):3382–90.

[30] R. Knibbe, M.L. Traulsen, A. Hauch, S.D. Ebbesen, M. Mogensen. Solid Oxide Electrolysis Cells: Degradation at High Current Densities. J Electrochem Soc 2010;157(8):B1209–17.

[31] M.S. Sohal, J.E. O'Brien, C.M. Stoots, J.S. Herring, J.J. Hartvigsen, D. Larsen, S. Elangovan, J.D. Carter, V.I. Sharma, B. Yildiz. Critical Causes of Degradation in Integrated Laboratory Scale Cells During High-Temperature Electrolysis. INL/EXT-09-16004 Prepared for the U.S. Department of Energy, Office of Nuclear Energy, Under DOE Idaho Operations Office, Contract DE-AC07-05ID14517, Idaho National Laboratory, Idaho Falls, ID., May 2009.

[32] K. Chen, S.P. Jiang. Failure mechanism of (La,Sr)MnO_3 oxygen electrodes of solid oxide electrolysis cells. Int J Hydrogen Energ 2011;36:10541–9.

[33] A. Hauch, M. Mogensen, A. Hagen. Ni/YSZ electrode degradation studied by impedance spectroscopy — Effect of p(H2O). Solid State Ionics 2011;192:547–51.

[34] A. Hauch, S.D. Ebbesen, S.H. Jensen, M. Mogensen. Solid Oxide Electrolysis Cells: Microstructure and Degradation of the Ni/Yttria-Stabilized Zirconia Electrode. J Electrochem Soc 2008;155(11):B1184–93.

[35] L. Holzer, B. Iwanschitz, Th. Hocker, B. Münch, M. Prestat, D. Wiedenmann, U. Vogt, P. Holtappels, J. Sfeir, A. Mai, Th. Graule. Microstructure degradation of cermet anodes for solid oxide fuel cells: Quantification of nickel grain growth in dry and in humid atmospheres. J Power Sources 2011;196:1279–94.

[36] A. Hagen, R. Barfod, P.V. Hendriksen, Y.-L. Liu, S. Ramousse. Degradation of Anode Supported SOFCs as a Function of Temperature and Current Load. J Electrochem Soc 2006;153(6):A1165-71.

[37] V. Alzate-Restrepo, J.M. Hill. Carbon deposition on Ni/YSZ anodes exposed to CO/H_2 feeds. J Power Sources 2010;195:1344–51.

[38] S.D. Ebbesen, M. Mogensen. Electrolysis of carbon dioxide in Solid Oxide Electrolysis Cells. J Power Sources 2009;193:349–58.

[39] M. Keane, P. Singh. Silver-Palladium Alloy Electrodes for Low Temperature Solid Oxide Electrolysis Cells (SOEC). In Proceedings of the 36th International Conference and Exposition on Advanced Ceramics and Composites, Daytona Beach, FL (2012).

[40] L. Bay, T. Jacobsen. Dynamics of the YSZ-Pt interface. Solid State Ionics 1997;93:201–6.

[41] K.V. Jensen, R. Wallenberg, I. Chorkendorff, M. Mogensen. Effect of impurities on structural and electrochemical properties of the Ni–YSZ interface. Solid State Ionics 2003;160:27–37.

[42] M.J. Jørgensen, M. Mogensen. Importance of Solid Oxide Fuel Cell LSM/YSZ Composite Cathodes. J Electrochem Soc 2001;148(5):A433–42.

[43] J.S. Cronin, K. Muangnapoh, Z. Patterson, K.J. Yakal-Kremski, V.P. Dravid, S.A. Barnett. Effect of Firing Temperature on LSM-YSZ Composite Cathodes: A Combined Three-Dimensional Microstructure and Impedance Spectroscopy Study. J Electrochem Soc 2012;159(4):B385–93.

[44] K. Chen, N. Ai, S.P. Jiang. Performance and stability of (La,Sr)MnO_3–Y_2O_3–ZrO_2 composite oxygen electrodes under solid oxide electrolysis cell operation conditions. Int J Hydrogen Energ 2012;37:10517–25.

[45] S.P. Jiang. Nanoscale and nano-structured electrodes of solid oxide fuel cells by infiltration: Advances and challenges. Int J Hydrogen Energ 2012;37:449–70.

[46] C. Yang, C. Jin, A. Coffin, F. Chen. Characterization of infiltrated $(La_{0.75}Sr_{0.25})_{0.95}MnO_3$ as oxygen electrode for solid oxide electrolysis cells. Int J Hydrogen Energ 2010;35:5187–93.

[47] K. Chen, N. Ai, S.P. Jiang. Reasons for the high stability of nano-structured (La,Sr)MnO_3 infiltrated Y_2O_3-ZrO_2 composite oxygen electrodes of solid oxide electrolysis cells. Electrochem Commun 2012;19:119–22.

[48] N. Li, M. Keane, M.K. Mahapatra, P. Singh. Mitigation of the delamination of LSM anode in solid oxide electrolysis cells using manganese-modified YSZ. Int J Hydrogen Energ 2013;38:6298–303.

[49] M. Yang, A. Yan, M. Zhang, Z. Hou, Y. Dong, M. Cheng. Effects of GDC interlayer on performance of low-temperature SOFCs. J Power Sources 2008;175:345–52.

[50] E.D. Wachsman, K.T. Lee. Lowering the Temperature of Solid Oxide Fuel Cells. Science 2011;334:935–9.

[51] H.J. Ko, J.-J. Lee, S.-H. Hyun. Structural Stability of the GDC Electrolyte for Low Temperature SOFCs Depending on Fuels. Electrochem Solid St 2010;13(10):B113–5.

[52] N.A. Baharuudin, H.A. Rahman, A. Muchtar, A.B. Sulong, H. Abdullah. Development of lanthanum strontium cobalt ferrite composite cathodes for intermediate- to low-temperature solid oxide fuel cells. J Zhejiang Univ-Sc A 2013;14(1):11–24.

[53] E. Magnone. A Systematic Literature Review on BSCF-Based Cathodes for Solid Oxide Fuel Cell Applications. J Fuel Cell Sci Tech 2010;7:064001-1–11.

[54] K. Sasaki, M. Muranaka, A. Suzuki, T. Terai. Determination of Oxygen Pathway in Silver Cathodes by Secondary-Ion Mass Spectroscopy Using Oxygen Isotope Exchange. J Electrochem Soc 2011;158(11):B1380–3.

[55] Z. Wu, M. Liu. Ag-$Bi_{1.5}Y_{0.5}O_3$ Composite Cathode Materials for $BaCe_{0.8}Gd_{0.2}O_3$-Based Solid Oxide Fuel Cells. J Am Ceram Soc 1998;81(5):1215–20.

[56] M. Camaratta, E. Wachsman. Silver-bismuth oxide cathodes for IT-SOFCs Part II – Improving stability through microstructural control. Solid State Ionics 2007;178: 1411–8.

[57] A. Jaiswal, E.D. Wachsman. Direct current bias studies on $(Bi_2O_3)_{0.8}(Er_2O_3)_{0.2}$ electrolyte and Ag–$(Bi_2O_3)_{0.8}(Er_2O_3)_{0.2}$ cermet electrode. Solid State Ionics 2006;177:677–85.

[58] W. Zhou, Z. Shao, F. Liang, Z.-G. Chen, Z. Zhu, W. Jin, N. Xu. A new cathode for solid oxide fuel cells capable of in situ electrochemical regeneration. J Mater Chem 2011;21:15343–51.

[59] Y. Lin, C. Su, C. Huang, J.S. Kim, C. Kwak, Z. Shao. A new symmetric solid oxide fuel cell with a samaria-doped ceria framework and a silver-infiltrated electrocatalyst. J Power Sources 2012;197:57–64.

[60] M. Liang, B. Yu, M. Wen, J. Chen, J. Xu, Y. Zhai. Preparation of LSM–YSZ composite powder for anode of solid oxide electrolysis cell and its activation mechanism. J Power Sources 2009;190:341–5.

[61] A.J. Bard. Electrochemical Methods: Fundamentals and Applications. Hoboken, NJ: Wiley, 2000.

[62] T.P. Holme, R. Pornprasertsuk, F.B. Prinz. Interpretation of Low Temperature Solid Oxide Fuel Cell Electrochemical Impedance Spectra. J Electrochem Soc 2010;157(1):B64–70.

[63] A. Leonide. SOFC Modelling and Parameter Identification by means of Impedance Spectroscopy. Dissertation, Karlsruhe Institute of Technology. Karlsruhe: KIT Scientific Publishing, 2010.

[64] S.P. Jiang, J.G. Love, J.P. Zhang, M. Huong, Y. Ramprakash, A.E. Hughes, S.P.S. Badwal. The electrochemical performance of LSM/zirconia–yttria interface as a function of a-site non-stoichiometry and cathodic current treatment. Solid State Ionics 1999;121:1–10.

[65] M. Backhaus-Ricoult, K. Adib, T. St.Clair, B. Luerssen, L. Gregoratti, A. Barinov. In-situ study of operating SOFC LSM/YSZ cathodes under polarization by photoelectron microscopy. Solid State Ionics 2008;179:891–5.

[66] J.I. Gazzarri, O. Kesler. Non-destructive delamination detection in solid oxide fuel cells. J Power Sources 2007;167:430–41.

[67] M. Chen. Understanding the Thermodynamics at the $LaMnO_3$-YSZ Interface in SOFC. Ph.D. Dissertation. ETH Zurich, 2005.

[68] J.A. Labrincha, J.R. Frade, F.M.B. Marques. $La_2Zr_2O_7$ formed at ceramic electrode/YSZ contacts. J Mater Sci 1993;28:3809–15.

[69] N.Q. Minh, T. Takahashi. Science and Technology of Ceramic Fuel Cells. Amsterdam: Elsevier Ltd, 1995.

[70] C.M. D'Souza, N.M. Sammes. Mechanical Properties of Strontium-Doped Lanthanum Manganite. J Am Ceram Soc 2000;83(1):47–52.

[71] A.V. Virkar. Mechanism of oxygen electrode delamination in solid oxide electrolyzer cells. Int J Hydrogen Energ 2010;35:9527–43.

[72] M. De Ridder, R.G. van Welzenis, A.W. Denier van der Gon, H.H. Brongersma, S. Wulff, W.-F. Chu, W. Weppner. Subsurface segregation of yttria in yttria-stabilized zirconia. J Appl Phys 2002;92(6):3056–64.

[73] C. Clausen, C. Bagger, J.B. Bilde-Sørensen, A. Horsewell. Microstructural and microchemical characterization of the interface between $La_{0.85}Sr_{0.15}MnO_3$ and Y_2O_3-stabilized ZrO_2. Solid State Ionics 1994;70/71:59–64.

[74] W.W. Mullins. Theory of Thermal Grooving. J Appl Phys 1957;28(3):333–9.

[75] M. Juhl, S. Primdahl, C. Manon, M. Mogensen. Performance/structure correlation for composite SOFC cathodes. J Power Sources 1996;61:173–81.

[76] J.C. Lin, J.Y. Chan. On the resistance of silver migration in Ag-Pd conductive thin films under humid environment and applied d.c. field. Mater Chem Phys 1996;43:256–65.

[77] R.P. Carreker, Jr, W.R. Hibbard, Jr. Tensile Deformation of Aluminum as a Function of Temperature, Strain Rate and Grain Size. General Electric Research Laboratory. WADC Technical Report 55-113 (1955).

[78] S.B. Rane, T. Seth, G.J. Phatak, D.P. Amalnerkar, M. Ghatpande. Effect of inorganic binders on the properties of silver thick films. J Mater Sci-Mater El 2004;15:103–6.

[79] A.M. Szaplonczay. Effect of Copper on the Solubility of Palladium in Nitric Acid Solutions in Analysis of Electroplated Palladium Layers. Anal Chem 1983;55:2202–4.

[80] H.J. Fraser. Microchemistry of the precious metal elements. Am Mineral 1937;22(10):1016–34.

[81] A. Lodder, J.P. Dekker. The Electromigration Force in Metallic Bulk. AIP Conf Proc 1998:418:315–28.

[82] L. Gremillard, T. Epicier, J. Chevalier, G. Fantozzi. Microstructural Study of Silica-Doped Zirconia Ceramics. Acta Mater 2000;48:4647–52.

[83] F. Gonella, G. Mattei, P. Mazzoldi. Structural and Optical Properties of Silver-Doped Zirconia and Mixed Zirconia-Silica Matrices Obtained by Sol-Gel Processing. Chem Mater 1999;11:814–21.

[84] Calculated using HSC Chemistry software (Outotec).

[85] N. Vivet, S. Chupin, E. Estrade, A. Richard, S. Bonnamy, D. Rochais, E. Bruneton. Effect of Ni content in SOFC Ni-YSZ cermets: A three-dimensional study by FIB-SEM tomography. J Power Sources 2011;196:9989–97.

[86] T. Klemensø, C. Chung, P.H. Larsen, M. Mogensen. The Mechanism Behind Redox Instability of Anodes in High-Temperature SOFCs. J Electrochem Soc 2005;152(11):A2186–92.

[87] M. Liang, B. Yu, M. Wen, J. Chen, J., Y. Zhai. Preparation of LSM–YSZ composite powder for anode of solid oxide electrolysis cell and its activation mechanism. J Power Sources 2009;190:341–5.

[88] V.K. Nagesh, J.A. Pask. Wetting of nickel by silver. J Mater Sci 1983;18(9):2665–70.

[89] R. Arróyave. Thermodynamics and Kinetics of Ceramic/Metal Interfacial Interactions. Dissertation, Massachusetts Institute of Technology. Cambridge: Massachusetts Institute of Technology, 2004.

[90] D. Simwonis, F. Tietz, D. Stöver. Nickel coarsening in annealed Ni/8YSZ anode substrates for solid oxide fuel cells. Solid State Ionics 2000;132:241–51.

[91] H.J. Grabke, R. Krajak, E.M. Müller-Lorenz, S. Strauß. Metal dusting of nickel-base alloys. Mater Corros 1996;47:495–504.

[92] Y. Matsuzaki, I. Yasuda. The poisoning effect of sulfur-containing impurity gas on a SOFC anode: Part I. Dependence on temperature, time, and impurity concentration. Solid State Ionics 2000;132:261–9.

[93] W.A. Meulenberg, O. Teller, U. Flesch, H.P. Buchkremer, D. Stöver. Improved contacting by the use of silver in solid oxide fuel cells up to an operating temperature of 800 °C. J Mater Sci 2001;36:3189–95.